A study of J/ψ production in Pb-Pb collisions at $\sqrt{s_{NN}}$ = 5.02 TeV

A thesis
submitted in partial fulfillment of requirements for the award of the degree of

Doctor of Philosophy
in
Applied Physics

by

Tahir Hussain

Under the supervision of
Dr. Mohammad Mohisin Khan

Department of Applied Physics
Zakir Hussain College of Engineering & Technology
Aligarh Muslim University, Aligarh
INDIA

2018

Declaration

I, ***Tahir Hussain***, Department of Applied Physics, Aligarh Muslim University (AMU), Aligarh certify that the work embodied in this Ph.D. thesis is my own bonafide work carried out by me under the supervision of ***Dr. Mohammad Mohisin Khan***, Assistant Professor, Department of Applied Physics at the AMU, Aligarh. The matter embodied in this Ph.D. thesis has not been submitted for the award of any other degree.

I declare that I have faithfully acknowledged, given credit to and referred to the research workers wherever their works have been cited in the text and the body of the thesis. I further certify that I have not wilfully lifted up some other's work, paragraph, text, data, result, etc. reported in the journals, books, magazines, reports, dissertations, theses, etc. or available at websites and included them in this Ph.D. thesis and cited as my own work.

Date: September 04, 2018 **(Tahir Hussain)**

Certificate from the Supervisor

This is to certify that the above statement made by the candidate is correct to the best of my knowledge.

Signature of the Supervisor:

Name & Designation: Dr. M. Mohisin Khan (Assistant Professor)

Department: Applied Physics, AMU, Aligarh

(Signature of the Chairman of the Department with seal)

Course/Comprehensive Examination/ Pre-submission Seminar Completion Certificate

This is to certify that ***Mr. Tahir Hussain***, Department of Applied Physics, Aligarh Muslim University, Aligarh has satisfactorily completed the course work/comprehensive examination and pre-submission seminar requirement, which was part of his Ph.D. programme.

Date:..... **(Signature of the Chairman of the Department)**

Acknowledgements

First of all, I am highly thankful to Almighty "Allah" without whose grace and mercy I could not have accomplished my research work.

At the outset, I sincerely wish to acknowledge and express my deep sense of gratitude to my research supervisor Dr. Mohammad Mohisin Khan, Assistant Professor, Department of Applied Physics, Aligarh Muslim University (AMU) for his extraordinary cooperation and supervision. He gave me full freedom to explore this beautiful branch of physics and gave room to select the topic of my choice for my Ph.D. thesis. This thesis is the result of his painstaking and generous attitude.

I am highly indebted to Professor Shakeel Khan, Chairman, Department of Applied Physics, AMU, Aligarh, for his support and encouragement. I am equally thankful to all the faculty members, Prof. Ameer Azam in particular, of the Department for their moral support, intellectual inputs and encouragement. I also take this opportunity to thank Professor Tauheed Ahmad, Chairman, Department of Physics, AMU, Aligarh for his support and cooperation, particularly during last academic session when I was teaching in the Department.

I feel blessed to have some great mentors throughout my career. I am extremely grateful to Prof. M. Irfan for his invaluable suggestions and guidance. I attribute my Ph.D. in experimental high-energy physics to him. I owe my low-p_T analysis to Prof. Sukalyan Chattopadhyay and Dr. Indranil Das, Saha Institute of Nuclear Physics (SINP), Kolkata.

My special thanks go to my seniors for their readiness to help and providing useful tips and tricks on everything. I wish to thank Dr. Kushal for providing help in the data analysis during the initial years of my Ph.D. and innumerable tea breaks. I also thank Dr. Nazeer Ahmad, Dr. Danish Azmi, Dr. Shafiqullah, Dr. Suhail Ahmad Siddiqui.

During my Ph.D. I was privileged to be part of the ALICE collaboration. I am grateful to Philippe Pillot for supervising my service work. I also wish to thank Laure

Massacrier for explanations regarding the analysis. I would also like to thank Boris Teyssier for sharing my burden by doing simulations.

I also express my gratitude to my friends Dr Amirullah, Dr Ashiq, Dr Aziz, Dr Hushnud, Wadut, Jhuma, Nayab for the support they always provided to me. Their help at many junctures made things much easier for me. I am also thankful to the staff members of the Department of Applied Physics for their help and cooperation during the study. I am also thankful to the staff of Maulana Azad Library, AMU, Seminar Library of Department of Applied Physics, AMU, for their help in locating and providing necessary research material required for this study.

In the end, I express my gratitude to my beloved parents, parents-in-law and sister for their inspiration, affection and constant encouragement, which sustained me throughout this venture. I would be failing in my duty if I do not put on record the help and the pains that my better half took in the course of the study. I am indebted to my son "Zayn" whom I could not give time and now he is just ten days away from his first birthday. I shall always remain indebted to all the above mentioned people and those whom I might have missed out. In the end I would like to say that all the positive points and features of this thesis are the results of the contributions from a host of people but, follies, if any, are entirely mine.

Finally, I gratefully acknowledge the financial support from University Grants Commission (UGC) through the Maulana Azad National Fellowship and Department of Science & Technology (DST), Government of India to pursue my Ph.D. degree.

Tahir Hussain

September 04, 2018

List of Figures

List of Tables

Contents

2

Charmonia and the Quark-Gluon Plasma

The production of heavy quarkonia is an important observable to study the properties of the nuclear matter created in high-energy heavy-ion collisions. Lattice QCD calculations predict a phase transition of the hadronic matter to a deconfined medium of quarks and gluons, popularly known as Quark-Gluon Plasma (QGP), at extreme energy densities. While passing through the deconfined medium the charmonium bound states are dissociated into quark-antiquark pair due to color screening. This is visible in data as a suppression of J/ψ resonances with respect to the proton-proton results scaled by the number of binary collisions. However, the cold nuclear matter effects can also lead to the suppression of J/ψ resonances in heavy-ion collisions. Cold nuclear effects are studied in p-Pb collisions since the QGP is not expected to be produced. ALICE measures the charmonium down to zero transverse momentum via the dimuon decay channel at forward rapidity ($2.5 < y < 4$). Hard probes are important tools for a detailed characterization of the deconfined medium. When the heavy-quark pair forms a quarkonium bound state, this process is non-perturbative as it involves long distances and soft momentum scales. Therefore, a detailed study of heavy-flavour production and the comparison to experimental data provides an important testing ground for both perturbative and non-perturbative aspects of QCD calculations.

In nucleus–nucleus collisions, quarkonium production is expected to be significantly suppressed as a consequence of the colour screening of the force that binds the $c\bar{c}$ ($b\bar{b}$) state. In this scenario, quarkonium suppression should occur sequentially, according

to the binding energy of each state. As a consequence, the in-medium dissociation probability of these states are expected to provide an estimate of the initial temperature reached in the collisions. At high centre-of-mass energy, a new production mechanism could be at work in the case of charmonium: the abundance of c and $\bar{c}$ quarks might lead to charmonium production by (re)combination of these quarks. An observation of the recombination of heavy quarks would therefore directly point to the existence of a deconfined QGP. Charm and beauty quarks provide important tools to investigate the energy-loss mechanisms, in addition to the QGP properties.

2.1 Charmonium in nucleus-nucleus collisions

Quarkonia are considered important probes of the QGP formed in heavy-ion collisions. In a hot and deconfined medium quarkonium production is expected to be significantly suppressed with respect to the proton–proton yield, scaled by the number of binary nucleon–nucleon collisions, as long as the total charm cross section remains unmodified[1]. The origin of such a suppression, taking place in the QGP, is thought to be the colour screening of the force that binds the $c\bar{c}$ ($b\bar{b}$) state [210]. In this scenario, quarkonium suppression should occur sequentially, according to the binding energy of each meson: strongly bound states, such as the Υ(1S) or the J/ψ, should melt at higher temperatures with respect to the more loosely bound ones, such as the χ_b , Υ(2S), or Υ(3S) for the bottomonium family or the ψ(2S) and the χ_c for the charmonium one. As a consequence, the in-medium dissociation probability of these states should provide an estimate of the initial temperature reached in the collisions [198]. However, the prediction of a sequential suppression pattern is complicated by several factors. Feed-down decays of higher-mass resonances, and of b-hadrons in the case of charmonium, contribute to the observed yield of quarkonium states. Furthermore, other hot and cold matter effects can play a role, competing with the suppression mechanism.

On the one hand, the production of c and $\bar{c}$ quarks increases with increasing centre-of-mass energy. Therefore, at high energies, as at the LHC, the abundance of c and $\bar{c}$ quarks might lead to a new charmonium production source: the (re)combination of these quarks throughout the collision evolution [196] or at the hadronisation stage [161, 180]. This

[1]As open heavy flavour and quarkonia are produced via the same processes, any modifications of the initial state will not modify the yield ratio of quarkonia to open heavy flavour states.

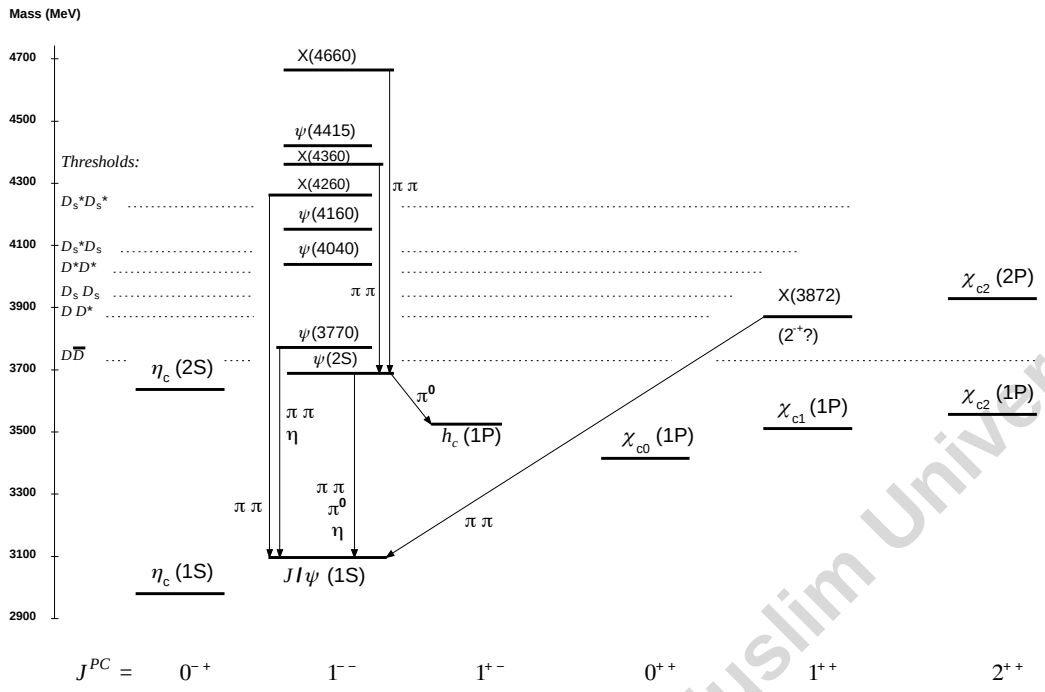

Figure 2.1: *Charmonium family with spectroscopic notations. Figure taken from [151].*

additional charmonium production mechanism, taking place in a deconfined medium, enhances the J/ψ yield and might counterbalance the expected J/ψ suppression.

The in-medium modification of quarkonium production, induced by either hot or cold matter mechanisms, is usually quantified through the nuclear modification factor R_{AA}, defined as the ratio of the quarkonium yield in A-A collisions ($N_{AA}^{q\bar{q}}$) and the expected value obtained by scaling the production cross section in pp collisions ($\sigma_{pp}^{q\bar{q}}$) by the average nuclear overlap function ($\langle T_{AA} \rangle$), evaluated through a Glauber model calculation [101]:

$$R_{AA} = \frac{N_{AA}^{q\bar{q}}}{\langle T_{AA} \rangle \times \sigma_{pp}^{q\bar{q}}} \tag{2.1}$$

R_{AA} is expected to equal unity if nucleus–nucleus collisions behave as a superposition of nucleon–nucleon interactions. This is, e.g., the case for electroweak probes (direct γ, W, and Z) that do not interact strongly [88, 120, 122, 126, 127]. A value of R_{AA} different from unity implies that the quarkonium production in AA is modified with respect to a binary nucleon–nucleon scaling. Further insight on the in-medium modification of quarkonium production can be obtained by investigating the rapidity and transverse momentum dependence of the nuclear modification factor.

Studies performed for thirty years, first at the SPS ($\sqrt{s_{NN}}$ = 17 GeV) and then at RHIC ($\sqrt{s_{NN}}$ = 39-200 GeV), have indeed shown a reduction of the J/ψ yield beyond the expectations from cold nuclear matter effects (such as nuclear shadowing and $c\bar{c}$ break-up). Even if the centre-of-mass energies differ by a factor of ten, the amount of suppression, with respect to pp collisions, observed by SPS and RHIC experiments at mid-rapidity is rather similar. This observation suggests the existence of an additional contribution to J/ψ production, the previously mentioned (re)combination process, which sets in already at RHIC energies and can compensate for some of the quarkonium suppression due to screening in the QGP. Furthermore, J/ψ suppression at RHIC is, unexpectedly, smaller at mid-rapidity than at forward rapidity, in spite of the higher energy density. The stronger J/ψ suppression at forward-y might be considered a further indication of the role played by (re)combination processes. Note, however, that the rapidity dependence of the (re)combination contribution is expected to be rather small [226, 227].

The measurement of charmonium production is especially promising at the LHC, where the higher energy density reached in the medium and the larger number of $c\bar{c}$ pairs produced in central Pb–Pb collisions (increased by a factor ten with respect to RHIC energies) should help to disentangle suppression and (re)combination scenarios.

2.2 Charmonium production: Theoretical overview

2.2.1 Sequential suppression and lQCD

Historically, the large masses of charm and beauty quarks provide the basis for a quarkonium spectroscopy through non-relativistic potential theory, introducing a confining potential in terms of a string tension [155].

State	J/ψ	χ_c(1P)	ψ(2S)	Υ(1S)	χ_b(1P)	Υ(2S)	χ_b(1P)	Υ(3S)
Mass (GeV/c^2)	3.07	3.53	3.68	9.46	9.99	10.02	10.26	10.36
Binding energy (GeV)	0.64	0.20	0.05	1.10	0.67	0.54	0.31	0.20
Radius (fm)	0.25	0.36	0.45	0.14	0.22	0.28	0.34	0.39

Table 2.1: *Mass, binding energy and radius for charmonia and bottomonia [155].*

The QGP consists of deconfined colour charges, so that the binding of a $q\bar{q}$ pair is subject to the effect of colour screening which limits the range of strong interactions. Intuitively, the fate of heavy quark bound states in a QGP depends on the size of the colour screening radius r_D (which is inversely proportional to the temperature, so that it decreases with increasing temperature) in comparison to the quarkonium binding radius r_q: if $r_D \gg r_q$, the medium does not really affect the heavy quark binding. Once $r_D \ll r_q$, however, the two heavy quarks cannot "see" each other any more and hence the bound state will melt. It is therefore expected that quarkonia will survive in a QGP through some range of temperatures above T_c, and then dissociate once T becomes large enough. Recent studies have shown that the Debye-screened potential develops an imaginary part, implying a class of thermal effects that generate a finite width for the quarkonium peak in the spectral function. These results can be used to study quarkonium in a weakly coupled Quark Gluon Plasma within an Effective Field Theories (EFT) framework [176]. On the other hand lattice-QCD enables ab initio study of quarkonium correlation functions in the strongly coupled regime. The sequential dissociation scenario is confirmed by all these approaches [177].

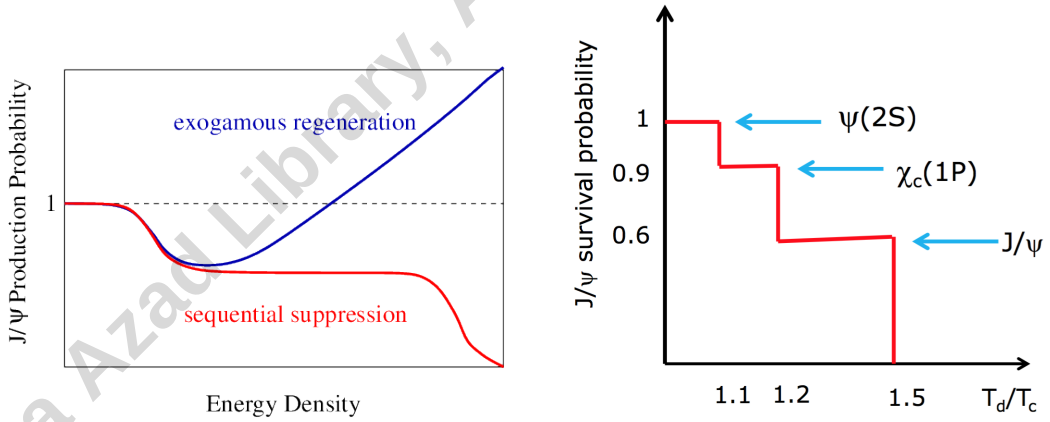

Figure 2.2: *A sketch of J/ψ showing regeneration and suppression (left). Sequential suppression of different charmonium states. T_d & T_s represents dissociation and critical temperature respectively (right).*

The survival probability for a given quarkonium state depends on its size and binding energy (see Table 2.1 for details[2]). Hence the excited states will be dissolved at a lower

[2]Note that in this Table the calculation of the binding energies and radii of the quarkonium states is made with an arbitrary potential model with arbitrary parameters, so they do not correspond to the experimental masses of quarkonia but are model dependent. These values are to be taken as an illustration of the expected Debye screening ordering.

initial temperature than the more tightly bound ground states. However, only a fraction (about 60%) of the observed J/ψ is a directly produced (1S) state, the remainder is due to the feed-down of excited states, with about 30% from χ_c(1P) and 10% from ψ(2S) decays [103, 104]. The decay processes occur far outside the produced medium, so that the medium affects only the excited states. As a result, the formation of a hot deconfined medium in nuclear collisions will produce a sequential quarkonium suppression pattern [146], as illustrated in Figure 2.2b. Increasing the energy density of the QGP above deconfinement first leads to ψ(2S) dissociation, removing those J/ψs which otherwise would have come from ψ(2S) decays. Next the χ_c melts, and only for a sufficiently hot medium also the direct J/ψ disintegrate.

2.2.2 Summary of theoretical models

Different theoretical models are available for comparison. Among them, the statistical hadronisation model, the transport model, the collisional dissociation model, and the comover model will be compared to charmonium experimental results in the next section. Their principal characteristics can be summarised as follows.

In the statistical hadronisation model, the charm (beauty) quarks and antiquarks, produced in initial hard collisions, thermalise in a QGP and form hadrons at chemical freeze-out. It is assumed that no quarkonium state survives in the deconfined state (full suppression) and, as a consequence, also CNM effects are not included in this model. An important aspect in this scenario is the canonical suppression of open charm or beauty hadrons, which determines the centrality dependence of production yields in this model. The overall magnitude is determined by the input charm (beauty) production cross section. Kinetic (re)combination of heavy quarks and antiquarks in a QGP provides an alternative quarkonium production mechanism. In transport models, there is continuous dissociation and (re)generation of quarkonia over the entire lifetime of the deconfined state. A hydrodynamical-like expansion of the fireball of deconfined matter, constrained by data, is part of such models, alongside an implementation of the screening mechanism with inputs from lattice QCD. Other important ingredients are parton-level cross sections. Cold nuclear matter effects are incorporated by means of an overall effective absorption cross section that accounts for (anti-)shadowing, nuclear absorption, and Cronin effects.

The collisional dissociation model considers, in addition to modifications of the

binding potential by the QGP and cold nuclear matter effects, radiative energy loss of the colour octet quarkonium precursor and collisional dissociation processes inside the QGP. Similarly, the comover interaction model includes dissociation of quarkonia by interactions with the comoving medium of hadronic and partonic origin. Regeneration reactions are also included. Their magnitude is determined by the production cross section of $c\bar{c}$ pairs and quarkonium states. Cold nuclear matter effects are taken into account by means of (anti-)shadowing models.

In transport and comover models, at LHC energies, a large fraction of J/ψ (> 50% in most central collisions) is produced by charm quark recombination. In the statistical hadronization model, all J/ψ are generated at the hadronization stage by purely statistical mechanisms.

2.3 Charmonium production in A-A collisions: Experimental results

2.3.1 Nuclear modification factor (R_{AA})

The nuclear matter at extreme temperature and density is investigated through the measurements of nuclear modification factor (R_{AA}). The study of R_{AA} gives information about the medium created in the heavy-ion collisions. Charmonium suppression and its regeneration is examined by the measurement of R_{AA}. It is one of the most important observable of QGP formation. The Figure 2.3 compares the centrality dependence of R_{AA} for Pb-Pb collisions at $\sqrt{s_{NN}}$ = 5.02 TeV [96] and $\sqrt{s_{NN}}$ = 2.76 TeV [77]. For both the energies the centrality dependence shows the same trend, increasing suppression up to N_{part} ~ 100 followed by approximately static value of R_{AA}.

The increase in the value of R_{AA} in peripheral collisions is due to the photo-production of J/ψ [95]. In order to minimize the contribution of the photo-produced J/ψ to the hadronic R_{AA} and better comparison with the models, the Figure 2.4 is plotted for 0.3 < p_T < 8 GeV/c. In the Figure 2.6 the region p_T > 0.3 GeV/c is not excluded as the contribution of photo-produced J/ψ is negligible in central collisions. The transport model of Ref. [225, 228] (TM1) describes well the p_T dependence of R_{AA}. The study of p_T dependence of R_{AA} shows that at the LHC energies J/ψ production can be understood as combination

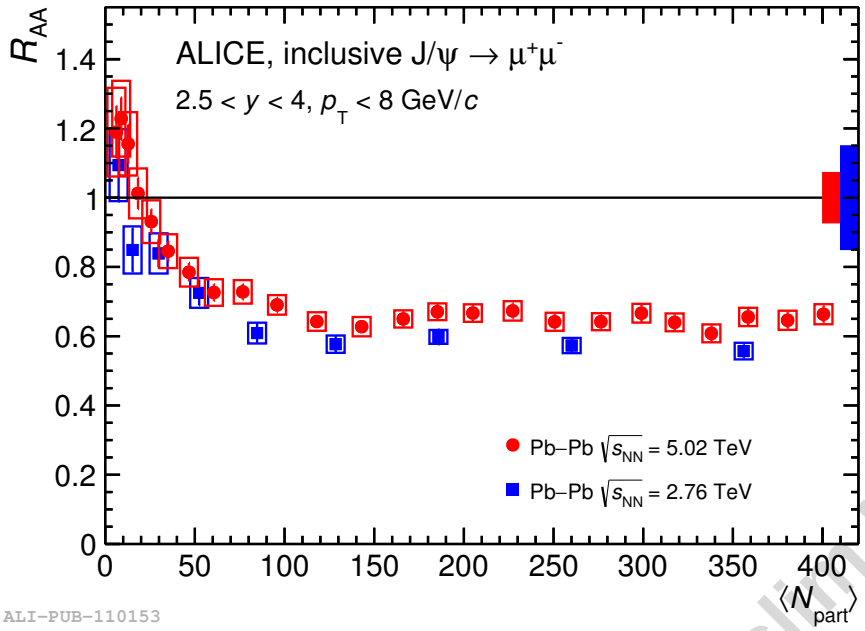

Figure 2.3: *Comparison of the nuclear modification factor for inclusive J/ψ production as a function of centrality for Pb-Pb collisions at $\sqrt{s_{NN}}$ = 5.02 TeV [96] and $\sqrt{s_{NN}}$ = 2.76 TeV [77]. The error bars represents statistical uncertainties, boxes around the points uncorrelated systematic uncertainties. The centrality correlated global uncertainties are shown as a filled box around $R_{AA} = 1$.*

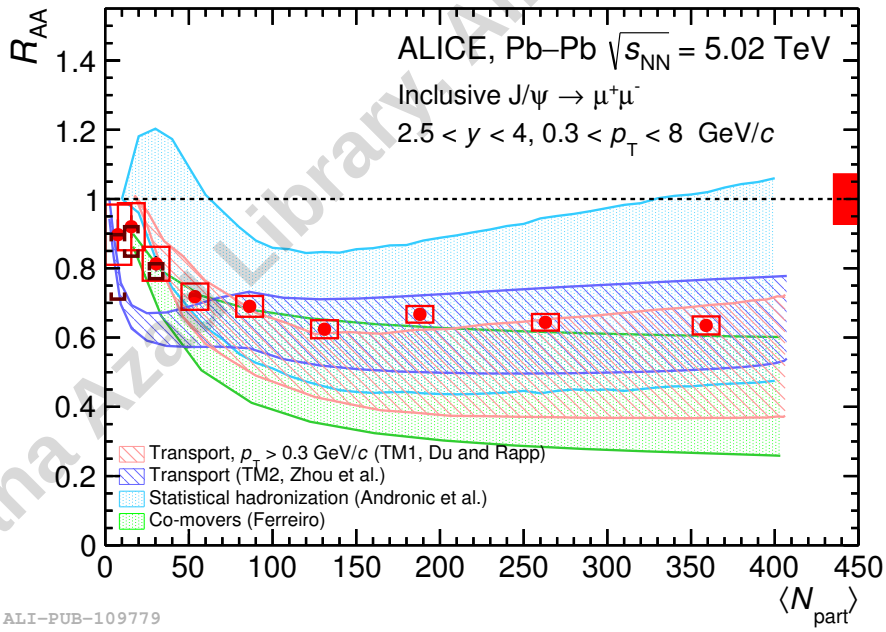

Figure 2.4: *Centrality dependence of the inclusive J/ψ R_{AA} for 0.3 < p_T < 8 GeV/c in Pb-Pb collisions at $\sqrt{s_{NN}}$ = 5.02 TeV compared with different theoretical models [5, 139, 140, 163, 225, 228]. The error bars represents statistical uncertainties, boxes around the points uncorrelated systematic uncertainties. The centrality correlated global uncertainties are shown as a filled box around $R_{AA} = 1$ [96].*

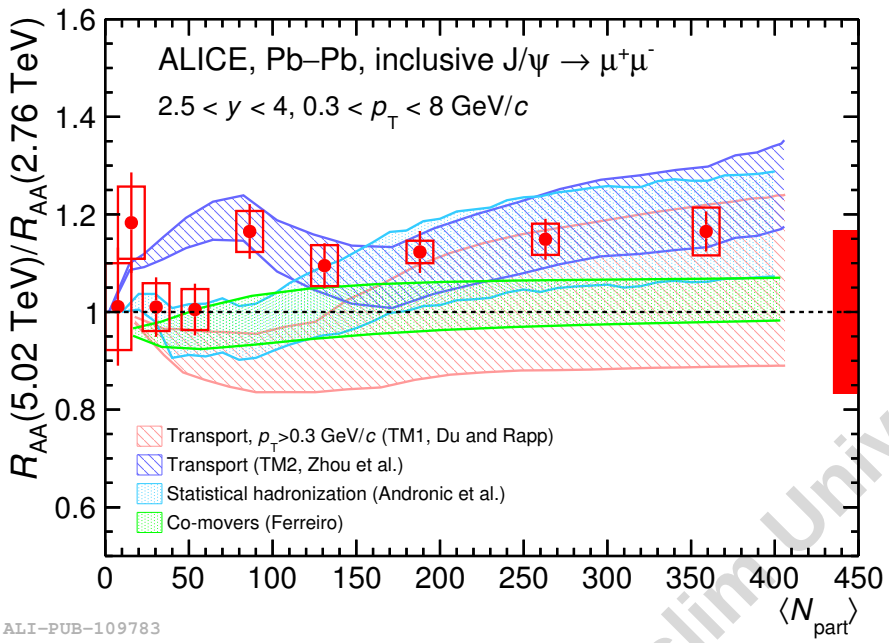

Figure 2.5: *The ratio of the inclusive J/ψ R_{AA} between $\sqrt{s_{NN}}$ = 5.02 TeV and $\sqrt{s_{NN}}$ = 2.76 TeV for 0.3 < p_T < 8 GeV/c as a function of centrality compared with different theoretical models [5, 139, 140, 163, 225, 228]. The collision system is Pb-Pb. [96].*

of suppression and regeneration that takes place in QGP, the aforesaid mechanisms are prominent at high and low-p$_T$ respectively. It can be seen from the Figure 2.6 that there is a hint for an increase in R_{AA} from $\sqrt{s_{NN}}$ = 2.76 TeV to $\sqrt{s_{NN}}$ = 5.02 TeV is visible in the region 2 < p_T < 6 GeV/c, whereas the results are consistent elsewhere. Models that include a p$_T$ dependent contribution from (re)combination, amounting ≈ 50% at low-p$_T$ and vanishing at high-p$_T$ provide a reasonably good description of the data.

2.3.2 J/ψ elliptic flow

The J/ψ elliptic flow measurement was performed by the ALICE at forward as well as mid-rapidity in Pb-Pb collisions at $\sqrt{s_{NN}}$ = 5.02 TeV. It is an important observable to characterize the medium created under extreme conditions. At forward rapidity, the p_T dependence of the J/ψ v_2 was investigated in three centrality classes shown in Figure 2.8. The J/ψ v_2 signal can be clearly seen from the Figure 2.8 in the region 2 < p_T < 8 GeV/c for all the centrality classes. This provides conclusive evidence of the collective flow of the J/ψ mesons. The p_T dependence of the J/ψ v_2 was measured only in a single centrality class (20%-40%) at mid-rapidity which exhibits the similar trend but with larger uncertainties. The transport models [117, 163, 225] could not explain the large value

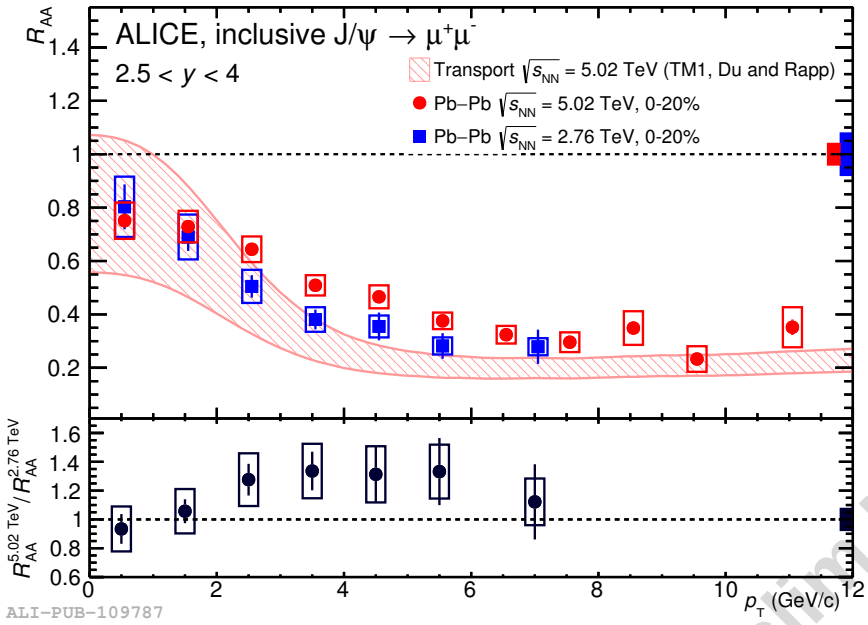

Figure 2.6: *The p_T dependence of the inclusive J/ψ R_{AA} in Pb-Pb collisions at $\sqrt{s_{NN}} = 5.02$ TeV compared to the corresponding result at $\sqrt{s_{NN}} = 2.76$ TeV and to the transport model [77, 225, 228].*

of J/ψ v_2 in the high-p_T region. However, at low-p_T, the magnitude of the observed v_2 are reproduced by the aforementioned models by invoking concept of J/ψ (re)generation through the (re)combination of thermalized charm quarks in the QGP. Thus, J/ψ elliptic flow in conjunction with the R_{AA} provides considerable evidence for thermalized charm quarks and (re)generation of J/ψ.

2.3.3 Charmonium photoproduction in UPC collisions

The ALICE Collaboration studied the J/ψ and ψ' photoproduction at mid-rapidity in ultra-peripheral Pb-Pb collisions at $\sqrt{s_{NN}}$ = 2.76 TeV [84]. The cross section of coherent J/ψ photoproduction was compared with six different model calculations [8, 13, 202, 208, 221, 222], shown in Figure 2.9. The J/ψ photoproduction cross section measurement is a powerful tool to constrain the nuclear gluon shadowing in the region x≈10^{-3}. The coherent J/ψ cross section was consistent with the models which take into account the nuclear gluon shadowing according to the EPS09 parameterization (AB-EPS09). However, models which do not consider nuclear gluon shadowing are inconsistent with the observed results, like those which use the Glauber model to incorporate nuclear effects. The AB-HKN07 and AB-EPS08 models either underestimate

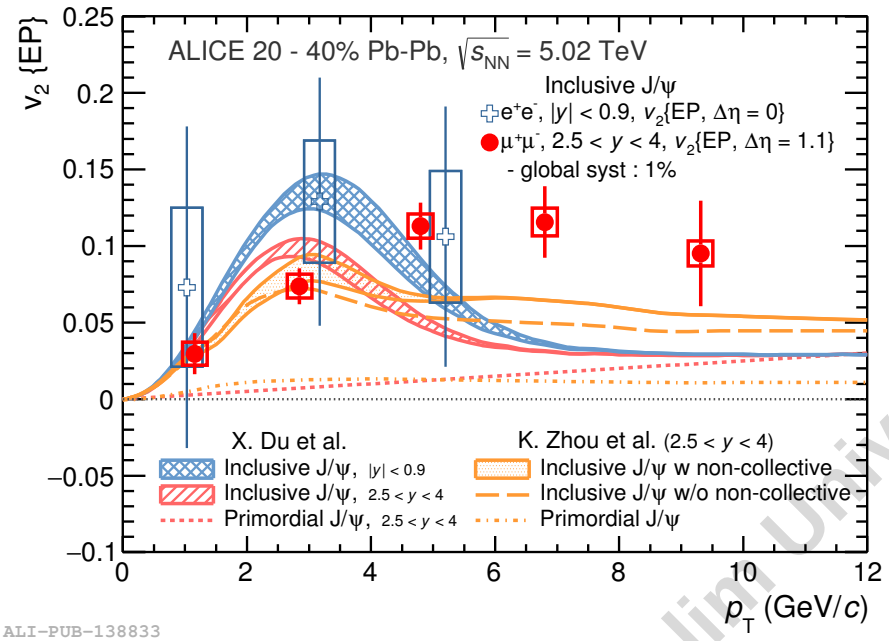

Figure 2.7: *The inclusive J/ψ $v_2(p_T)$ at forward and mid-rapidity for the centrality interval 20%-40% in Pb-Pb collisions at $\sqrt{s_{NN}}$ = 5.02 TeV. Transport models [117, 163] calculations are also plotted for comparison. The vertical bars represents the statistical uncertainties, whereas boxes indicate the uncorrelated systematic uncertainties. [118].*

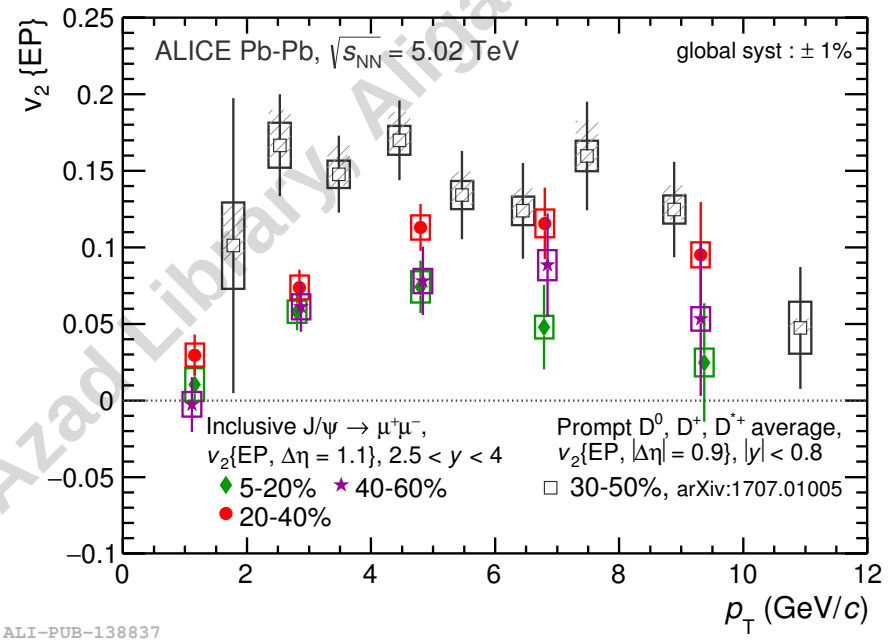

Figure 2.8: *Inclusive J/ψ $v_2(p_T)$ at forward rapidity in Pb-Pb collisions at $\sqrt{s_{NN}}$ = 5.02 TeV for three centrality classes 5%-20%, 20%-40% and 40%-60%. The average of D^0, D^+ and D^{*+} at mid-rapidity in the centrality class 30%-50% is also shown for comparison [119]. Figure and caption are taken from [118].*

or overestimate the effect of shadowing to match the data.

Furthermore, the incoherent J/ψ photoproduction cross section were compared with calculations from the three models [202, 208, 222], shown in Figure 2.10. None of the

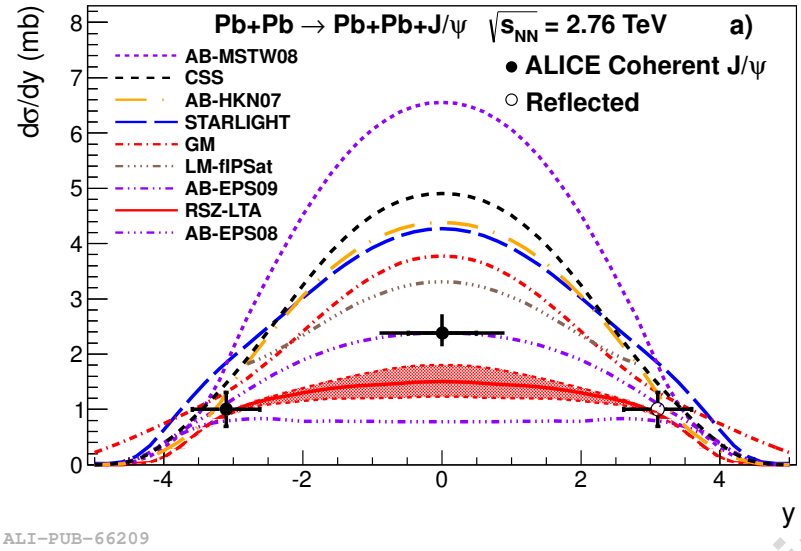

Figure 2.9: *Differential cross section of J/ψ photoproduction in ultra-peripheral Pb-Pb collisions at* $\sqrt{s_{NN}} = 2.76$ *TeV for coherent events.*

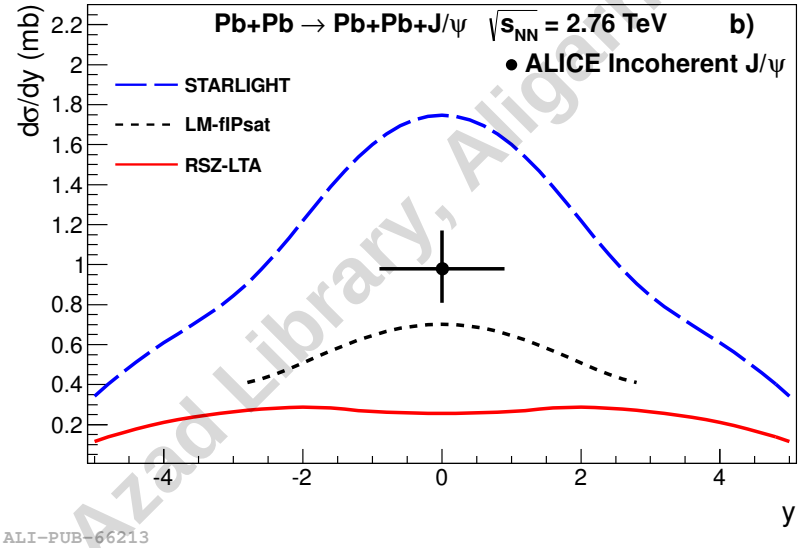

Figure 2.10: *Cross section for incoherent photonuclear production of J/ψ as measured by the ALICE.*

three existing models could match the observed incoherent photoproduction cross section correctly. Nevertheless, incoherent-to-coherent ratio was correctly predicted by the STARLIGHT. Finally, the observed two-photon cross section for di-electron production was in good agreement with the STARLIGHT model. This suggests that those models are not favored which predicts a strong contribution of higher-order terms (not included in the STARLIGHT) to the cross section.

2.3.4 Comparison of R_{AA}: LHC versus RHIC

It is interesting to compare results from the experiments of the world's top two most powerful colliders, i.e. LHC and RHIC[3]. The LHC operates at nearly 25 times more energy per nucleon pair. The statistical hadronisation or the recombination process is dominant in central collisions and, for kinematical reasons, they are expected to contribute mainly at low-p_T, and becomes negligible at high-p_T. This behavior is further examined by studying the p_T dependence of R_{AA}.

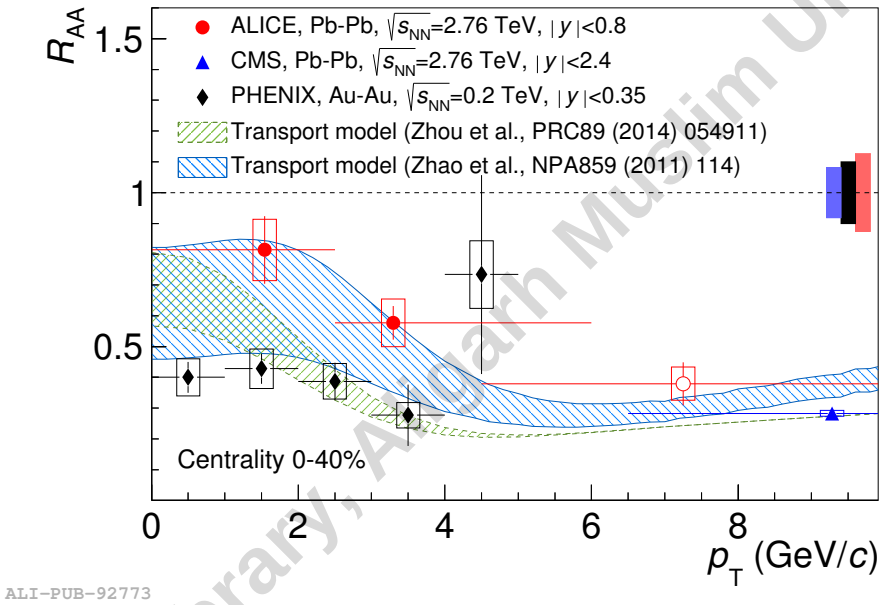

Figure 2.11: *Inclusive J/ψ R_{AA} versus p_T for the ALICE [77] and PHENIX result [52] in the similar forward rapidity region. Both results correspond to 0-40% centrality.*

In Figure 2.11 and Figure 2.12, the ALICE J/ψ R_{AA} dependence on p_T is compared with the corresponding PHENIX results in the similar rapidity intervals. In both rapidity regions, a striking difference in the pattern could be observed: while the ALICE J/ψ R_{AA} shows a continuous decrease from low to high p_T, the pattern observed at low energies, i.e. in the PHENIX data, is rather different. It is almost flat in the low-p_T region, with a suppression up to a factor four (two) stronger than at LHC at forward rapidity (mid-rapidity). The stronger suppression in PHENIX data is a clear manifestation that the role of recombination processes becoming important with increasing collision energy. Consequently, it can be seen from the Figure 2.12 that the J/ψ R_{AA} measured by the ALICE (LHC) is systematically larger, particularly in the low-p_T region. On the other

[3]Relativistic Heavy Ion Collier. It is located at Brookhaven National Laboratory (BNL) in Upton, USA.

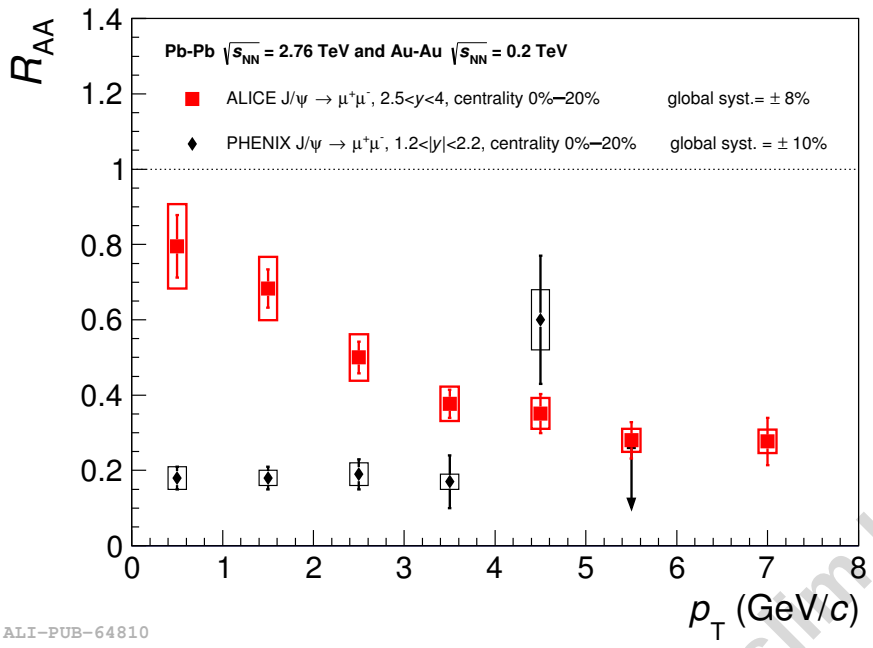

Figure 2.12: *The mid-rapidity result of ALICE [93] is compared to PHENIX result [52] within the same centrality class 0-20%.*

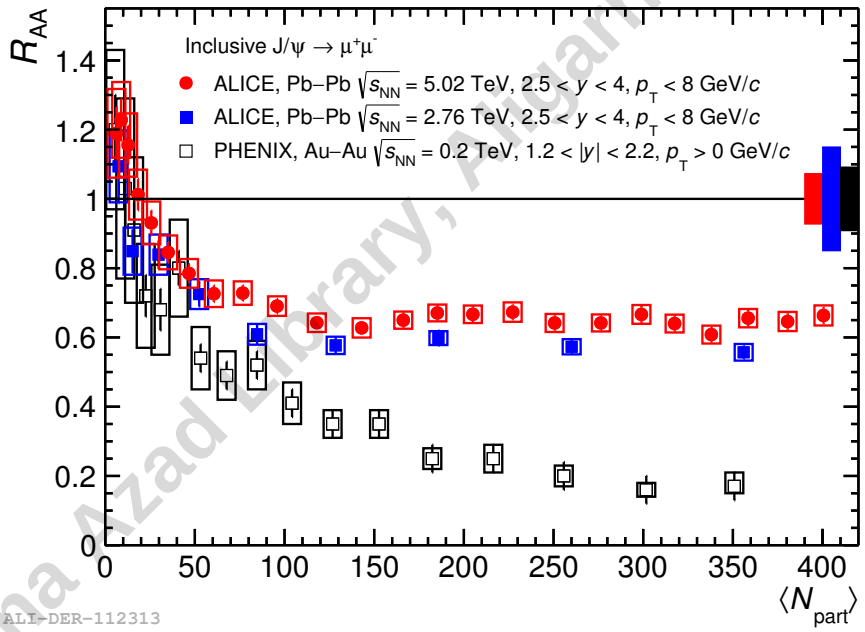

Figure 2.13

hand, there is no significant p_T dependence in the high-p_T region.

It is clearly evident from the Figure 2.13 that the regeneration of J/ψ, if any, is insignificant at RHIC energies and the suppression is the dominant mechanism. The R_{AA} measurement done by the ALICE at $\sqrt{s_{NN}}$ = 2.76 TeV and $\sqrt{s_{NN}}$ = 5.02 TeV shows similar centrality independent behavior for central events. There is a clear saturation of J/ψ suppression for N_{part} > 100 at $\sqrt{s_{NN}}$ = 5.02 TeV, thanks to fine centrality binning.

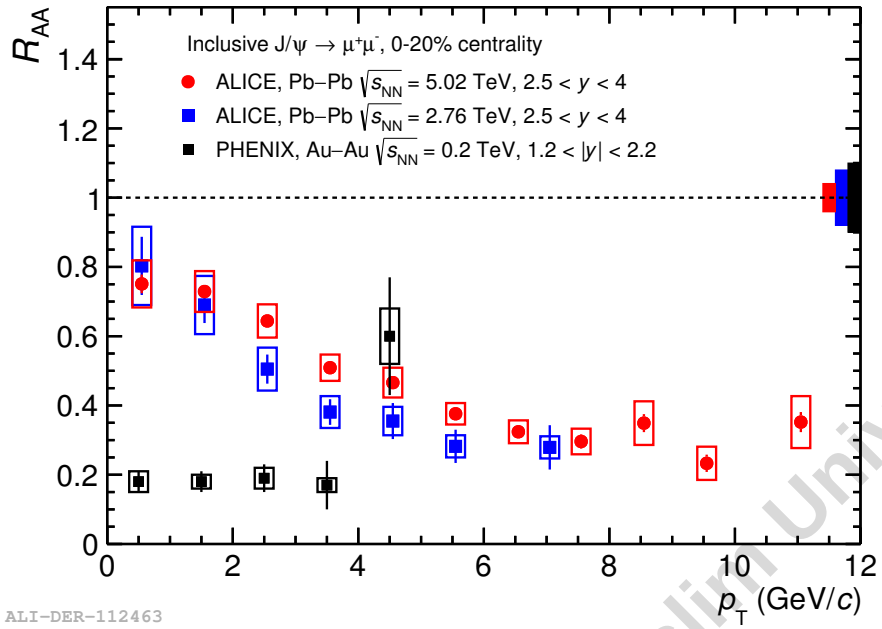

Figure 2.14

The J/ψ R_{AA} dependence on p_T shows similar trend, see Figure 2.14, and is almost independent of collision energy. At both the energies regeneration is the dominant mechanism at low-p_T, while suppression prevails at high-p_T.

Part II

Experimental setup

4

The Muon spectrometer

This chapter is dedicated to the ALICE forward Muon spectrometer [15, 19, 24]. The data recorded by this detector is used in the analysis presented in this thesis. The chapter describes various components of the Muon spectrometer.

4.1 Physics goals of the muon spectrometer

Hard probes, such as heavy-quarkonia states, are potent tools for probing the earliest and hottest stages of heavy-ion collisions [1, 2] as they are sensitive to the nature (i.e. confined versus deconfined) as well as collision dynamics of the medium created in these reactions. The aim of the ALICE forward muon spectrometer is to study the full spectrum of heavy-quark vector-meson resonances (i.e. $J/\psi, \psi', \Upsilon, \Upsilon', \Upsilon''$) as well as light vector mesons (ρ, ω, ϕ) via the $\mu^+\mu^-$ decay channel. The simultaneous measurement of all the quarkonia species with the same apparatus allows a direct comparison of their production rate as a function of different parameters such as collision centrality and transverse momentum. However, the production of open heavy-flavors (D and B mesons) and weak bosons ($W^{\pm}$, Z^0) are also measured through their semi-muonic decay channels with the muon spectrometer. The muon arm also enables to explore the low Bjorken-x at values never reached before. We may go down to $x = 2 \times 10^{-6}$ for the $c\bar{c}$ in pp collisions at 14 TeV/c [211]. It performs muon detection in the pseudorapidity interval $-4.0 \leq \eta \leq -2.5$ (corresponding to polar angle range $171^\circ \leq \theta \leq 178^\circ$) in

order to provide good acceptance down to zero transverse momentum and a manageable background from hadron decays.

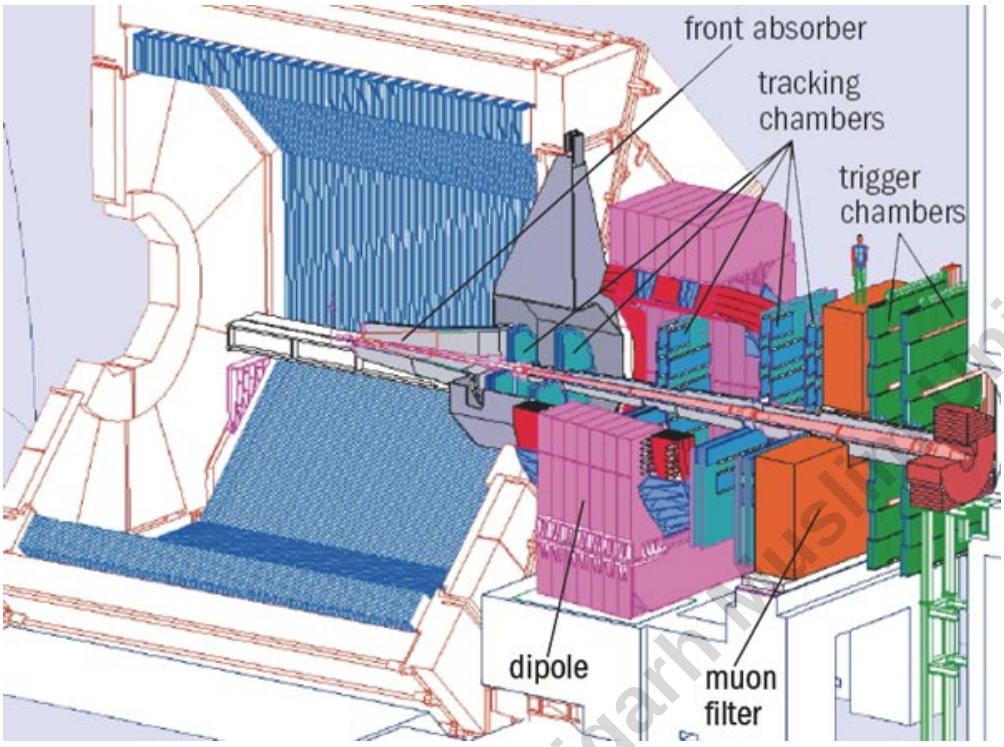

Figure 4.1: *Layout of the muon spectrometer. Figure taken from [148].*

The notable features, which also influenced its design, of the muon arm are as follows: Its acceptance was chosen as large as possible to address the statistics constraints (especially for the Υ family). Furthermore, a large acceptance down to zero p_T is required for the measurement of direct J/ψ's. At high p_T a considerable fraction of J/ψ's are produced through B-decay [59]. It has a mass resolution of 100 MeV/c^2 in the 10 GeV/c^2 dimuon invariant-mass region, sufficient to resolve the $\Upsilon(1S)$, $\Upsilon(2S)$ and $\Upsilon(3S)$ resonances. In addition, the tracking and trigger detectors of the muon arm has a very high granularity read-out to cope with the high particle multiplicity produced in the heavy-ion central collisions.

4.2 Components of the muon arm

The 3D view and the longitudinal cross-section of the muon spectrometer is shown in Figure 4.1 and Figure 4.2 respectively. It is mainly composed of a front absorber, an inner beam shield (small angle absorber), a dipole magnet, muon filter (iron wall), two

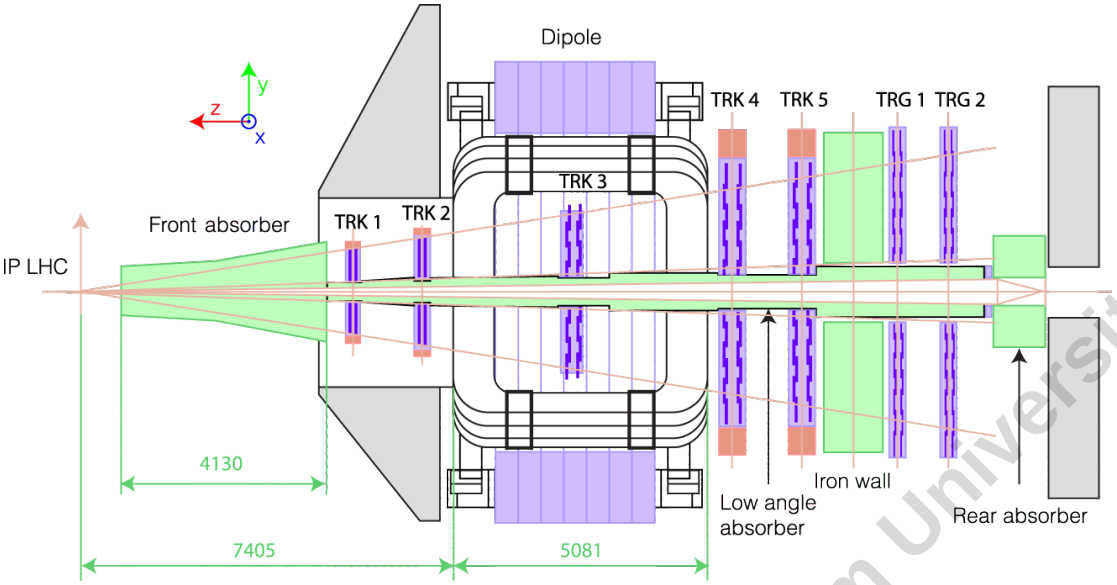

Figure 4.2: *Longitudinal cross section of the muon spectrometer. The Station 1 is closest to the interaction point. Note that the front absorber and the first two tracking stations are inside the L3 solenoid magnet. Figure taken from [64].*

trigger stations and five tracking stations. The different components, constituting the spectrometer, are now explained:

4.2.1 Absorbers

Front absorber

The purpose of the front absorber is to provide strong absorption of the charged hadrons and photons flux coming from the central nucleus-nucleus collisions. It also safeguards other ALICE detectors from particles produced in secondary interactions within the absorbing material itself [128]. The front absorber is designed to minimize the mass resolution deterioration and, hence, the most critical component of the forward muon arm [214]. This imposes an upper limit on the length of the front absorber, i.e. 4.13 m ($\sim 10\lambda_{int}$[1], $\sim 60\ X_0$[2]). It is placed at a distance of 90 cm from the interaction point, so that the measurements in the central barrel should not be affected by the presence of the absorber, and is located inside the L3 solenoid magnet. In order to minimize the small-angle multiple-scattering and energy loss by traversing muons the absorber is

[1]The nuclear interaction length, λ_{int}, is the mean path length in the material travelling through which the number of relativistic charged particles are reduced by the factor 1/e.

[2]The radiation length, X_0, is a characteristic of material which represents the distance travelled by a charged particle in losing 1/e of its initial energy.

mainly made of carbon and concrete, shown in Figure 4.3.

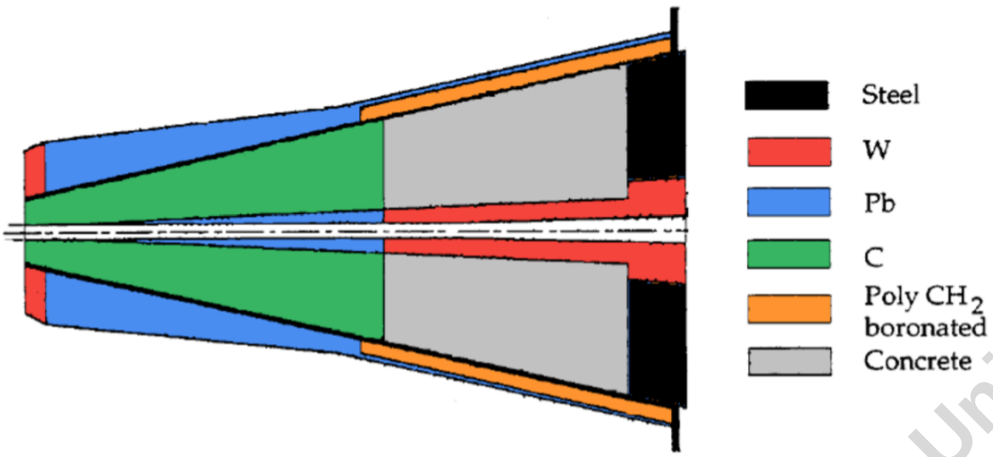

Figure 4.3: *Cross section of the front absorber of the muon spectrometer. Figure taken from [165].*

Beam shield

The secondary particles (pions and kaons in particular) interact with the beam pipe and become an important source of background. In order to reduce this background the entire length of the muon spectrometer is shielded by a dense absorber tube which surrounds the beam pipe. The tube (beam shield) is composed of tungsten, lead and stainless steel and has a conical geometry along the length of the spectrometer to reduce background particle interaction [110]. This beam shield is crucial to protect the detection chambers from primary and secondary particles produced at large rapidities.

Muon filter

Despite the fact that the two absorbers (front absorber and beam shield) are sufficient to safeguard the tracking chambers against the huge incoming hadronic background from the vertex, an additional protection is provided to the trigger chambers. As a result, the muon filter, i.e. an iron wall having thickness 1.2 m ($\sim 7.2\lambda_{int}$) is installed between the last tracking chamber and first trigger chamber. Since the muon filter is placed after the last tracking chamber, it does not affect the mass resolution of the spectrometer. The combined effect of the front absorber (stops primary hadrons) and of the muon-filter (suppresses the low-momentum muons from decays of π/K) leads to a detection threshold of $p \geq 4$ GeV/c for tracks matching the trigger.

Rear absorber

The rear absorber provides protection to the trigger chambers from the background generated by the beam-gas residual interactions produced in the LHC beam pipe. This background is directly proportional to the beam luminosity and, therefore, could not be ignored, especially during pp collisions. Now it has been extended to fully cover the tunnel aperture.

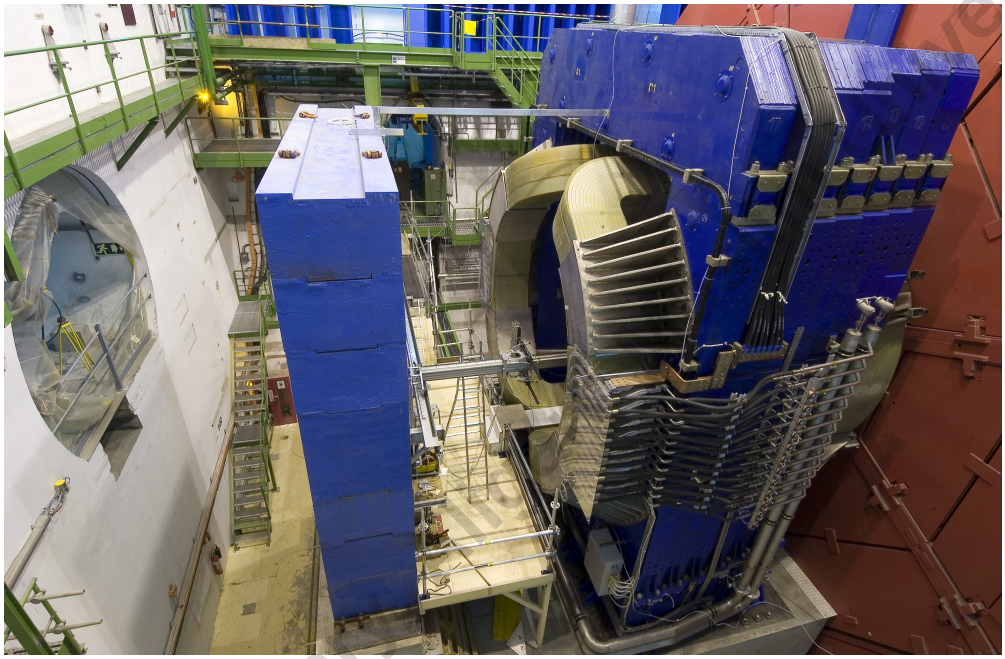

Figure 4.4: *View of the muon filter (left) and dipole magnet (right) [172].*

4.2.2 Dipole magnet

The muon arm is equipped with a large dipole magnet with resistive coils, placed outside the L3 magnet at a distance of about 7 m from the interaction point (IP). Its nominal magnetic field strength, defined by the requirements on mass resolution of the quarkonium states (70 MeV/c^2 for the J/ψ family and 100 MeV/c^2 for the Υ family), is $B_{nominal}$ = 0.7 T and the field integral along the beam axis between IP and muon filter is 3 Tm. The size, 5 m length× 7.1 m width× 9 m height weighing ~ 890 tons [83], of the dipole was determined by the requirement on the angular acceptance of the spectrometer, i.e. $171° \leq \theta \leq 178°$. The magnetic field is directed in the horizontal plane along the x-axis defining a bending plane (yz plane) and a non-bending plane (xz plane). This enables measurement of muon momenta using the tracking system.

4.2.3 Muon tracking system

The muon tracking system is comprised of five tracking stations, each with two detection or chamber planes consist of 5 mm gas gap drift Multi-Wire Proportional Chambers with segmented cathode plane, called Cathode Pad Chambers (CPC) [214]. The first two stations lie inside the L3 magnet, the third one is inside the dipole magnet and the last two stations are placed in between the dipole magnet and the muon-filter. Each chamber is made of two cathode planes and both are readout to provide two-dimensional hit information[3].

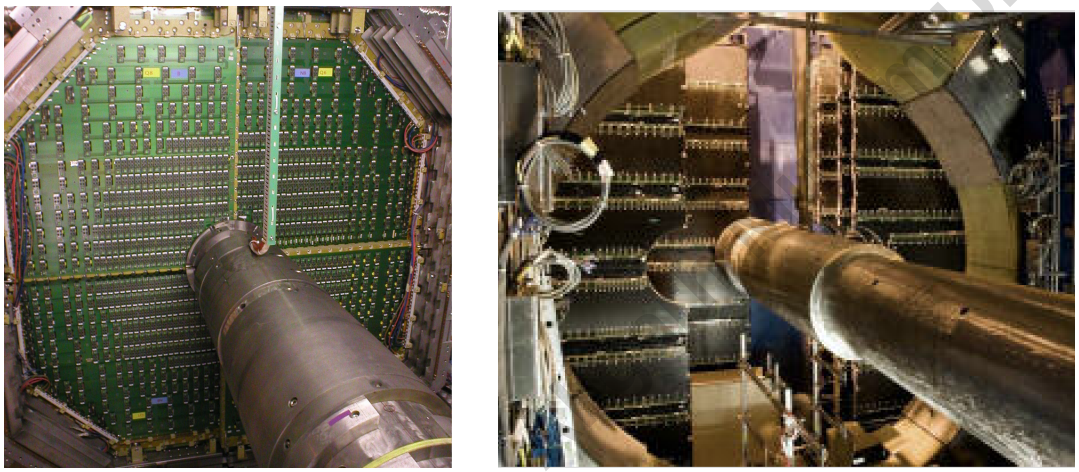

(a) *Figure adapted from [205].* **(b)** *Figure adapted from [99].*

Figure 4.5: *Cathode Pad Chambers of the station 1 (left) and layout of stations 4 and 5 (slat architecture) of tracking system of the muon spectrometer (right).*

Two main requirements which impacted the design of the tracking system were: firstly, a spatial resolution of about 100 μm for the bending plane (y direction) or momentum resolution of about 1% is needed to obtain invariant-mass resolution of the order of 100 MeV/c^2 at the 10 GeV/c^2 mass region to resolve the Υ resonance states [58, 116] and secondly, the capability to withstand high-particle multiplicity environment. However, a spatial resolution of 1 mm would suffice in the non-bending plane (x direction) to reconstruct the muon candidate track. The expected maximum hit density for most central Pb-Pb collisions were 5×10^{-2} cm^{-2}. Moreover, the whole area covered by the tracking system is about 100 m^2. All these requirements were met by the use of Cathode Pad Chambers. In order to precisely locate the exit points of the muons the first station is positioned just behind the front absorber. Highly segmented readout pads were used to

[3]Details of the tracking system can be found in [61, 90]

keep the occupancy (defined as the ratio of the number of hit pads to the total number of pads) at about 5%. For instance, pads used in the region of the first station close to the beam pipe are in area 4.2×6.3 mm^2, where the highest particle density was expected. As the hit density decreases with the distance from the beam, larger pads are used at larger radii. This had resulted in total number of channels at about one million in the entire muon tracking system.

The thickness of each chamber is about 3% of the radiation length (X_0). In order to minimize multiple scattering of the muons in the chambers, composite materials, such as carbon fibre, are used. Muon stations are of different sizes, ranging from few square metres for station 1 to more than 30 m^2 for the station 5, depending upon their positions from the interaction point. As a consequence, two different designs were adopted: the first two stations have quadrant structure [98, 107] whereas a slat architecture was chosen for the remaining three. The readout electronics is distributed on the surface of chambers in the quadrant design Figure 4.5a, while it is located on the side of the slats Figure 4.5b. The quadrants and the slats overlap to avoid dead zones on the detector.

While passing through the muon tracking chambers the particles deposit clusters of charge that are deciphered using the Maximum Likelihood Expectation Maximization (MLEM) algorithm [60] and fitted with a 2D Mathieson function [141] to ascertain their spatial location. Muon spectrometer uses tracking algorithm based on kalman filter approach to reconstruct the trajectory of particles [90, 105]. The identified muon tracks are then extrapolated to the vertex position which is measured by the ITS (in most cases SPD does this job alone). Furthermore, the effects of multiple scattering as well as energy loss of muons in the front absorber are taken into account by correcting the kinematic parameters.

Alignment of chambers: The importance of alignment of the spectrometer tracking chambers cannot be underestimated in achieving the desired invariant-mass resolution (100 MeV/c^2 in the Υ mass region). For this reason, at the beginning of each data taking period dedicated runs without magnetic field are carried out in order to align all the ten tracking chambers with straight muon tracks. This determines the initial geometry of the system. The changes, such as displacements and deformations, in the tracking chambers with respect to the initial geometry (due to any reason, including switching

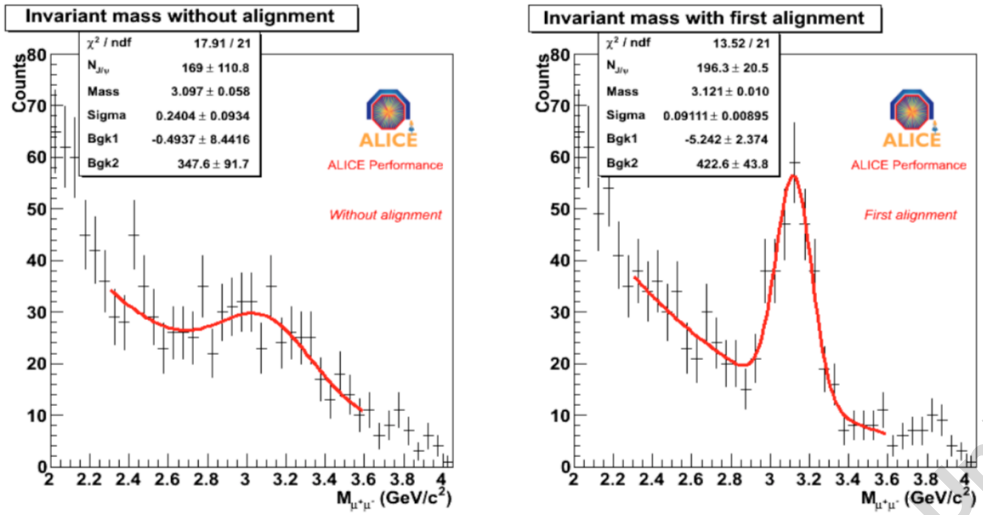

Figure 4.6: *Invariant mass spectra for opposite-sign muon pairs, which corresponds to J/ψ, before (left) and after (right) the alignment of the muon tracking system. Figure taken from [50].*

on the magnetic field and electronic power supplies) are measured and recorded during data taking by the Geometry Monitoring System (GMS). These changes are utilized during the muon track reconstruction [90, 97, 106]. The effect of alignment on the mass resolution of J/ψ is shown in Figure 4.6. A substantial improvement was observed: J/ψ resonance width decreased from 230 MeV to 90 MeV. The GMS is optimized to monitor the position of all the tracking chambers with a resolution better than 40 μm. It is an array of 460 optical sensors which are installed on platforms placed at each corner of the tracking chambers.

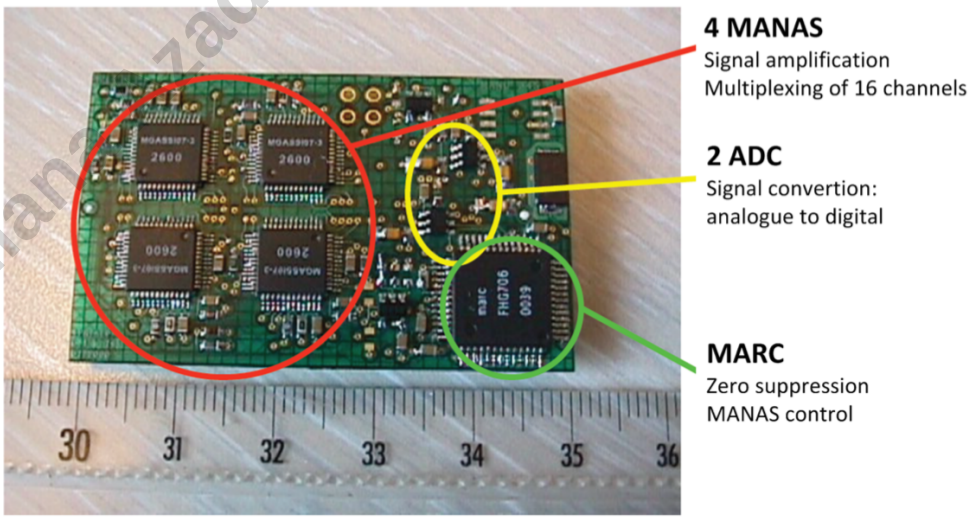

Figure 4.7: *A MANU board has 4 MANAS chips, 2 ADCs and 1 MARC. Figure taken from [165].*

Electronics and readout: The front-end electronics and boards are carefully designed to have minimum noise ($\sim 1000\ e$) along with multiple scattering. The electronics chain of the tracking system consists of three parts: the front-end boards, called MANU (MAnas NUmérique), the readout system, called CROCUS (Cluster Read Out Concentrator Unit System) and the interface with the general ALICE trigger, called TCI (Trigger Crocus Interface) [213]. The readout principle of all the five tracking stations is the same and their front-end electronics is based on a 16-channel chip called MANAS (Multiplexed ANALogic Signal processor) with the functionalities such as charge amplifier, filter, shaper, and track & hold. The signal digitization is obtained onboard. The channels of four of these chips are fed into a 12-bit ADCs, read out by the controller chip MARC (Muon Arm Readout Chip) which includes zero suppression. This whole chain is mounted on front-end boards (MANUs). The entire tracking system employs 1.08 millions channels in total, which are treated by approximately 17000 MANU cards.

The connection between the MANUs and the CROCUS crate are provided by the PATCH (Protocol for ALICE Tracking Chambers) buses. Each chamber is read out by two CROCUS. During the data acquisition phase, the main tasks of the CROCUS are to concentrate and format the data from the chambers, to transfer them to the ALICE DAQ (Data Aquisition)as well as to control front-end electronics, including calibration and dispatching of the trigger signals. A CROCUS can read up to 50 PATCH buses with a chamber occupancy up to 5%, with rates of the order of kHz.

The trigger signals, coming from the Central Trigger Processor (CTP), are distributed to the front-end electronics through the CROCUS by the TCI. The main goals of the TCI are to decode the trigger signal, to generate the L1 reject in the FFT board (Frontal Fan-out Trigger) and to manage the busy signals of all the CROCUS crates.

4.2.4 Muon trigger system

Simulation studies show that in a central Pb-Pb collision about eight low-p_T muons from the decay of pions and kaons (per event) are likely to be detected in the muon spectrometer [16], as shown in Figure 4.9. These low-p_T muons are the main source of background. In order to minimize the possibility of triggering on events which do not have any high-p_T muon emitted either in the decay of heavy quarkonia or in the semi-leptonic decay of open charm and beauty, a hardware cut on each individual muon

p_T is applied [206]. Trigger electronics implements two cuts (low-p_T and high-p_T) in parallel [149].

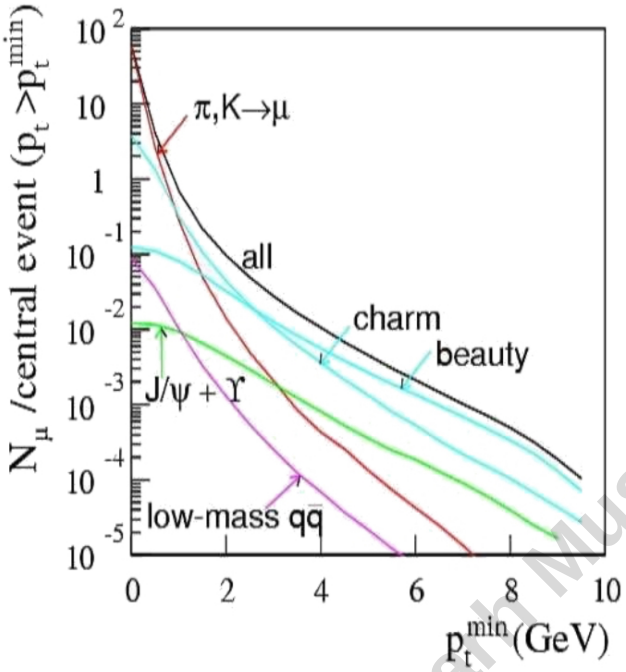

Figure 4.8: *Average number of muons with $p_T > p_T^{min}$ produced at forward rapidity in a central Pb-Pb collision as a function of p_T^{min} . The different sources of muon are also shown. Figure adapted from [16].*

The muon triggers are implemented at Level-0 only and are as follows:

- MSL: at least one muon has p_T above low-p_T threshold
- MSH: at least one muon has p_T above high-p_T threshold
- MUL: Both the unlike sign muons have p_T above low-p_T threshold
- MLL: Both the like sign muons have p_T above low-p_T threshold

All the above were used in coincidence with MB[4]. The MUL was used for the measurements of mesons and was complemented by the MLL for the estimation of combinatorial background. The low and high-p_T thresholds may take values 0.5–1.0 GeV/c and 1.7–4.2 GeV/c respectively, depending upon the type of run. However, during LHC Run 2 the single-muon high-p_T threshold was set to 4.2 GeV/c, whereas single-muon low-p_T threshold depended on the run type. For the Pb-Pb data taking low-p_T threshold

[4]Minimum Biased triggers (MBand and MBor)

was kept at 1.0 GeV/c. The threshold cuts for low-p_T and high-p_T are so chosen that the signal detection efficiency could be maximized in conjunction with background rejection in the mass region of charmonium and bottomonium families resonances.

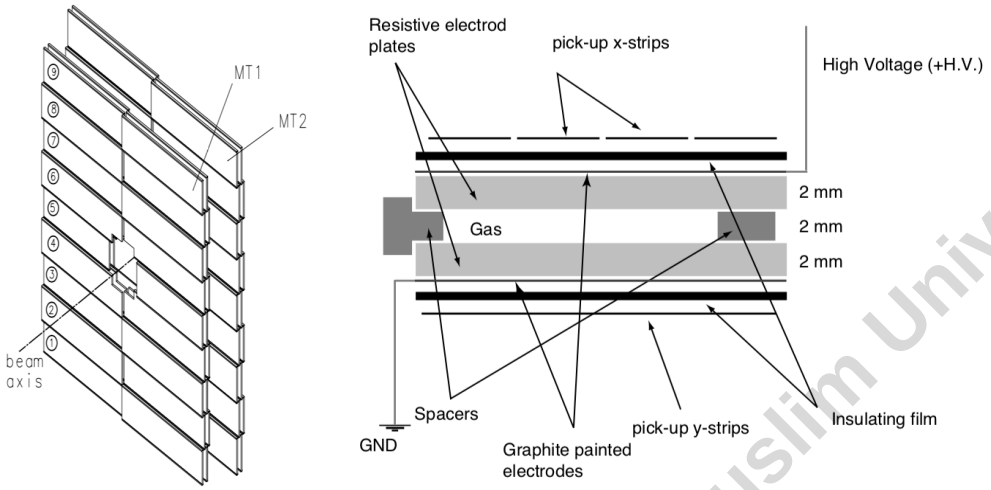

(a) **(b)**

Figure 4.9: *Layout of ALICE muon trigger detectors (left). Schematic view of a RPC cross-section (right). Figures adapted from [19].*

In order to implement the aforementioned p_T cuts on muons, a high resolution (better than 1 cm) position-sensitive detector was required for the trigger. These requirements could be well achieved by the Resistive Plate Chambers (RPCs) [187]. The RPC are gas-gap parallel plate detectors, shown in Figure 4.9b, which has good space as well as time resolution and suitable for fast space-time particle tracking. It can be operated in two modes, i.e. streamer mode and avalanche mode, by changing the gas mixture and varying the high voltage across the electrodes [184].

- The streamer mode is appropriate for high-multiplicity Pb-Pb collisions. A large signal amplification is obtained in this mode. Nevertheless, it leads to fast ageing of the detector.

- The avalanche mode is employed during high-luminosity pp collisions. In this mode, detector has very good time resolution. Also, it has slower ageing as compared to streamer mode.

Nonetheless, the muon trigger currently operates its RPCs in “highly-saturated avalanche mode” , which means that the electric field is not high enough to qualify to be

called as streamer mode, but the signal generated by the avalanche is still significant and does not require amplification.

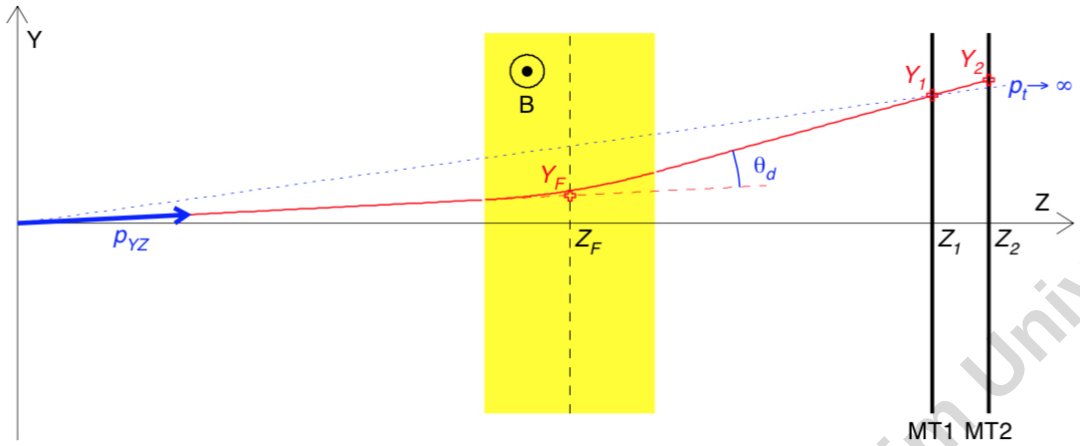

Figure 4.10: *Schematic diagram of muon trigger principle [19]. Details are discussed in text.*

The spectrometer has two trigger stations (MT1 and MT2) each with two RPC planes. Both the stations, separated by one meter, are located behind the muon filter and are at a distance of 16m and 17m from the IP. 18 RPC modules constitute one plane with an active area of about 30 m^2 [207]. The typical size of a single module is $\sim 70 \times 300$ cm^2. Also, in order to achieve a time resolution of 1-2 ns, necessary for the identification of bunch crossing, the muon trigger system is equipped with non-amplified front-end electronics called A DUaL-Threshold (ADULT) [185, 186].

The muon trigger measures the angle of deviation θ_d[5], shown in Figure 4.10. θ_d is the angle between an arbitrary muon track deflected by the dipole magnetic field and the trajectory of the muon of infinite momentum (straight line). The basis of trigger principle of p_T cut is that larger the deviation angle (or larger the distance between Y_F and the $p_T \to \infty$), lower the p_T of the track.

[5]The deviation angle θ_d and the track coordinates $(X_1, Y_1, Z_1, Y_2, Z_2)$ are related as

$$\theta_d = \frac{1}{Z_F}\left(\frac{Y_1 Z_2 - Y_2 Z_1}{Z_2 - Z_1}\right)$$

where

Z_1, Z_2, and Z_F are the positions of MT1, MT2 and middle of dipole magnet with respect to the vertex along the beam axis respectively. Y_1 and Y_2 are the Y coordinates of the position where the muon crosses on MT1 and MT2.

Part III

Data analysis

5 Identification of unexpected chamber efficiency issues

The previous chapter dealt with muon spectrometer in detail. However, the subject of this chapter pertains to the tracking chambers of the spectrometer. In order to identify the unexpected chamber efficiency issues, single-muon simulations were performed and the discrepancies were pointed out by comparing cluster maps generated from the real data and MC[1]. The results obtained to date are available on the dedicated TWiki page "Monitoring the data/MC agreement of tracking chamber status maps" [65] created for this service task[2].

5.1 Motivation

While making tracking efficiency calculations it must be ensured that the status of all the tracking chambers during real data taking should be perfectly reflected in realistic MC simulations. The purpose of this service task [65] was to track "unexpected" detector issues which are not well reproduced in simulations, thus biasing acceptance×efficiency ($A \times \varepsilon$) corrections, and consequently, result in large tracking systematic uncertainties.

[1] Monte Carlo

[2] The work presented in this chapter was carried out as service work for the ALICE Collaboration. It is mandatory, as per ALICE Constitution and publications rules – 08.11.2012, for every PhD student to provide six months equivalent of service work for the Collaboration before he/she can get a PhD thesis using the ALICE experiment.

In other words, the goal is to make the realistic simulations as realistic as possible.

The status map, summarizes the actual status of the detector during data and Monte Carlo (MC) reconstruction, is used to discard the problematic pads. This map is built using informations stored in the Offline Conditions Data Base (OCDB) such as detector configuration, HV[3], pedestal, occupancy, etc., on which cuts are applied as defined in recoParam (e.g. Manu occupancy too high, HV too low, etc.). Nonetheless, some of the detector issues, for instance, cable swapping or a bad HV connection of a PCB[4], are not detected online and therefore not reproduced in the status map. For instance, nominal operating voltage supplied to the tracking chambers is 1.6 kV. There were frequent voltage fluctuations during Run 2 and the voltage drop as low as 1.4 kV was observed, and resulted in reduced efficiency of chambers. The effects of this low voltage drop could not be reproduced in MC, therefore, elements of the detector which are considerably affected are added to "RejectList" and does not included in the reconstruction process both in data and MC.

The aim of this monitoring was to spot all the issues which could not be included in the status map and investigate their origin. Furthermore, once an issue is identified, either a way is found to solve it (by fixing the detector or finding an automatic way to spot it and incorporate it into the status map) or, in the last resort, faulty elements are added to the RejectList. This RejectList is used in the reconstruction to complement the status map to discard the problematic pads. This RejectList is contained in OCDB as one of its objects. Thus, RejectList improves the description of the detector in the MC. This lowers the corresponding systematic uncertainty and, as a result, more precise $A \times \varepsilon$ corrections.

5.2 Track reconstruction in the Muon Spectrometer

The track reconstruction process in the muon spectrometer has already been briefly discussed in the Section 4.2.3. This section will further elaborate on this and presents whole picture of tracking algorithm. As the particles leave cluster of charges, detected by chamber pads, while passing through the tracking chambers, their position is ascertained by the 2D Mathieson function [141]. After the cluster distribution is completed in all the chambers, the track reconstruction begins with the joining of these clusters of the

[3]HV stands for High Voltage.
[4]PCB stands for Printed Circuit Board.

last two tracking stations, i.e. 4 & 5 where the hadronic background is minimum as compared to other tracking stations. The straight lines connecting clusters on the two chambers of each station gives a rough estimate of position, bending momentum and direction (assuming that the particle was originated at the vertex). Thereafter, tracks are extrapolated between the two stations by pairing at least one cluster. While extrapolation, if one track corresponds to more than one cluster, then the track is duplicated and all the possible combinations are explored. Tracks sharing the same clusters and fall outside the detector acceptance are rejected. Also, the track parameters are computed at every step using the Kalman filter.

Then the tracks are extrapolated to station 3 to station 2 and finally to station 1, and for every station the entire process is repeated. If, for any track, corresponding cluster is not found or track parameters don't lie within the acceptance of the detector then it is eliminated. Finally the leftover tracks are extrapolated to the vertex determined by the SPD by taking into account the effect of multiple scattering and energy loss in the front absorber.

The tracks reconstructed through the tracking chambers are matched with their counterparts in the Muon Trigger. This would exclude fake tracks. For a track to be reconstructed in the Muon Trigger at least 3 chambers out of 4 are to be hit. On the other hand, reconstruction of a track in the Muon Tracker requires at least one chamber hit per station for the stations 1, 2 & 3 and 3 out of 4 chamber hits for station 4 & 5. The aforementioned track selection criteria are utilized while pointing out the discrepancies between the cluster maps from the data and MC. For physics analyses, a set of additional selections are applied, which is to be discussed in the next chapter.

5.3 Procedure

5.3.1 Overview

In order to spot these issues, the distribution of the clusters attached to the reconstructed tracks (also known as cluster maps) are compared, run-by-run and chamber-by-chamber, from data and MC simulations. The basic idea behind this comparison is that if all the defects are spotted in the status map, we should observe no difference in the cluster maps from data and realistic MC simulations. On the other hand, if we see differences, it

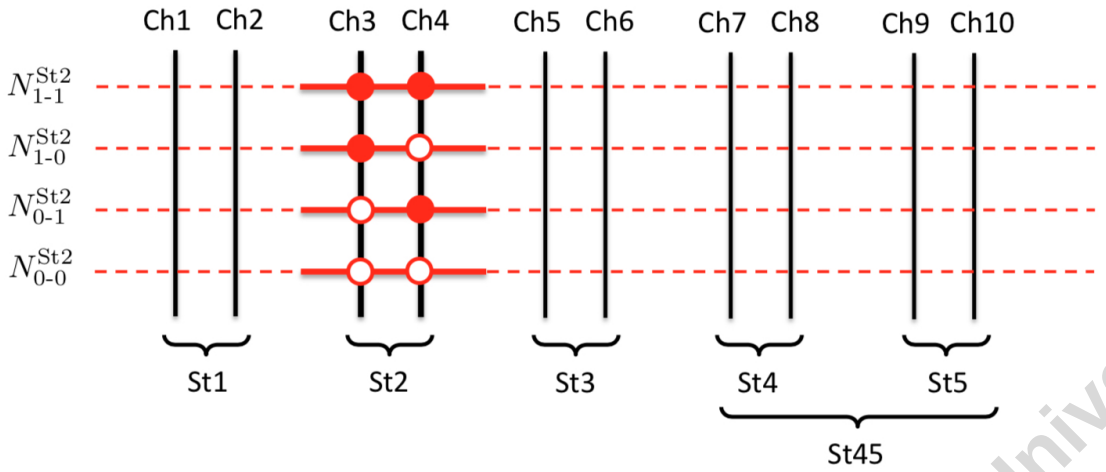

Figure 5.1: *Schematic diagram representing arrangement of different muon tracking stations possessing two chambers each. One possible response of station 2 to the passage of particle is shown. Figure adapted from [41].*

means that there are some additional "unexpected" defects not discarded, or not properly discarded, by the status maps or the current RejectList.

Following the aforementioned idea, the realistic single-muon simulations were performed. These simulations were roughly tuned to reproduce the muon distributions in the data. This tuning of simulations with data was done with two purposes. Firstly, it eases the comparison, and secondly, they can also be used further in the tracking efficiency systematics studies.

5.3.2 Whereabouts of cluster maps

The cluster maps for real data are produced by the QA[5] task and are stored in the `QAresults.root` files. The QA task run immediately after the reconstruction and the results are merged run-by-run afterward.

However, the cluster maps for the MC data can be taken directly from the reconstruction QA present in the `Merged.QA.Data.root` files. It requires to enable the MUON QA in the reconstruction macro and to merge the `Merged.QA.Data.root` files run-by-run afterward if the simulation is split in several jobs.

[5]Quality Assurancee

5.3.3 Single-muon simulation and merging of the QA results

Simulation code was generated and submitted to the AliEn grid using the AliMuonAccEffSubmitter facility, committed in $ALICE_PHYSICS/PWG/muondep. It is based on template files (located in $ALICE_PHYSICS/PWG/muondep/AccEffTemplates) which contains several variables that are replaced by the customized configuration settings of the submitter. In this way changes were made in the OCDB settings, switch between different generators, select the output files we want to save/merge, etc.

For the purpose of illustration, a configured AliMuonAccEffSubmitter for single muon simulation, namely `SubmitSingleMu.C`, is available on the twiki page. There are numerous variables to play with, some of them are mentioned below:

- Number of events per run can be generated by using the reference trigger and proportionality factor or can be fixed to some value.
- Adjust the parameters of the p_T/y generation functions (functions are given in `GenParamCustomSingleBen.C`)
- Change the minimum p_T cut for the efficiency task
- Adjust the alignment by changing the OCDB configuration
- Choose the AliPhysics version as per our choice

There were different modes available to run the macro. Some of them are given below:

- LOCALTEST: This mode generates files in local directory and run the full simulation chain locally (it was configured to generate 100 events)
- FULL: It generates the files, copy them to the specified AliEn directory, and launch the jobs on the grid for the given run list
- TEST: This mode is same as FULL but without actually submitting the jobs on the grid
- MERGE:xxx: It launches the xxx step of merging on the grid (step 0 = final merging per run)

Period	No. of runs	No. of chambers
LHC16e	22	220
LHC16f	20	200
LHC16g	16	160
LHC16h	81	810
LHC16i	19	190
LHC16j	50	500
LHC16k	174	1740
LHC16l	71	710
LHC16m	42	420
LHC16n	63	630
LHC16p	42	420
11 periods	600	6000

Table 5.1: *The periods for which cluster maps are analysed. All periods correspond to pp data at $\sqrt{s} = 13$ TeV taken in 2016.*

5.3.4 Production of cluster maps comparison plots

The macro, i.e. `SaveQA.C`, to produce comparison plots is available on the twiki page. Depending upon the reconstruction parameters for a given period, it can be set to LowMultiplicity or HighMultiplicity. The path to the directory is mentioned to find maps in the root file. The macro takes two input parameters, two list of QA files with their full path corresponding to data and MC. The files are accessible directly from the AliEn by prepending the path by alien://, such as
`alien:///alice/data/2016/LHC16e/000253488/muon_calo_pass1/QAresults.root`.

In principle, for better comparison of maps, the total number of MC simulated events per run should be two times the number of triggers in data. Nevertheless, because of limited availability of quota on the AliEn grid, i.e. a limit on the number of jobs, CPU and running time quota, a fixed number of events (400000) per run, independent from the number of events in data, was simulated. The minimum p_T^{min} threshold was kept at 0.8 GeV/c. There were total 11 periods of the 2016 pp data at $\sqrt{s}$ = 13 TeV for which cluster maps were generated and discrepancies were pointed out. For LHC16k period central simulation was performed because of very large number of runs. The MC simulations were performed using raw/full alignments. More than six thousand

cluster maps dispersed over 11 periods were analysed. All the periods for which cluster maps were generated and compared are summarized in Table 5.1. In order to spot the discrepancies every chamber was analysed run by run for the whole period.

Correlated Dead Area (CDA)

Following up the discussion of Section 5.2 on chamber hits requirement for track reconstruction, consider a case if there are 2 aligned holes, one in each of the 2 chambers of a station, none of the tracks crossing this region of the detector can be reconstructed, which would also be reflected on the cluster distributions on other chambers (only clusters attached to a track are displayed to remove background). These shadows are more prominent in MC than in data because the MC tracks have a higher p_T threshold and all come from the vertex, therefore, they have more similar trajectories than the tracks in data [183].

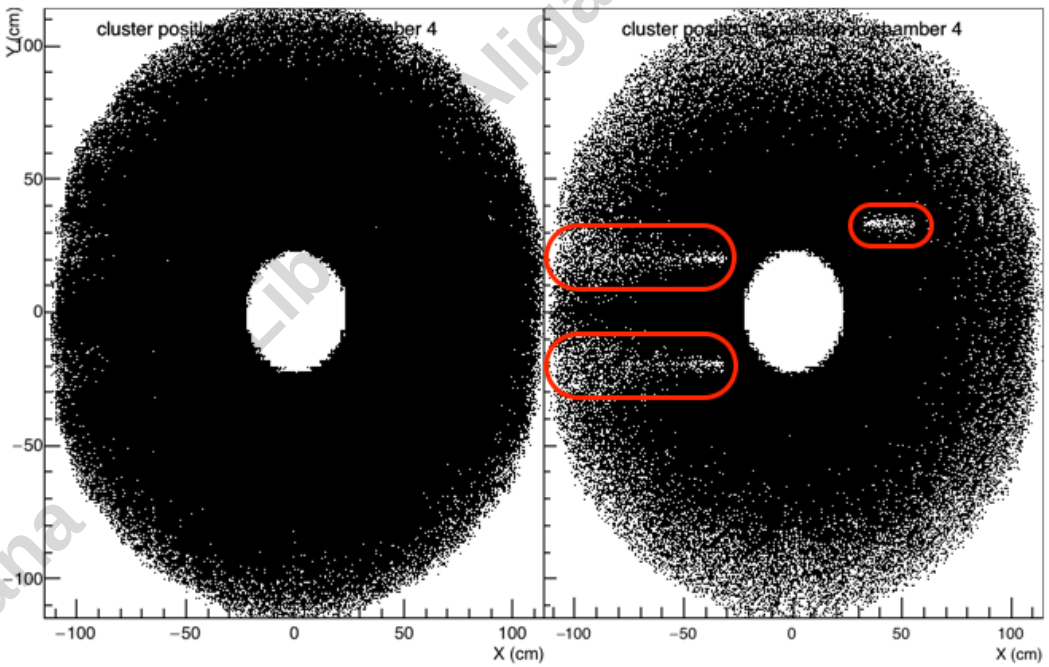

Data MC

Figure 5.2: *Cluster map shown in this figure is a manifestation of correlated dead area. This map of chamber 4 belongs to run 253563 of LHC16e period.*

As briefly explained in Section 5.1, these maps are utilized in systematics evaluation of tracking efficiency measurements and contributes to the uncertainty, among many others, in $A \times \varepsilon$ corrections. For the purpose of illustration, several cluster maps with

major discrepancies between the data and MC are included here.

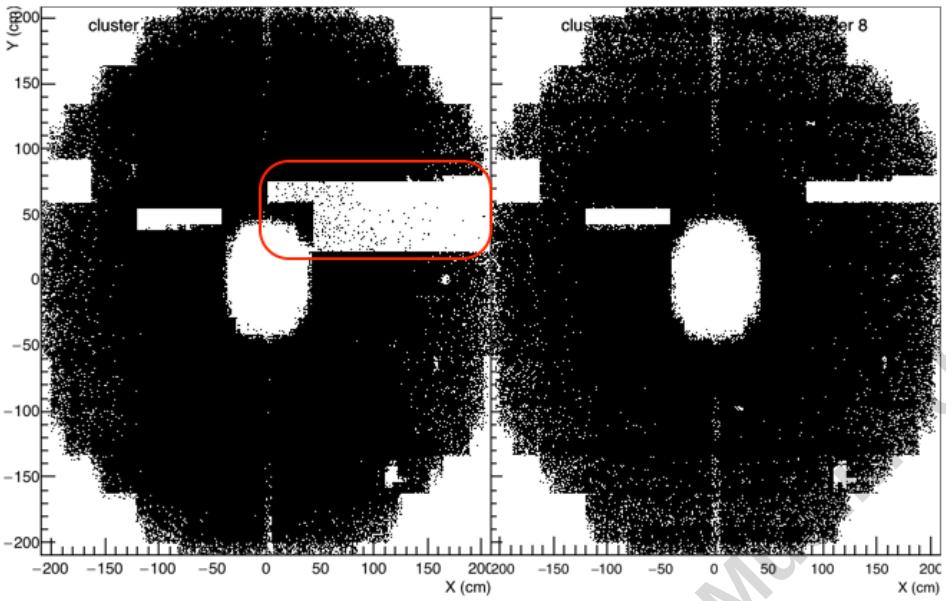

Data MC

Figure 5.3: *Cluster map of chamber 8 which corresponds to run 256589 of LHC16k period. The aforementioned period was declared as bad run in the Run Condition Table (RCT), thereby, not fit for physics analysis.*

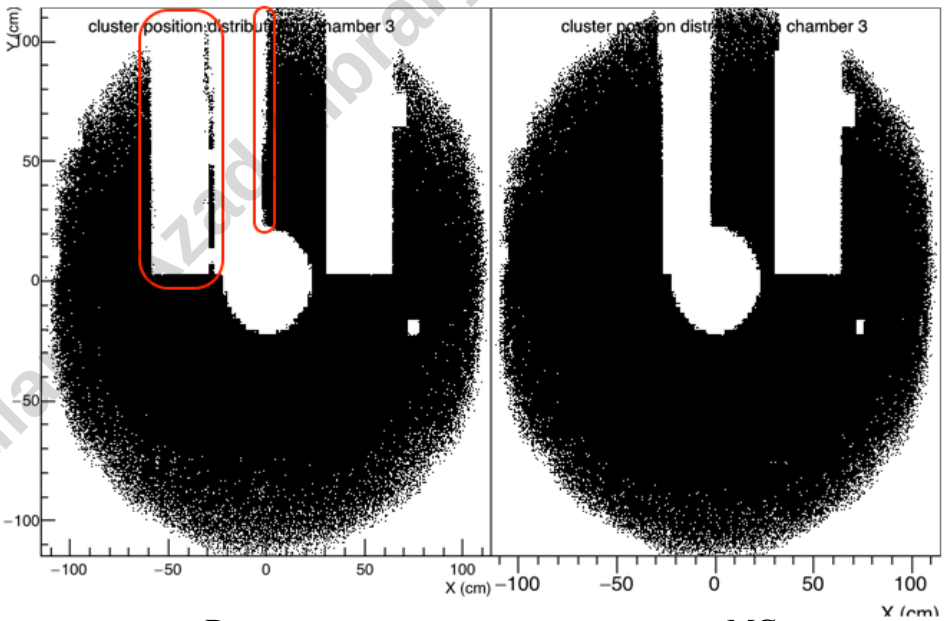

Data MC

Figure 5.4: *Cluster map of Chamber 3. The above major problem was detected in 8 runs, namely 260700, 704, 710, 713, 722, 723, 727 and 728 of LHC16n period.*

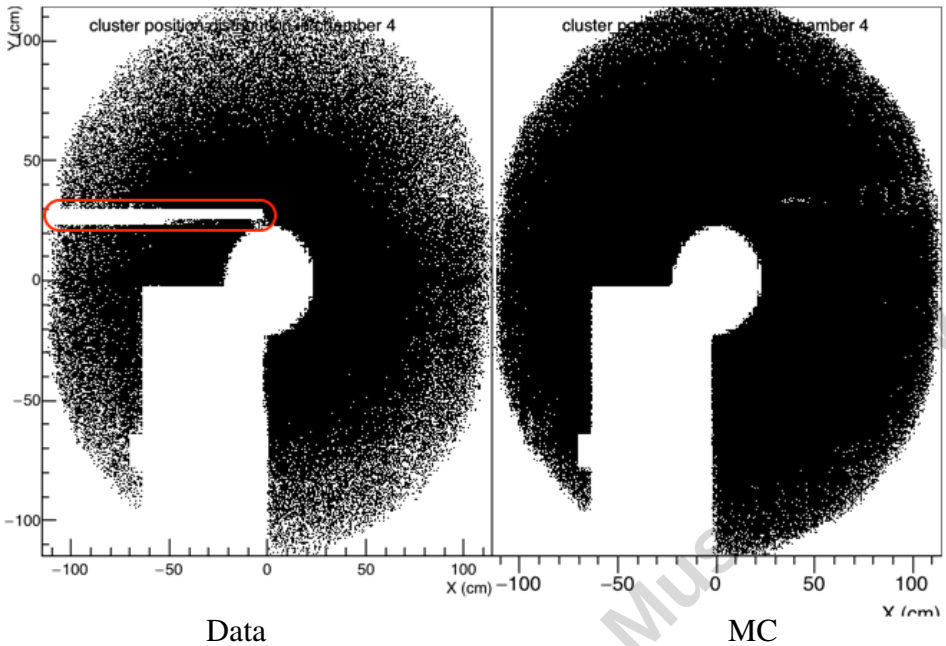

Data MC

Figure 5.5: *Cluster map of Chamber 4 corresponds to run 261095 of LHC16n period. This run was declared as bad run.*

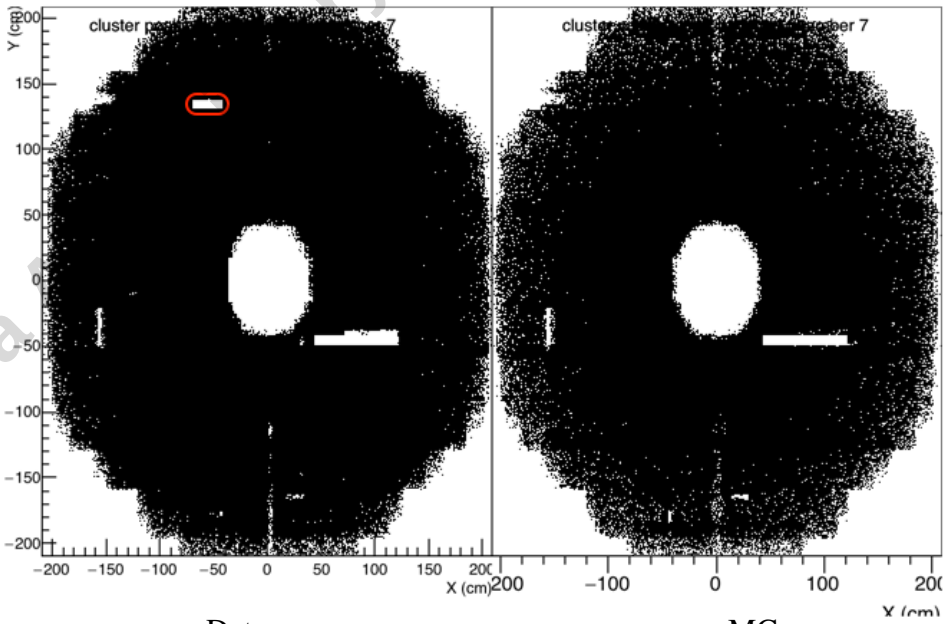

Data MC

Figure 5.6: *Cluster map of Chamber 7. The above discrepancy was identified in runs 256287 and 256289 belonging to LHC16j period. This discrepancy does not corresponds to correlated dead area.*

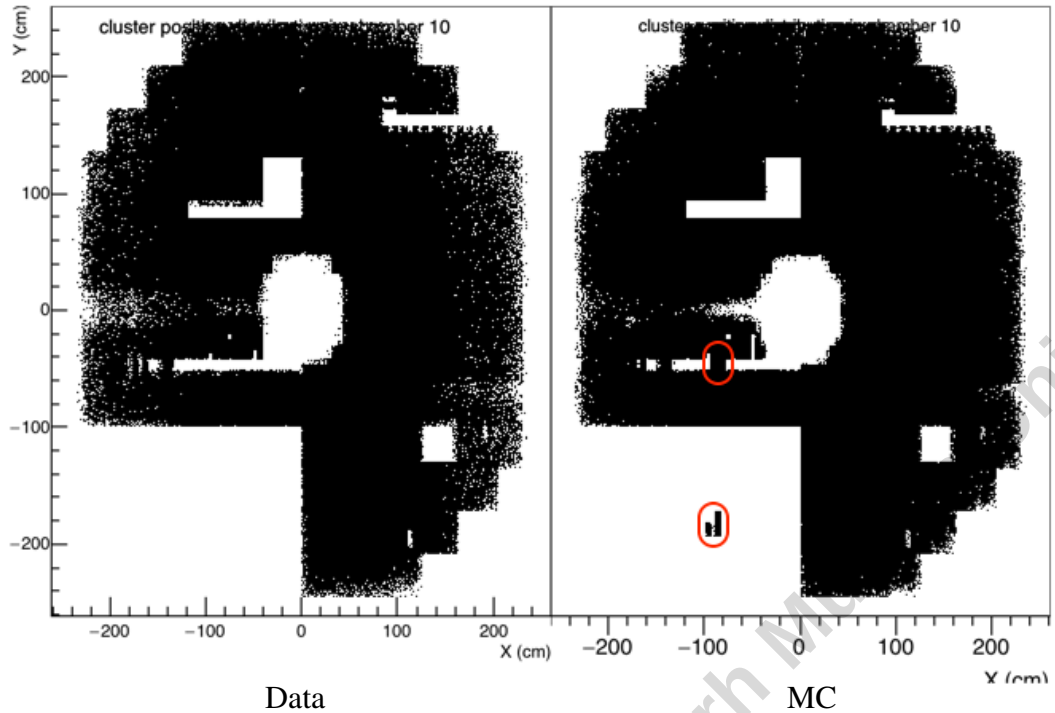

Data MC

Figure 5.7: *Cluster map of Chamber 10. Two runs 261020 and 261022 of LHC16n period have the above mismatch between the data and MC.*

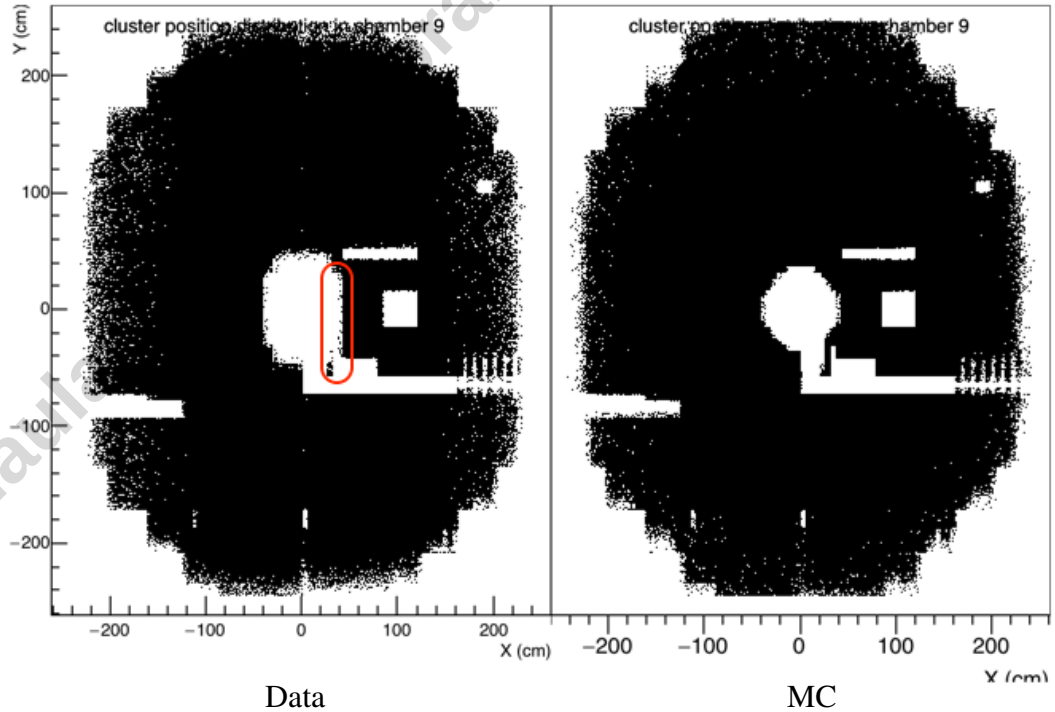

Data MC

Figure 5.8: *This map of chamber 9 corresponds to run 253756 of LHC16f period.*

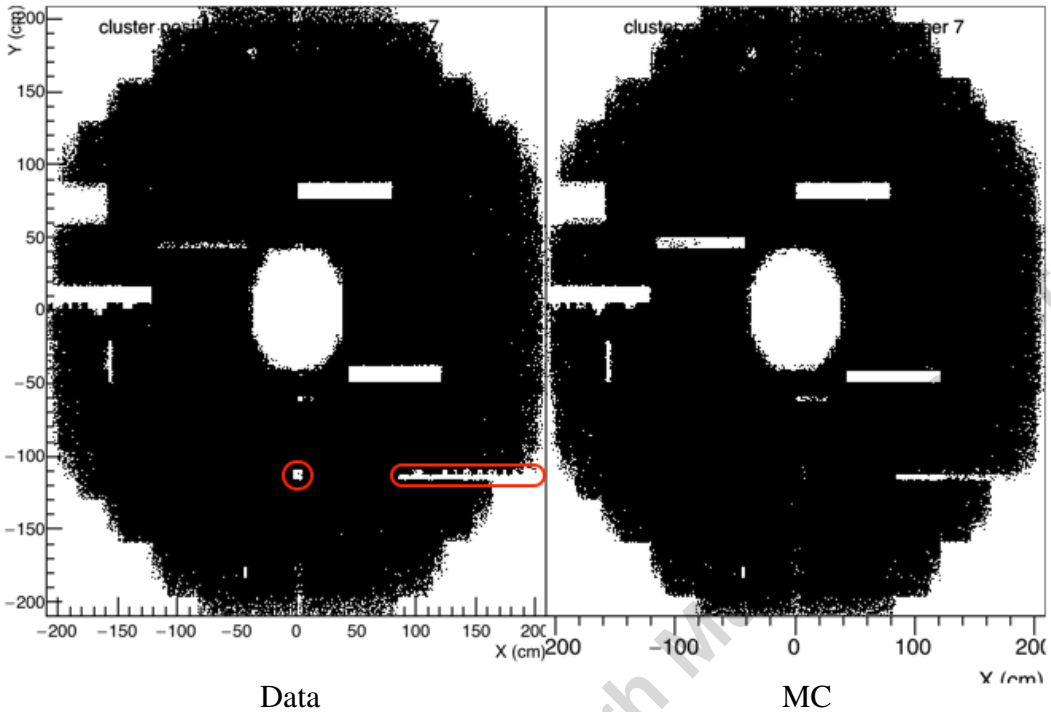

Data MC

Figure 5.9: *This cluster map of chamber 7 belongs to run 264139 of LHC16p period.*

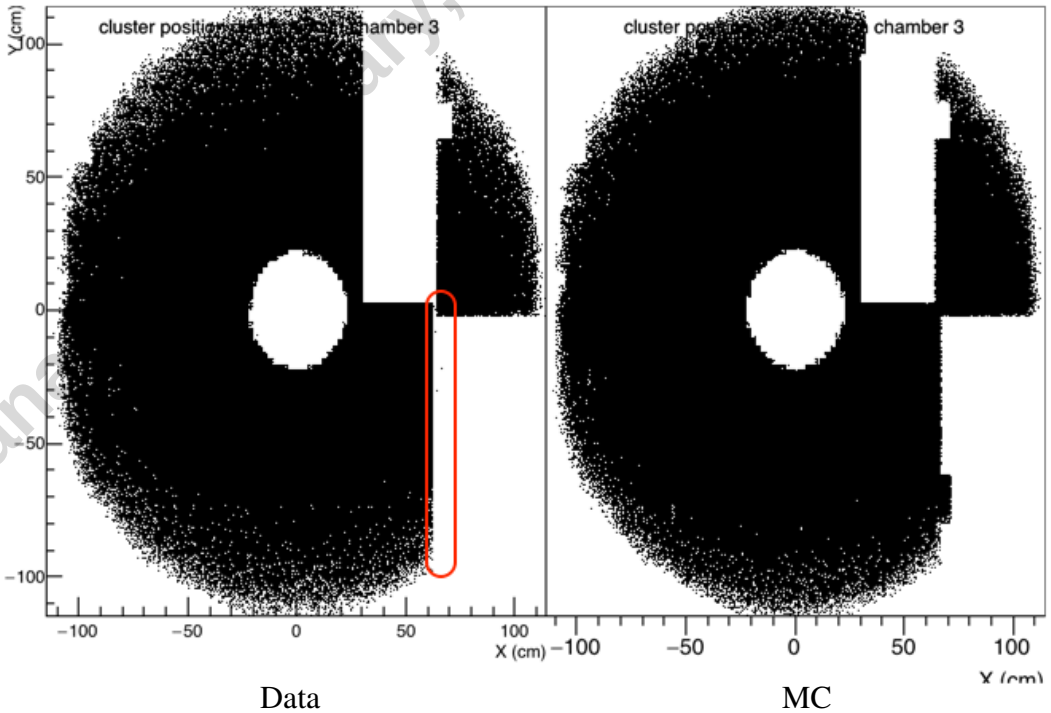

Data MC

Figure 5.10: *This cluster map of chamber 3 corresponds to period LHC16n. The affected runs with this problem were 260804, 808, 809, 810, 815, 938, 960, 963, 261020, 1022, 1026, 1027, 1052, 1055, 1065, 1076, 1083, 1088, 1093, 1094, 1095, 1099, 1100.*

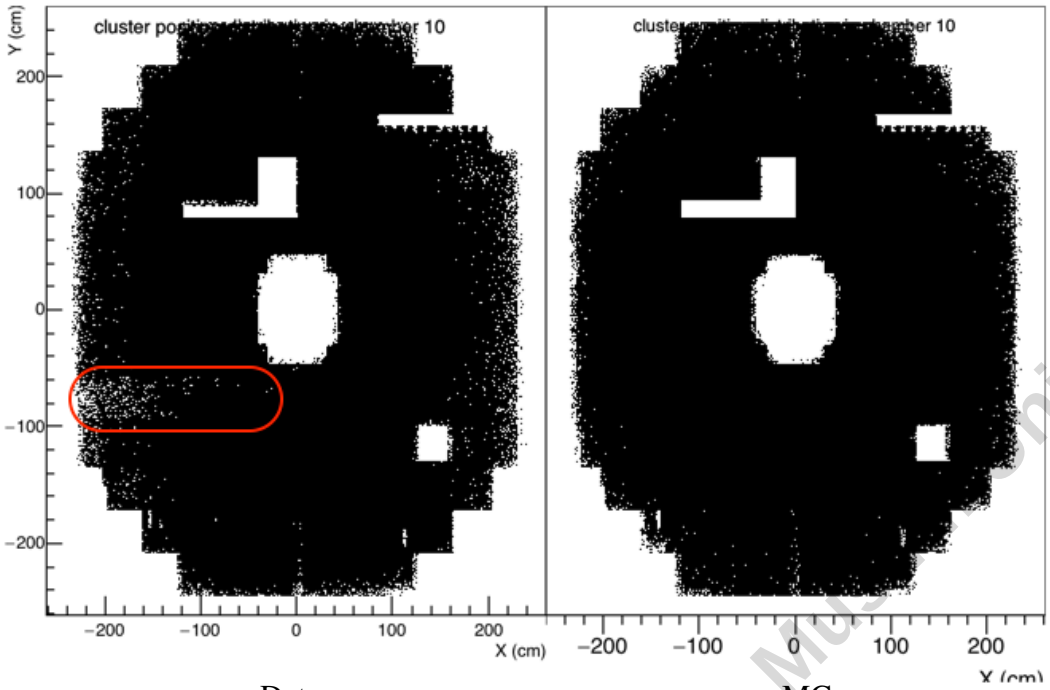

Data MC

Figure 5.11: *This cluster map of chamber 10 belongs to run 259756 of LHC16l period. This run was excluded from the list of good runs.*

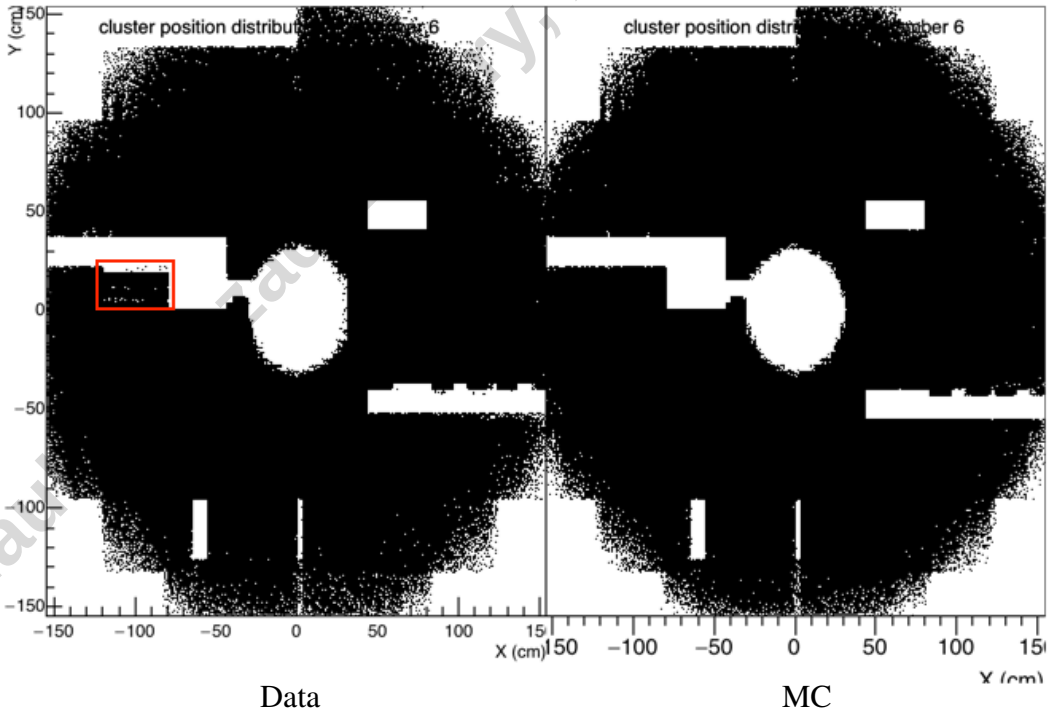

Data MC

Figure 5.12: *This cluster map of chamber 6 belongs to run 259477 of LHC16l period. However, this region has the above identified problem during many runs dispersed over the periods LHC16j, k and l. During the aforesaid periods, chamber 5 was fully efficient in this region. Also, this problem does not correspond to correlated dead area.*

6

J/ψ production at very low-p_T in peripheral Pb-Pb collisions

This chapter is dedicated to the study as well as analysis details of low-p_T J/ψ in peripheral Pb-Pb collisions. The excess yield in the J/ψ production at low-p_T (< 300 MeV/c) was observed for the first time in Pb-Pb collisions at $\sqrt{s_{NN}} = 2.76$ TeV [95].

6.1 Determination of centrality

Usually, nucleus-nucleus collisions are expressed in terms of centrality, a key concept in the field of heavy-ion physics. It is directly related to the impact parameter[1] b, in turn, number of nucleons participating in the collision N_{part}[2]. In addition, the number of spectator nucleons are defined as $N_{spec} = 2A - N_{part}$, where A is the mass number of nucleus. The dependence of N_{part} and N_{coll}[3] on b in nuclear collisions is commonly expressed by the Glauber model [168, 190–192].

The ALICE employs two methods for the determination of centrality. This section briefly describes the popular one, considered as standard method, and is used in physics

[1] defined as the distance between the centers of two colliding nuclei in a plane transverse to the beam axis [74].

[2] A participant nucleon of a nucleus undergoes at least one binary collision with nucleons of the other nucleus [74, 94].

[3] It represents number of binary nucleon-nucleon collisions. For a given value of b, it is determined by using a realistic initial distribution of nucleons inside the nucleus and assuming that nucleons follow straight trajectories.

analyses of the ALICE [62]. It uses the V0M[4] distribution fitted with the Monte Carlo Glauber model. The centrality is commonly expressed as a percentage of the total nuclear interaction cross section σ [168]. "In ALICE, the centrality is defined as the percentile c of the total hadronic cross section σ_{AA} corresponding to a particle multiplicity above a given threshold (N_{ch})" . However, for simplicity, number of observed events can be used instead of cross section.

$$c \approx \frac{1}{\sigma_{AA}} \int_{N_{ch}}^{\infty} \frac{d\sigma}{dN'_{ch}} dN'_{ch} \approx \frac{1}{N_{ev}} \int_{N_{ch}}^{\infty} \frac{dn}{dN'_{ch}} dN'_{ch} \tag{6.1}$$

where N_{ev} is the total number of events.

The events are classified into different centrality classes using the summed amplitudes of the signals in V0A and V0C detectors[5]. In order to reproduce the experimentally observed particle multiplicity distribution, the Glauber Monte Carlo[6] [12, 209] is coupled with a model of particle production based on the concept of "ancestors" , i.e. independently emitting sources of particles. The number of ancestors $N_{ancestors}$ are parameterized by $N_{ancestors} = f \times N_{part} + (1 - f) \times N_{coll}$, inspired by two-component models [138, 224], where $f \sim 0.8$ quantifies the relative contribution of N_{part} & N_{coll}. The particle multiplicity per nucleon-nucleon collision is distributed according to a negative binomial distribution (NBD), parametrized with μ and k, where μ is the mean multiplicity per nucleon-nucleon collision and k controls the contribution at high multiplicity. The Glauber Monte Carlo defines, for an event with a given impact parameter b, the corresponding N_{part} and N_{coll}. In the Monte Carlo Glauber calculation, the position of nucleons, irrespective of proton or neutron, inside the ^{208}Pb nucleus is modeled by the modified Woods-Saxon or two-parameter Fermi distribution:

$$\rho(r) = \rho_0 \frac{1}{1 + \exp\left(\frac{r-R}{a}\right)} \tag{6.2}$$

where ρ_0 is the nucleon density (not relevant for the MC simulation), R is the radius of ^{208}Pb nucleus and a is its skin thickness. Based on data from low-energy electron-nucleus scattering experiments [153], the values of R and a are 6.62 ± 0.06 fm and 0.546 ± 0.010 fm respectively.

[4] the sum of the amplitudes in the V0A and V0C.
[5] Details of the method used are given in [34, 74].
[6] Full description is given in [74].

For $\sqrt{s_{NN}}$ = 5.02 TeV collisions, the value used for the inelastic nucleon-nucleon cross-section σ_{NN}^{inel} is 70 ± 5 mb, which was estimated by interpolation of pp data [76]. However, the ALICE has recently renewed its value of σ_{NN}^{inel} to 67.6 ± 0.6 mb from 70 ± 5 mb [43]. The geometric overlap function T_{PbPb} is calculated as $T_{PbPb} = N_{coll}/\sigma_{NN}^{inel}$ thereafter, following notations of [168], representing the effective nucleon luminosity in the collision process. The V0M amplitude is well described by the NBD-Glauber fit in the region where the contamination by electromagnetic processes and effects of trigger inefficiency are negligible, which corresponds to the most central 90% of the cross section.

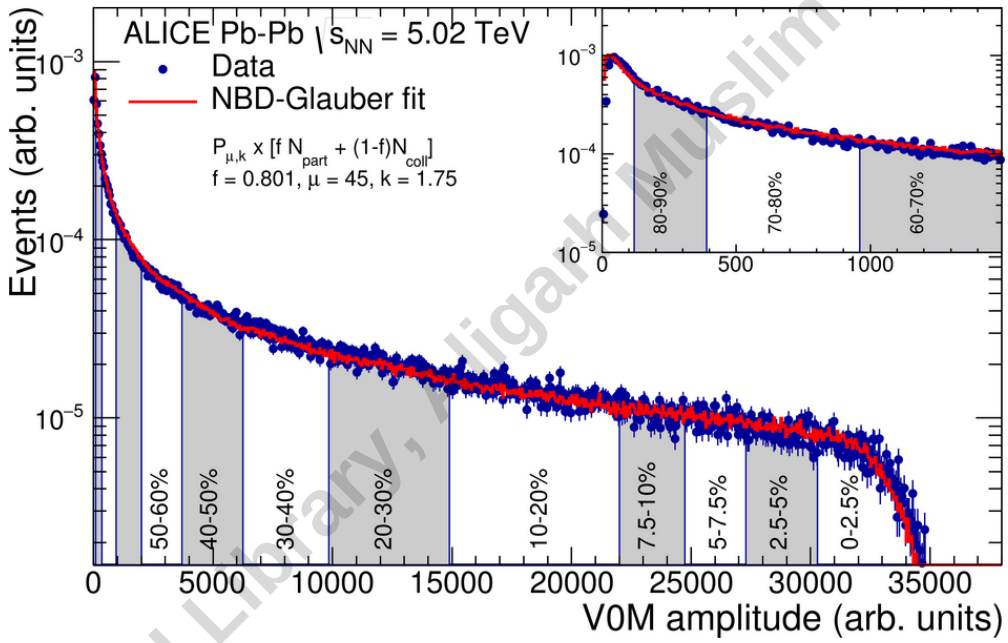

Figure 6.1: *Distribution of the sum of amplitudes in the V0 scintillator detectors (V0M), fitted with the NBD-Glauber fit. The inset shows zoomed in of the values in the lower limit region of V0M amplitude which corresponds to most peripheral region. Figure taken from [62].*

The distribution of V0M amplitudes fitted with the Glauber-NBD fit is shown in Figure 6.1. All events passing the physics selection and having $Z_{vtx} < 10$ cm are taken into account.

The mean values, the root-mean-square (RMS) as well as the systematic uncertainties of the geometric properties (N_{part}, N_{coll}, T_{PbPb}) for centrality classes defined by sharp cuts in the simulated V0M multiplicity distribution are obtained with a Glauber Monte Carlo calculation. This differs from the past practice where centrality classes were defined by cuts in the impact parameter.

Centrality	$\langle N_{part} \rangle$	$\langle N_{coll} \rangle$	$\langle T_{PbPb} \rangle$ (mb^{-1})
0-10%	357.3 ± 1.3	1569 ± 32	23.2 ± 0.43
10-30%	225 ± 2.65	781.9 ± 20	11.567 ± 0.285
30-50%	108.3 ± 3.5	261.9 ± 13	3.874 ± 0.19
50-70%	42.56 ± 1.55	65.625 ± 3.75	0.971 ± 0.054
70-90%	11.402 ± 0.435	10.971 ± 0.54	0.162 ± 0.007

Table 6.1: *For $\sqrt{s_{NN}}$ = 5.02 TeV, the mean values of N_{part}, N_{coll} and T_{PbPb} in different centrality classes considered in this thesis [36].*

For $\sqrt{s_{NN}}$ = 5.02 TeV, the mean values of number of participants $\langle N_{part} \rangle$, binary nucleon-nucleon collisions $\langle N_{coll} \rangle$ and nuclear overlap function $\langle T_{PbPb} \rangle$ for different centrality ranges used in the present analysis are given in the Table 6.1. Values are calculated for each centrality bin by combining the values given in thinner centrality bins in the [36]. The systematic uncertainties on the mean values are obtained by a Glauber Monte Carlo calculation.

6.2 Excess in the J/ψ yield at very low-p_T

The excess in the J/ψ yield at very low transverse momentum (p_T < 0.3 GeV/c) in peripheral Pb-Pb collisions at $\sqrt{s_{NN}}$ = 2.76 TeV was first observed by the ALICE Figure 6.2 [95]. The J/ψ measurement was performed through the $\mu^+\mu^-$ decay channel at forward rapidity in the muon spectrometer. The reason for this excess was attributed to the coherent photoproduction of J/ψ. The J/ψ nuclear modification factor was found to be strikingly high, i.e. 7 (2) in the p_T range 0-0.3 GeV/c in the 70%-90% (50%-70%) centrality class Figure 6.3. The photoproduction of J/ψ in ultraperipheral collisions (b[7] > 2R[8]) is a widely studied phenomenon, both at RHIC [121] and LHC [75, 84]. However, for b < 2R, coherent photoproduction of J/ψ has never been observed in nuclear collisions.

Figure 6.2 shows the p_T distribution of opposite-sign dimuons without combinatorial background subtraction in the invariant mass range 2.8 < $m_{\mu^+\mu^-}$ < 3.4 GeV/c^2 in the centrality interval 70%-90%. A notable excess of dimuons is observed in the p_T range

[7]Impact parameter
[8]Radius of colliding nucleus

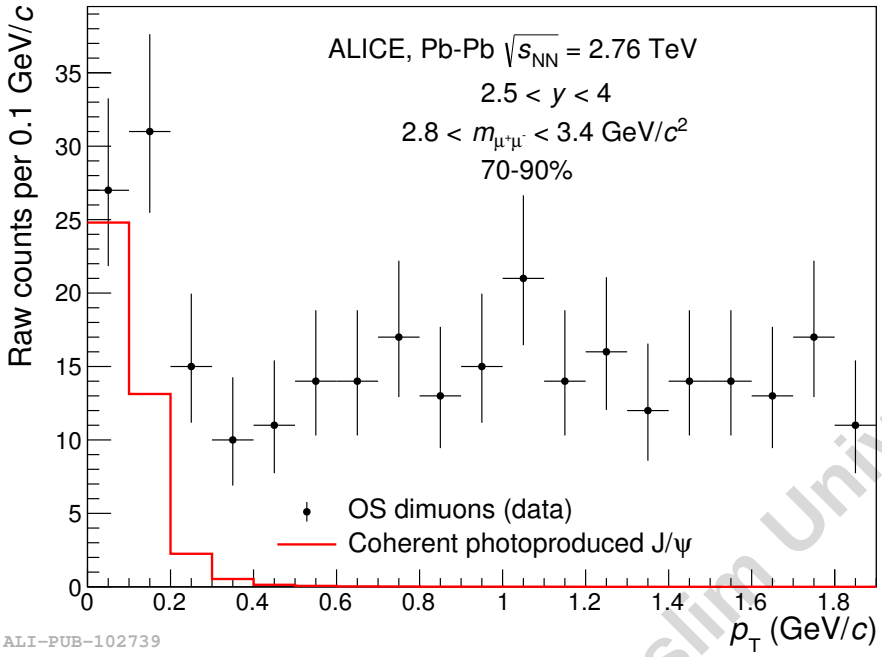

Figure 6.2: *Opposite-sign dimuon p_T distribution for the invariant mass range $2.8 < m_{\mu^+\mu^-} < 3.4$ GeV/c^2 and centrality class 70%-90%. The red line represents the p_T distribution of coherently photoproduced J/ψ as predicted by the STARLIGHT MC generator [203] in Pb-Pb ultraperipheral collisions and convoluted with the response function of the muon spectrometer. Vertical error bars are the statistical uncertainties. Figure taken from [95].*

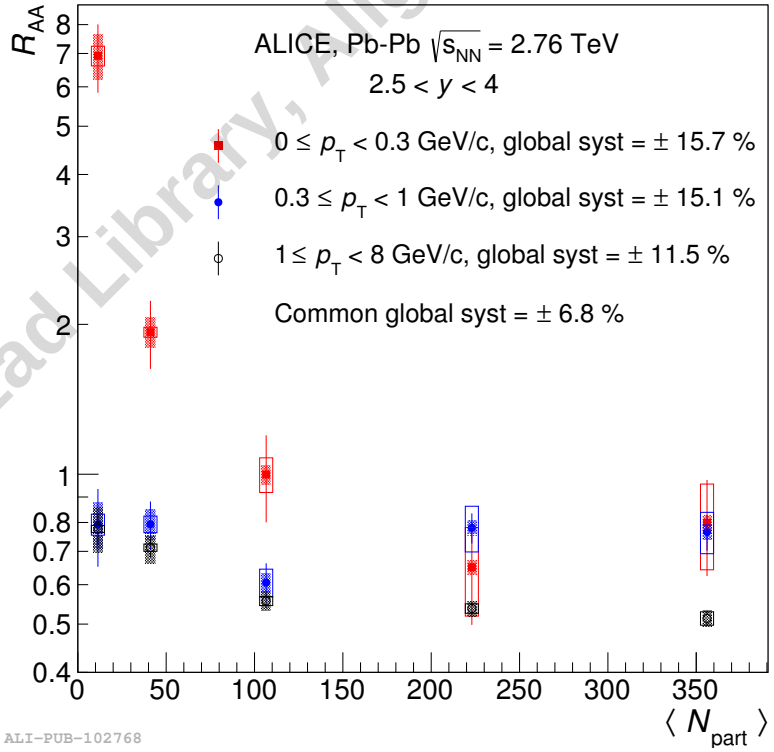

Figure 6.3: *J/ψ R_{AA} as a function of centrality for 3 p_T ranges in Pb-Pb collisions at $\sqrt{s_{NN}}$ = 2.76 TeV. Remarkable increase in the value of R_{AA} is observed in the range $0 < p_T < 0.3$ GeV/c in the most peripheral collisions [95].*

0-0.3 GeV/c in the aforementioned centrality class. It is worth mentioning that no such excess was observed neither in the like-sign p_T distribution nor in previous studies of pp collisions [70, 71, 78, 102, 114, 115]. The excess poses a challenge to the existing theoretical models which account for hadronic processes only. Moreover, it is expected that the coherent photoproduction of J/ψ occurred during the initial stage of the collisions and, therefore, could interact with the QGP. As a result, the cross section measurements may not meet the expectations of theoretical models. Precisely, partial suppression of photoproduced J/ψ in the QGP is expected due to color screening. Furthermore, the regenerated J/ψ in the QGP do not contribute to the observed excess, thereby making this study a powerful tool to constrain the models of suppression and regeneration.

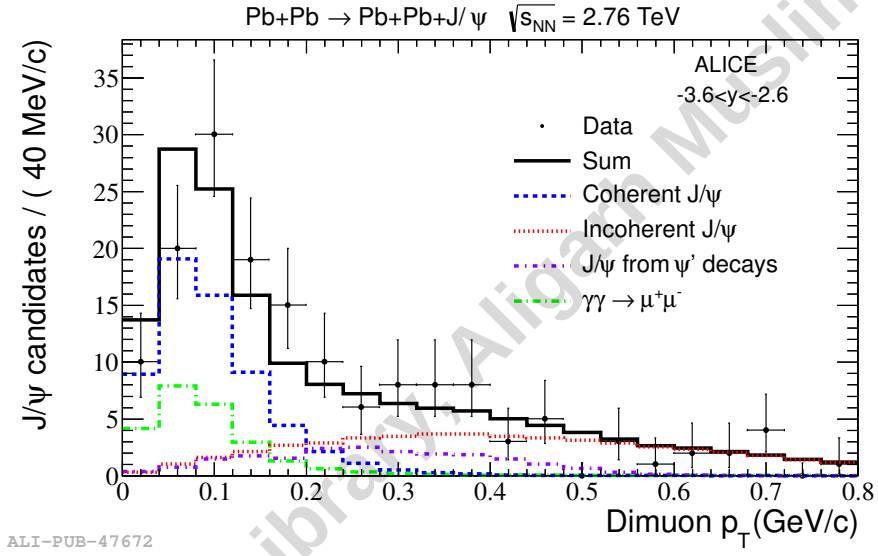

Figure 6.4: *Dimuon p_T distribution. The data points are fitted summing four different Monte Carlo templates: Coherent J/ψ production, Incoherent J/ψ production, J/ψ's from ψ′ decay, and $\gamma\gamma \rightarrow \mu^+\mu^-$ represented by dashed-blue, red, violet and green respectively. The solid black histogram is the sum [75].*

The analysis presented in this chapter is motivated by this low-p_T excess observation. The increased collision energy provides approximately 10 times larger data sample which may improve the precision of the current measurement. It would also provide the possibility to investigate this low-p_T excess in most central collisions. Furthermore, the excess in the J/ψ yield at p_T < 0.3 GeV/c in peripheral Pb-Pb collisions at $\sqrt{s_{NN}}$ = 5.02 TeV is also observed. Nonetheless, this excess is observed in the same centrality class, i.e. 70%-90% and 50%-70%, as was in Run 1 data. Clear indications of gamma-gamma background was found in the 70%-90% centrality class. It may be seen from the Figure 6.4 that there are two peaks at low-p_T, one from coherent J/ψ and another from two-photon

production of continuum pairs [75]. Thus, $\gamma\gamma$ is the dominant source of background in the at low-p_T region in the 70%-90% centrality class.

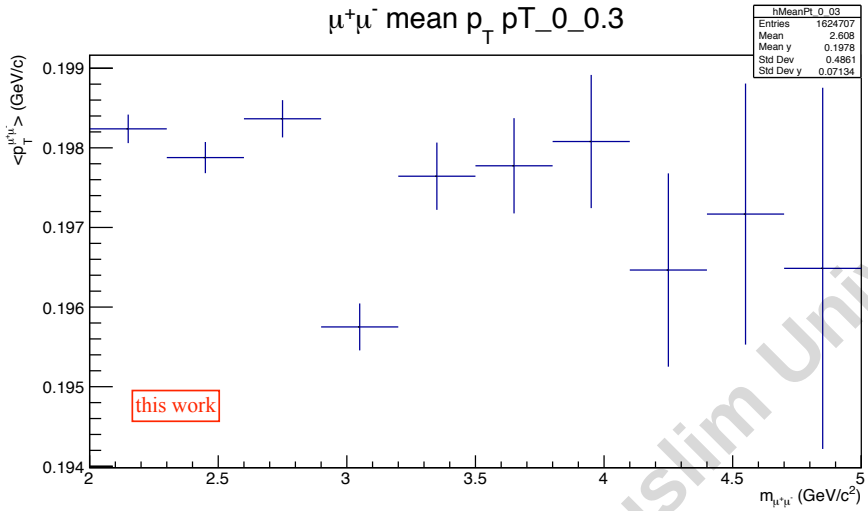

Figure 6.5: *Opposite-sign dimuon mean p_T versus mass distribution. Clear decrease in the dimuon mean p_T can be seen in the J/ψ mass region.*

Figure 6.5 shows a clear decrease in the mean p_T ($< p_T >$) at the J/ψ mass. Further investigation revealed that the decrease is concentrated from most peripheral (70%-90%) to semi-central events (30%-50%). No such decrease in the $< p_T >$ was observed in the central collisions.

6.3 Data sample

The Pb-Pb data, used in the present analysis, were recorded at $\sqrt{s_{NN}}$ = 5.02 TeV in November, 2015. The corresponding integrated luminosity was $\mathscr{L}_{int}^{Pb-Pb} = 225\ \mu b^{-1}$. The observed hadronic interaction rate was about 25 Hz out of the total interaction rate around 300 Hz, remaining were background from electromagnetically induced processes. Possibility of pileup events, i.e. the chance of two simultaneous hadronic interactions, was negligible.

The data belongs to LHC15o period and all runs passing Quality Assurance (QA) [66] are located in muon_calo_pass1. However, among 154 quality assured runs only 137 runs qualify as good runs and passes physics selection criteria. All the runs used in the present analysis are listed in Appendix A. The AODs analysed are AliAOD.Muons.root from AOD175 production. In the present analysis only dimuon unlike sign (MUL)

triggered events are considered, which requires at least one pair of opposite sign muon tracks in the muon spectrometer triggering system in coincidence with minimum bias trigger (MB), each having p_T above low-p_T threshold set by online trigger algorithm. The low-p_T trigger threshold was fixed at 1 GeV/c.

6.3.1 Event and track selections

Event selection

Events are selected by selecting the trigger and by applying the physics selection criteria. As mentioned in the previous section, for the purpose of this analysis opposite-sign (OS) dimuon trigger, namely CMUL7-B-NOPF-MUFAST, was selected. The physics selection criteria used was AliVEvent::kMuonUnlikeLowPt7. The number of triggered events before physics selection was 127171888 (for centrality 0-100%), whereas after physics selection it was found to be 126818829 (for centrality 0-100%). No additional cut is applied for the event selection. The V0M was used for the estimation of centrality.

Track selection

Due to large background in Pb-Pb collisions, it is a challenging task to preserve the purity of the muon sample. In order to achieve this tight selection criteria are imposed on the single muon tracks. It also make sure that all the reconstructed OS muon tracks correspond to the decay of charmonium family.

The selection criteria for single muon tracks include:

- Tracks must lie within the pseudorapidity range -4.0 < η_μ < -2.5. This condition corresponds to the acceptance of the muon spectrometer.

- Only those muon tracks are considered that should match Low-p_T trigger threshold (p_T > 1 GeV/c) in order to be consistent with the MUL trigger condition. This condition is fulfilled when each reconstructed track in the muon chambers must have a matching track in the muon trigger.

- Each muon track must have its transverse radius coordinate in the range 17.6 cm < R_{Abs} < 89.5 cm at the end of the front absorber. In terms of the polar angle of

the track, this cut may also be expressed as $2° < \theta_{Abs} < 10°$, where θ_{Abs}[9] is the polar angle of the track at the end of the absorber. R_{Abs} and z_{Abs}^{end} is the radius of the track and z-coordinate at the end of the absorber respectively ($z_{Abs}^{end} = 505cm$).

- p×DCA cut, i.e. the product of the track momentum and the distance between the vertex and the track extrapolated to the vertex transverse plane. This cut further reduces the residual background contamination.

The selection requirements at the dimuon level are:

- The rapidity cut $2.5 < y < 4.0$ is applied on the dimuon pair.
- Charge μ_1 + Charge $\mu_2 = 0$. Because we are studying J/ψ through the dimuon decay channel, i.e. $J/\psi \rightarrow \mu^+\mu^-$, it requires that the net charge of both the muons should be zero.

6.4 Signal extraction in Pb-Pb collisions at $\sqrt{s_{NN}} = 5.02$ TeV

The J/ψ candidates are formed by pairing opposite-sign muon tracks. The number of opposite-sign dimuon pairs as a function of their invariant mass, i.e. invariant mass distribution, is shown in Figure 6.6. The signal extraction was performed by fitting this invariant mass distribution. The range of the $x-$axis is chosen in the mass region of the J/ψ and ψ(2S). A clear peak can be seen in the distribution around 3.1 GeV/c^2 which corresponds to the muon pair coming from the decay of J/ψ. To extract the number of produced J/ψ ($N_{J/\psi}$) the invariant mass distribution is fitted with a sum of two functions, one describing the signal shape and the other for the background. Two functions are used for fitting the J/ψ signal, namely Extended (Double) Crystal Ball (CB2) function and NA60 function. On the other hand, Variable Width Gaussian (VWG) function is used for fitting the background. The details of the aforementioned functions are given in Appendix B.

The number of produced J/ψ can be extracted in two ways: the first one is direct fit to unlike-sign dimuons invariant mass distribution and the second method utilizes the event mixing technique for the subtraction of combinatorial ground. Nevertheless, only the first method is used for the signal extraction in this thesis.

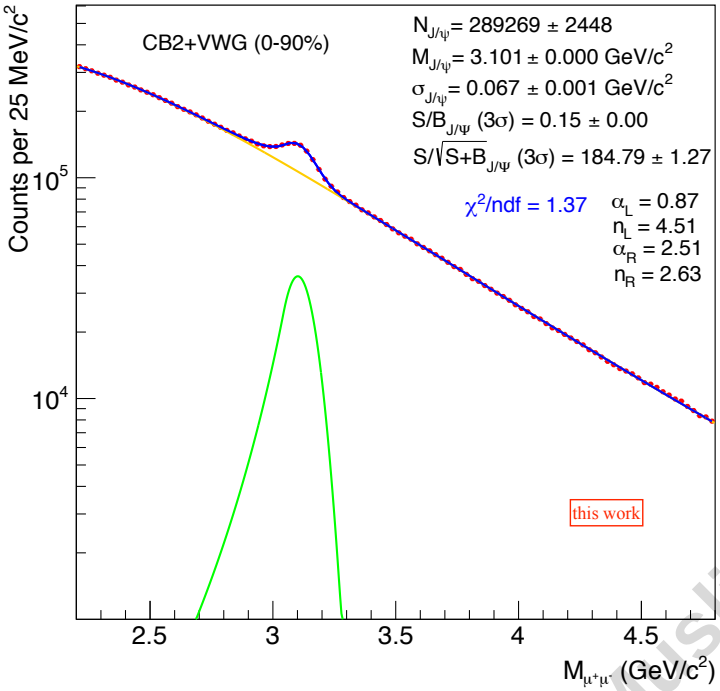

Figure 6.6: *Invariant mass distribution of opposite-sign (OS) dimuons for* $0 \leq p_T < 8$ *(GeV/c),* $2.5 < y < 4.0$ *and centrality 0-90%. Green, yellow and blue line corresponds to signal function, background functions and total function (signal+background) respectively. Extended Crystal Ball (CB2) function is used for fitting the signal, whereas Variable Width Gaussian (VWG) function is used for fitting the background.*

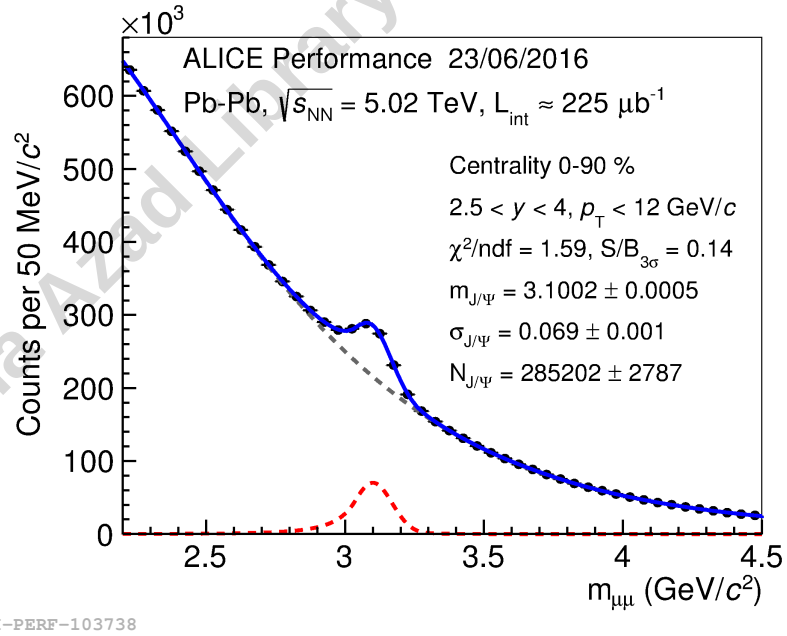

Figure 6.7: *ALICE Performance figure for the invariant mass spectrum of OS dimuons (zoomed in the J/ψ mass region). Figure taken from [109].*

Since lowest-p_T bins have limited statistics binned log likelihood method is used in the fitting procedure. The likelihood method treat the empty bins correctly by assuming asymmetric Poissonian errors in low statistics bin. The integrated invariant mass distribution of opposite-sign (OS) dimuons is shown in Figure 6.6. Just for the sake of comparison, the officially accepted ALICE performance Figure 6.7 is incorporated here. The number of J/ψ's, after direct fitting the signal and background, are found to be compatible and lies within the statistical error. However, the difference may be ascribed to, partially, different fitting ranges employed in extracting the signal.

6.4.1 Signal extraction in p_T bins

The J/ψ signal was extracted in 4 p_T bins (same as Run 1), namely $0 \leq p_T < 0.3$ GeV/c, $0.3 \leq p_T < 1.0$ GeV/c, $1.0 \leq p_T < 8.0$ GeV/c and $0 \leq p_T < 8.0$ GeV/c, shown in Figure 6.8. The last p_T bin is considered for cross-checks. Table 6.2 summarizes the number of J/ψs found from the direct fitting method at two collision energies, i.e. $\sqrt{s_{NN}}$ = 5.02 TeV and $\sqrt{s_{NN}}$ = 2.76 TeV.

p_T bins (GeV/c)	$N_{J/\psi}$ ($PbPb$@2.76 TeV)	$N_{J/\psi}$ ($PbPb$@5.02 TeV)
0 – 0.3	1107 ± 231	9308 ± 516
0.3 – 1.0	8129 ± 640	56192 ± 1343
1.0 – 8.0	31244 ± 981	223831 ± 3063

Table 6.2: *Comparison of number of J/ψs obtained from the direct fitting method at two different collision energies. The values quoted for PbPb@2.76 TeV are derived from the analysis note [35].*

The tail parameters are extracted by fitting the signal function to the MC simulated data. The embedding simulation technique was used in the generation was MC data. The embedding technique is explained in Section 6.5.1. Tail parameters were not extracted for different bins. Hence, the single tail parameter is used for fitting all the p_T bins. While performing the fittings, in all the p_T and centrality bins, the J/ψ mass (M) and the width (σ) was kept free, although both of them do not exhibit any dependence on p_T and centrality.

[9] $\theta_{Abs} = arctan\frac{R_{Abs}}{z^{end}_{Abs}}$

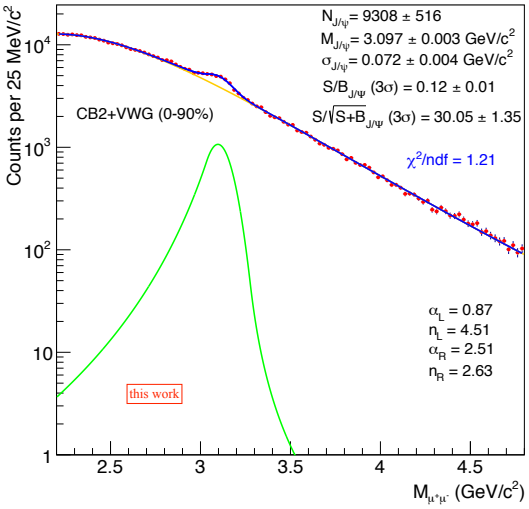

(a) $0 \leq p_T < 0.3$ *(GeV/c)*

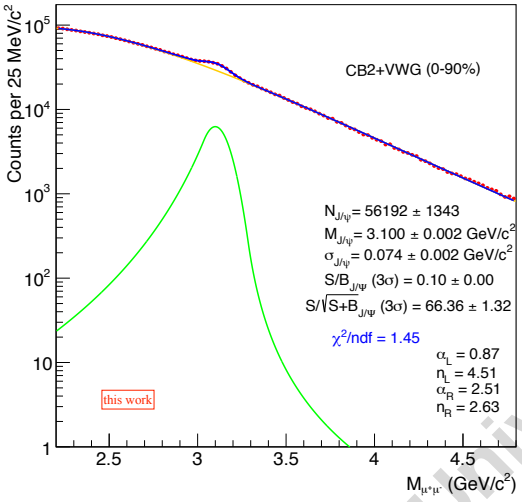

(b) $0.3 \leq p_T < 1$ *(GeV/c)*

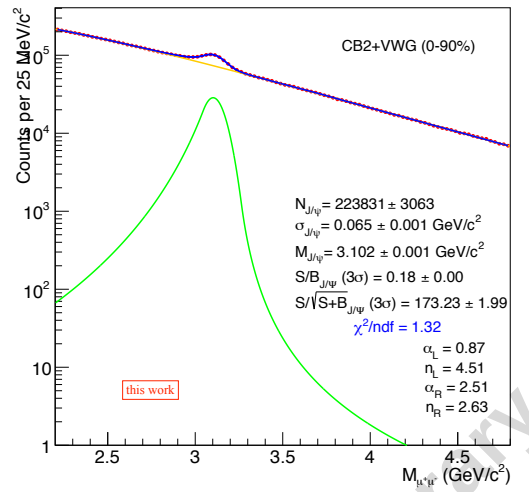

(c) $1 \leq p_T < 8$ *(GeV/c)*

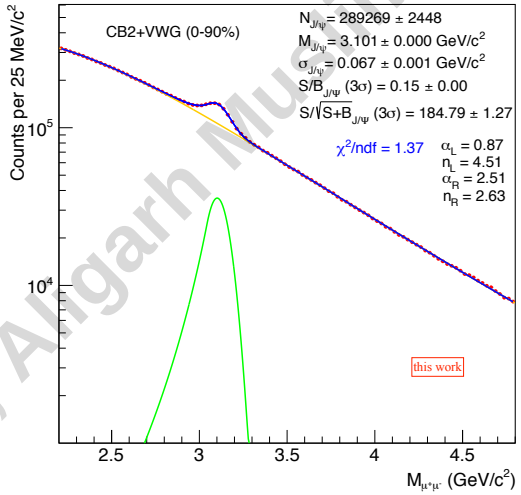

(d) $0 \leq p_T < 8$ *(GeV/c)*

Figure 6.8: *OS dimuons invariant mass spectra in 4 p_T bins, i.e. $0 \leq p_T < 0.3$ (top left), $0.3 \leq p_T < 1$ (top right), $1 \leq p_T < 8$ (bottom left) and $0 \leq p_T < 8$ (bottom right) (GeV/c). The extended crystal ball function (CB2) and Variable Width Gaussian (VWG) function are used for fitting the signal and background respectively.*

The J/ψ mass extracted from the direct fit is found to be systematically higher than its PDG value (3.097 GeV) [151] in general, however, the maximum difference never exceeds 0.5%. The signal over background ratio, S/B, and the significance ($S/\sqrt{S+B}$) are measured within the three standard deviations about the J/ψ mass value. Significance shows clear dependence upon the value of p_T interval. S/B also does not show significant variation with p_T. The number of J/ψs extracted in different p_T bins are found to be consistent with the number extracted from the integrated invariant mass spectrum.

6.4.2 Signal extraction in centrality bins at very low-p_T

The focus of the work presented in this thesis is peripheral collisions in the very low-p_T region. Thus, the signal extraction was performed in different centrality classes at the very low-p_T. In the first analysis measurement of photoproduction cross section was done for three peripheral centrality classes, i.e. 30%-50%, 50%-70% and 70%-90%. In order to compare the results the very low-p_T region, 0-0.3 GeV/c, was divided into the same aforementioned centrality intervals. The signal extraction was performed in each centrality bin. The p_T region 0-0.3 GeV/c was further divided into three equal p_T bins of 100 MeV/c and each p_T bin was studied in the above said three centrality intervals.

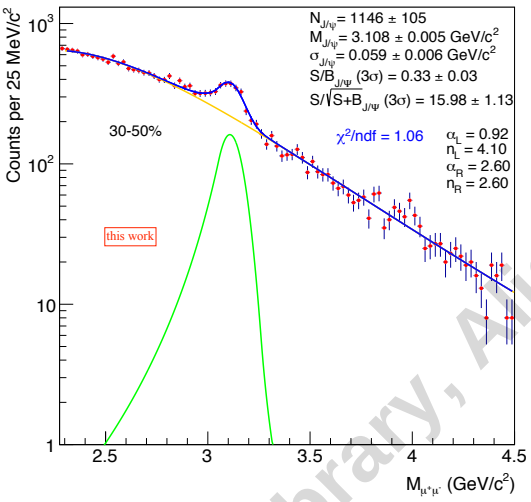

(a) $0 \leq p_T < 0.3$ *(GeV/c)*

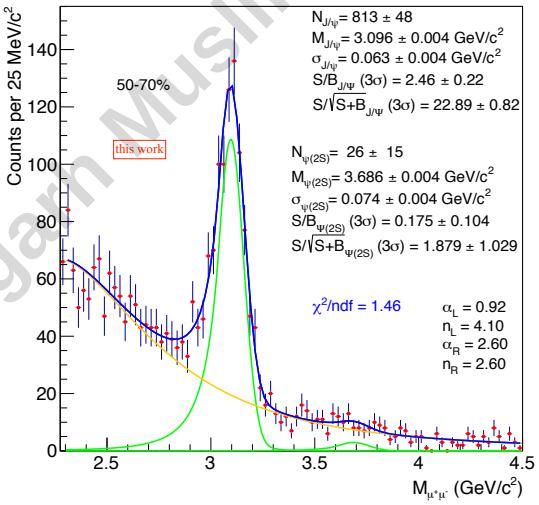

(b) $0 \leq p_T < 0.3$ *(GeV/c)*

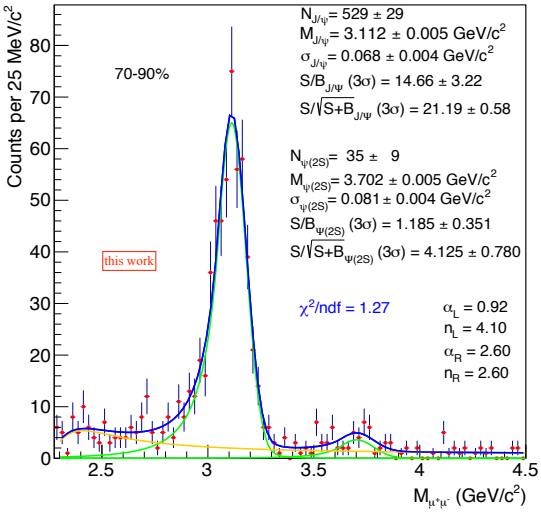

(c) $0 \leq p_T < 0.3$ *(GeV/c)*

Figure 6.9: *OS dimuon invariant mass spectra fit, in* $0 \leq p_T < 0.3$ *(GeV/c), for three centrality intervals, 30%-50% (top left), 50%-70% (top right) and 70%-90% (bottom).*

Centrality class (%)	$N_{J/\psi}$ (0-0.3 GeV/c) ($PbPb$@2.76 TeV)	$N_{J/\psi}$ (0-0.3 GeV/c) ($PbPb$@5.02 TeV)
30-50	126 ± 4	1146 ± 105
50-70	39 ± 2	813 ± 48
70-90	8 ± 1	529 ± 29

Table 6.3: *Comparison of number of J/ψs obtained by direct fit method at two different collision energies. The interval $0 \leq p_T < 0.3$ (GeV/c) was divided into three centrality classes, i.e. 30%-50%, 50%-70% and 70%-90%. The values quoted for PbPb@2.76 TeV are taken from the analysis note [35].*

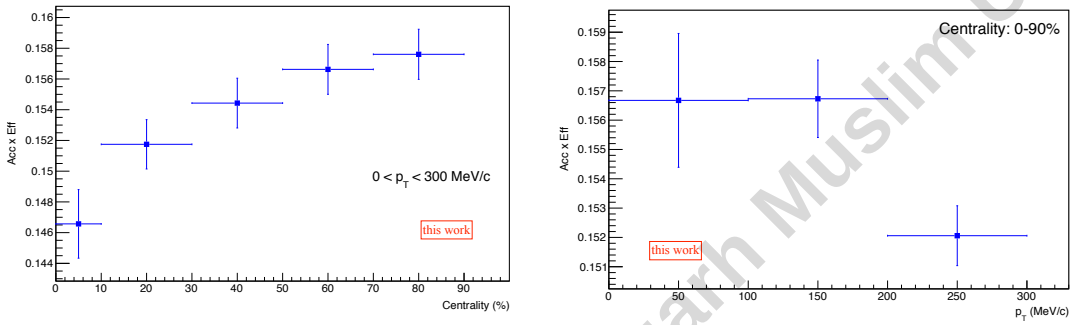

(a) *Dependence of $A \times \epsilon$ on centrality.* **(b)** *Variation of $A \times \epsilon$ on p_T.*

Figure 6.10: *Acceptance times Efficiency as a function of centrality (left) and p_T (right) for $0 \leq p_T < 0.3$ GeV/c.*

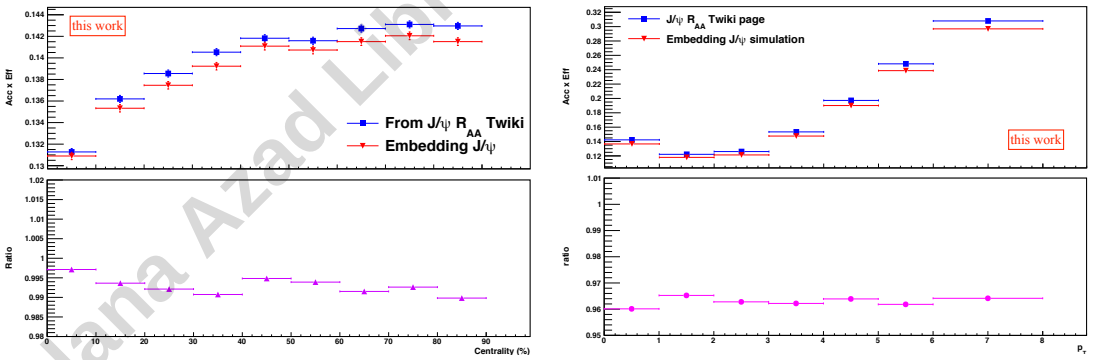

(a) **(b)**

Figure 6.11: *$A \times \epsilon$ comparison for CINT7 and CMUL7 events as a function of collision centrality (left) and p_T (right). Magenta corresponds to CINT7 and blue corresponds to CMUL7.*

Dependence of signal over background, S/B, can be clearly seen from the Figure 6.9. It increases from central to peripheral events. The $\psi(2S)$ signal could be extracted, shown in Figure 6.9b and Figure 6.9c, due to less background in peripheral events. However, its S/B and significance is insignificant.

The number of J/ψs found by direct fit is compared, Table 6.3, in three centrality classes in $0 \leq p_T < 0.3$ GeV/c. In addition, Figure 6.12 shows the dimuon invariant mass spectra for $0 \leq p_T < 0.1$, $0.1 \leq p_T < 0.2$, and $0.2 \leq p_T < 0.3$ GeV/c in centrality classes 30%-50%, 50%-70% and 70%-90%.

6.5 Acceptance×Efficiency ($A \times \epsilon$)

The measurement of $A \times \epsilon$ correction factor for coherently photoproduced J/ψ was obtained from the MC embedding simulations. The integrated $A \times \epsilon$ for a given run is obtained from the following expression:

$$A \times \epsilon = \frac{N^{rec}_{J/\psi}(2.5 < y < 4)}{N^{gen}_{J/\psi}(2.5 < y < 4)} \tag{6.3}$$

The corresponding statistical uncertainty is given by the following formula:

$$\sigma_{A\times\epsilon} = Max\left(\frac{1}{N^{gen}_{J/\psi}}, \sqrt{\frac{A \times \epsilon \cdot (1 - A \times \epsilon)}{N^{gen}_{J/\psi}}}\right) \tag{6.4}$$

where $N^{gen}_{J/\psi}$ and $N^{rec}_{J/\psi}$ represents the number of generated J/ψs and the number of reconstructed J/ψs respectively.

6.5.1 Embedding simulations

In the embedding MC technique a signal particle (a J/ψ in this analysis) is simulated and the detector response is embedded into a real event raw data (before the reconstruction). Both the signal and detector response is superimposed. Then the embedded event is reconstructed in the same manner as a normal real event. The advantage of embedding technique is that it provides the most realistic background conditions. The embedding simulations are particularly suitable for Pb-Pb collisions. Because of very high multiplicity produced in central Pb-Pb collisions the environment can alter the track reconstruction efficiency, which necessitates the realistic description of the background, which is not taken into account in pure J/ψ simulations. The primary objective of embedding simulations is to compute the $A \times \epsilon$ factor in different bins of p_T, y and centrality.

While performing the analysis embedding data is treated like real data. All the

selections applied on the real data are also applied on the embedding data. The two periods LHC16e2 and LHC162_plus is used in the present analysis [63]. The Figure 6.10a and Figure 6.10b show the dependence of $A \times \epsilon$ on centrality and p_T respectively. Since the embedding simulations are performed in MB events and the present analysis uses unlike-sign dimuon triggers (CMUL trigger), a weight has to be applied to consider the fact that runs with a large numbers of MB events may have small number of MUL events. In this way run-by-run fluctuations will be properly taken into account and the final result integrated over a full period will not be biased. Nonetheless, no weight is applied in Figure 6.10. It can be seen from the Figure 6.10a that as we move from central to peripheral collisions $A \times \epsilon$ systematically increases. On the other hand, there is a clear decrease in the value of $A \times \epsilon$ in the last p_T bin.

Figure 6.11a and Figure 6.11b shows the effect of CINT7 trigger on the real data as a function of centrality and p_T respectively. The real data is recorded with CMUL7 trigger. From Figure 6.11, it may be clearly inferred that using CINT7 trigger on the real data will systematically lower $A \times \epsilon$ values. The difference widens at high-p_T. For the determination of tail parameters in different p_T bins as well as systematics calculation, the pure signal was fitted with two functions, CB2 and NA60. The signal was generated using three MC methods, namely embedding, STARLIGHT and GEANT4.

6.5.2 Starlight simulations

The STARLIGHT event generator is most suitable for the simulation of ultra-peripheral collisions in relativistic heavy-ion collisions and was used to determine the $A \times \epsilon$ correction factor in the first very low-p_T analysis. It simulates both photonuclear and $\gamma\gamma$ interactions. Central simulations were performed for three processes, coherent J/ψ, incoherent J/ψ and coherent ψ(2S) to J/ψ. Nearly ten million events were generated for each individual process. It was a pure J/ψ simulation and per event one J/ψ was generated. Number of J/ψ generated per run was proportional to the number of CMUL7 events per run in data. Few control plots are shown in Figure 6.17. It can be seen from Figure 6.17a that generated dimuons have mean $p_T \approx 55$ MeV/c in the $0 < p_T < 0.3$ GeV/c, whereas Figure 6.17d shows strong correlation between p_T and mass at very low-p_T, like in Run 1 simulations.

6.5.3 GEANT4 simulations

The tail parameters were also extracted by fitting the pure signal with extended crystal ball function (CB2) generated by the GEANT4 simulations in the $0 < p_T < 0.3$ GeV/c, see Figure 6.16. However, the GEANT4 simulations were performed by a member[10] of the ALICE Collaboration.

6.5.4 Low-p$_T$ J/ψ R_{AA}

The nuclear modification factor of inclusive J/ψ can be calculated, in each p$_T$ bin and centrality class, by the following formula:

$$R_{AA} = \frac{Y^{Pb-Pb}_{J/\psi}}{< T_{AA} > \times \sigma^{pp}_{J/\psi}} \tag{6.5}$$

where $Y^{Pb-Pb}_{J/\psi}$ is the corrected J/ψ yield given by Equation (6.6), $< T_{AA} >$ is the nuclear overlap function and $\sigma^{pp}_{J/\psi}$ is the J/ψ cross section in pp collisions.

In each p$_T$ bin, the corrected J/ψ yield in the centrality class i is given by:

$$Y^{i}_{N_{J/\psi}} = \frac{N^{i}_{J/\psi}}{BR_{J/\psi \to \mu^+\mu^-} N^{i}_{MB} (A \times \epsilon)^{i}} \tag{6.6}$$

where $N^{i}_{J/\psi}$ is the measured number of J/ψ in the i^{th} centrality class, $BR_{J/\psi \to \mu^+\mu^-}$ is the J/ψ branching ratio in the dimuon decay channel, $A \times \epsilon^{i}$ is the acceptance times efficiency of the detector in the i^{th} centrality class and N^{i}_{MB} is the number of minimum bias events in the i^{th} centrality class.

[10] Mohamad Tarhini, IPN Orsay.

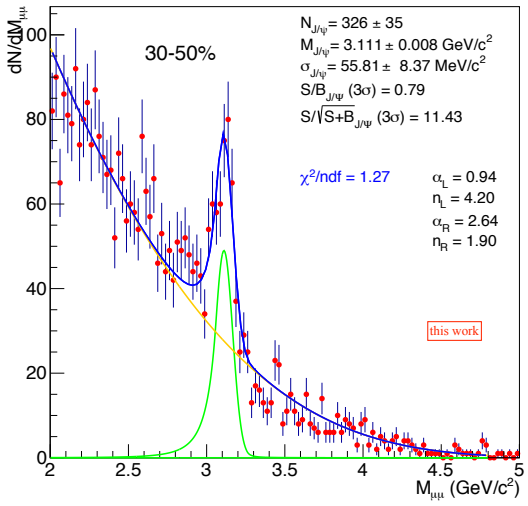

(a) $0 \leq p_T < 0.1$ *(GeV/c)*

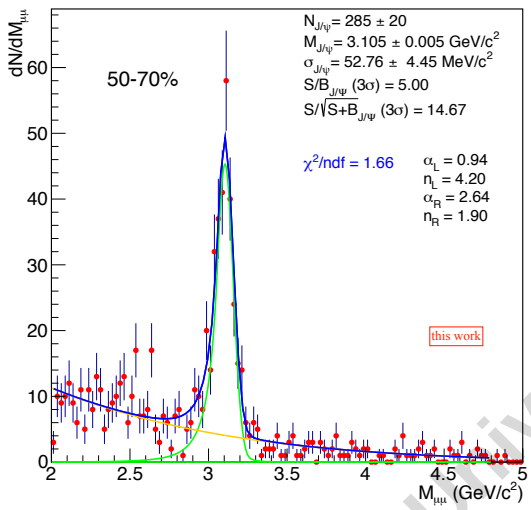

(b) $0 \leq p_T < 0.1$ *(GeV/c)*

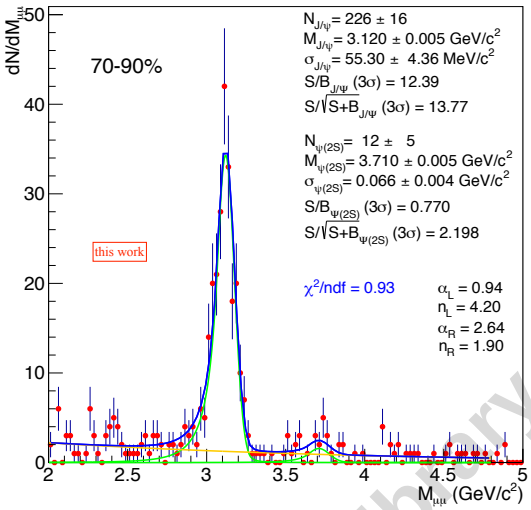

(c) $0 \leq p_T < 0.1$ *(GeV/c)*

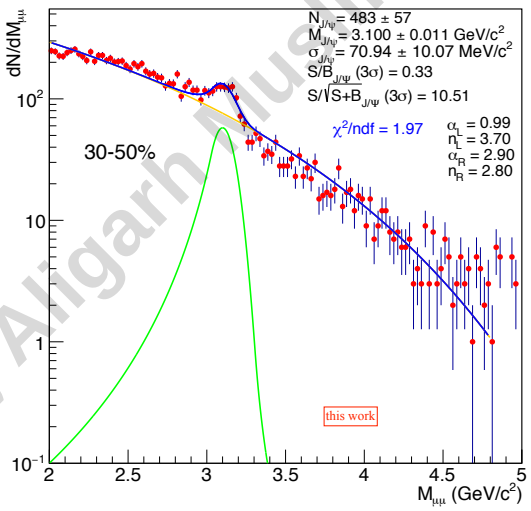

(d) $0.1 \leq p_T < 0.2$ *(GeV/c)*

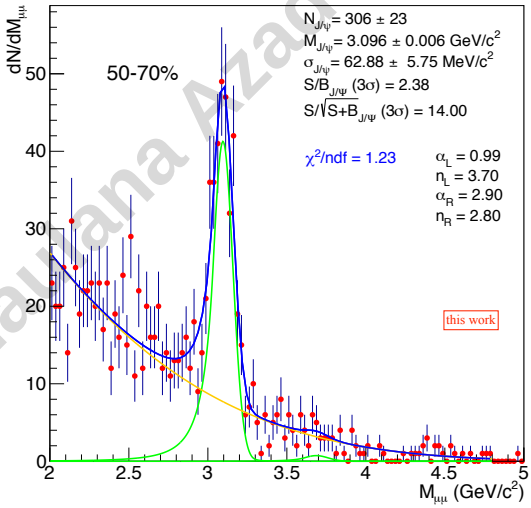

(e) $0.1 \leq p_T < 0.2$ *(GeV/c)*

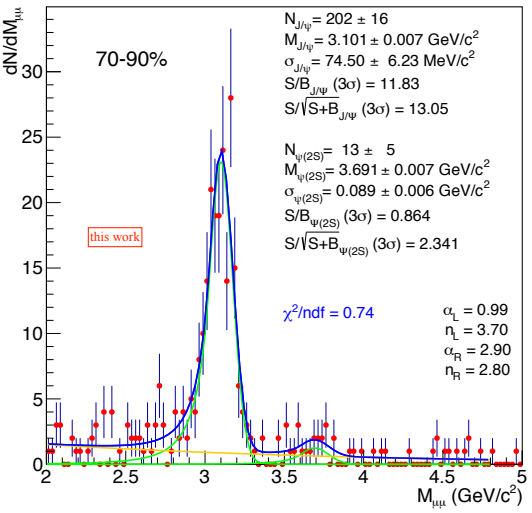

(f) $0.1 \leq p_T < 0.2$ *(GeV/c)*

Figure 6.12: *Dimuon invariant mass spectra fit, in* $0 \leq p_T < 0.1$ *and* $0.1 \leq p_T < 0.2$ *(GeV/c), for 30%-50%, 50%-70% and 70%-90% centrality bins.*

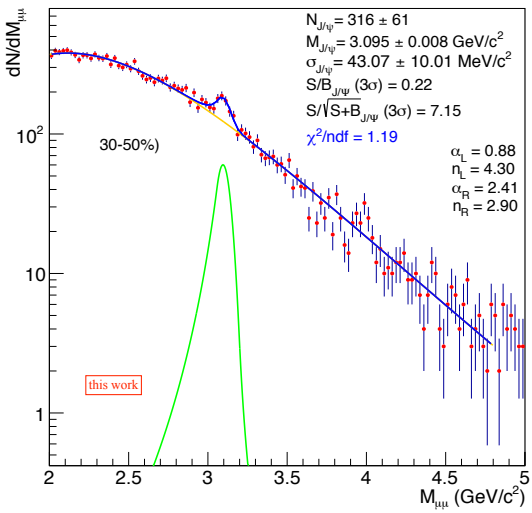

(g) $0.2 \leq p_T < 0.3$ *(GeV/c)*

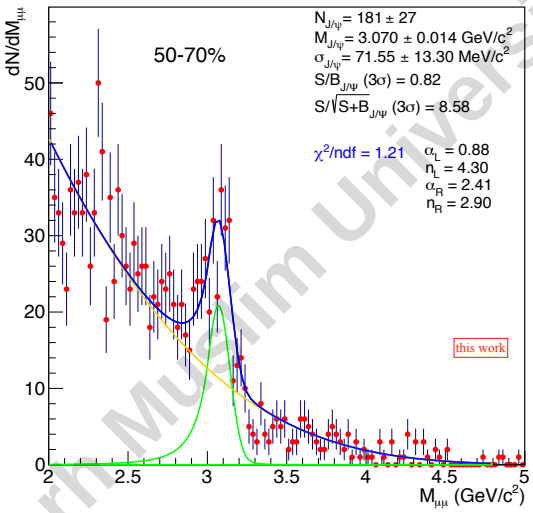

(h) $0.2 \leq p_T < 0.3$ *(GeV/c)*

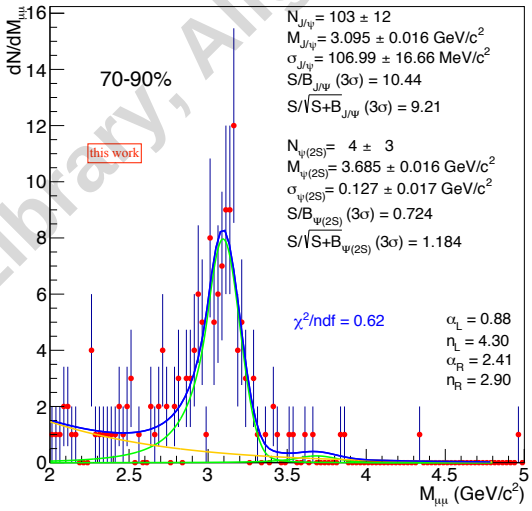

(i) $0.2 \leq p_T < 0.3$ *(GeV/c)*

Figure 6.12: *Dimuon invariant mass spectra fit, in* $0.2 \leq p_T < 0.3$ *(GeV/c), for 30%-50%, 50%-70% and 70%-90% centrality classes.*

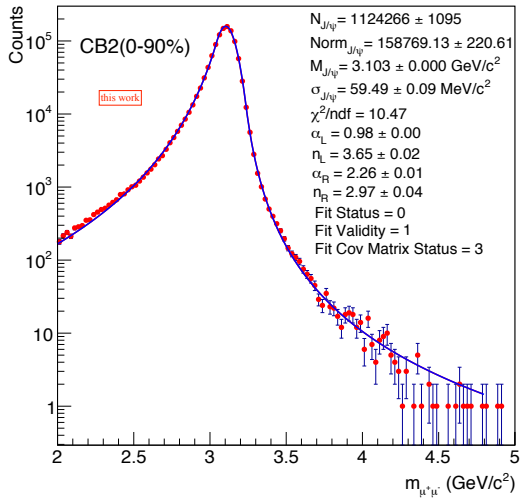

(a) $1 \leq p_T < 8$ *(GeV/c)*

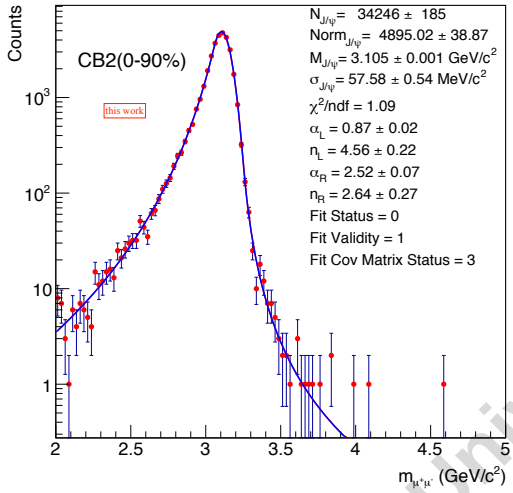

(b) $0 \leq p_T < 0.3$ *(GeV/c)*

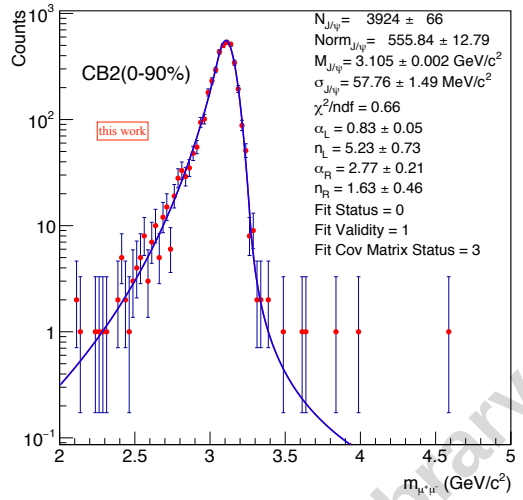

(c) $0 \leq p_T < 0.1$ *(GeV/c)*

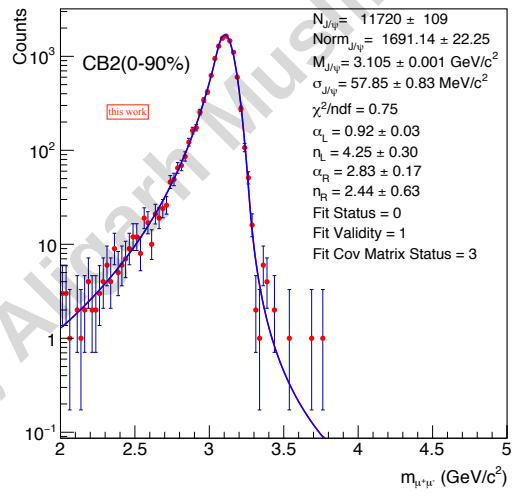

(d) $0.1 \leq p_T < 0.2$ *(GeV/c)*

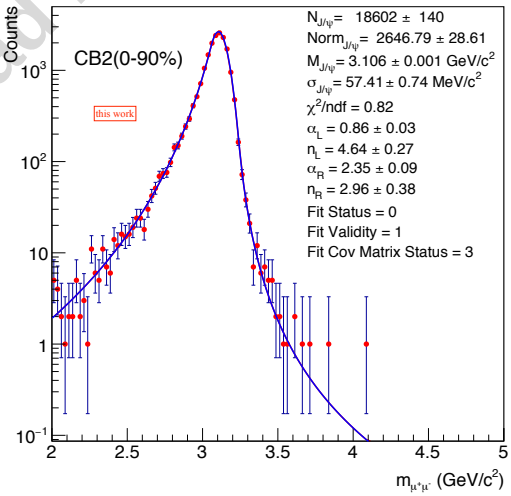

(e) $0.2 \leq p_T < 0.3$ *(GeV/c)*

Figure 6.13: *Pure J/ψ signal from embedding simulations fitted with CB2 function in different p_T ranges. Fit range:[2, 4.8].*

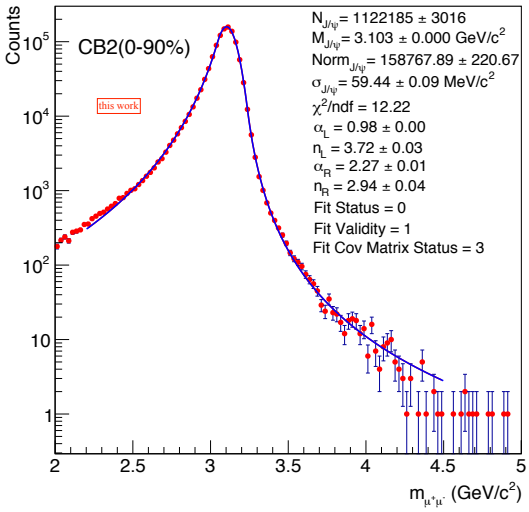

(a) $1 \leq p_T < 8$ *(GeV/c)*

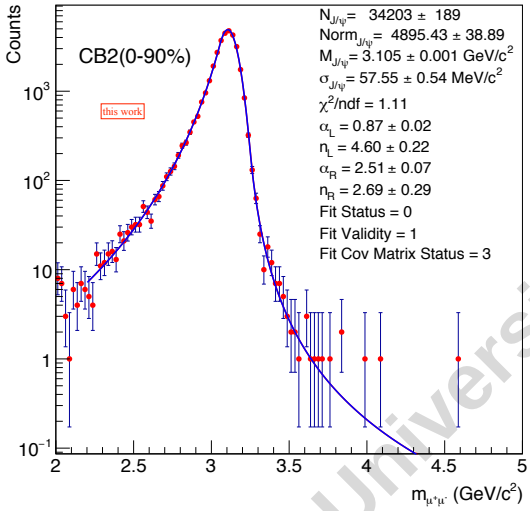

(b) $0 \leq p_T < 0.3$ *(GeV/c)*

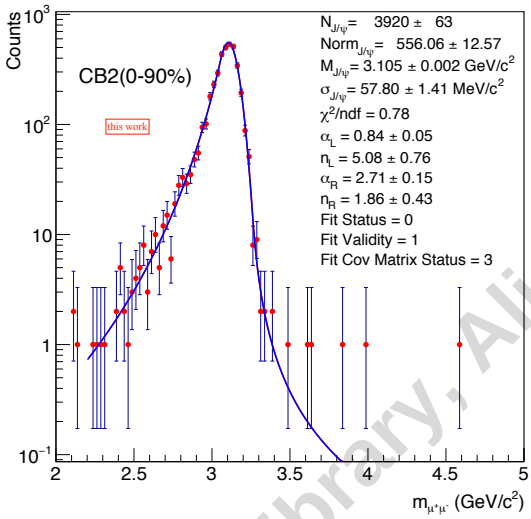

(c) $0 \leq p_T < 0.1$ *(GeV/c)*

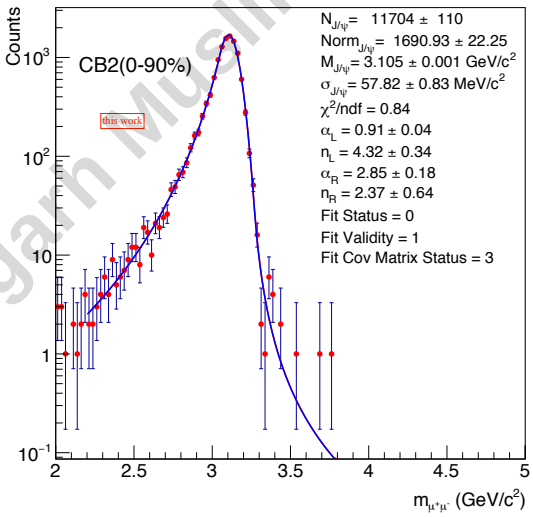

(d) $0.1 \leq p_T < 0.2$ *(GeV/c)*

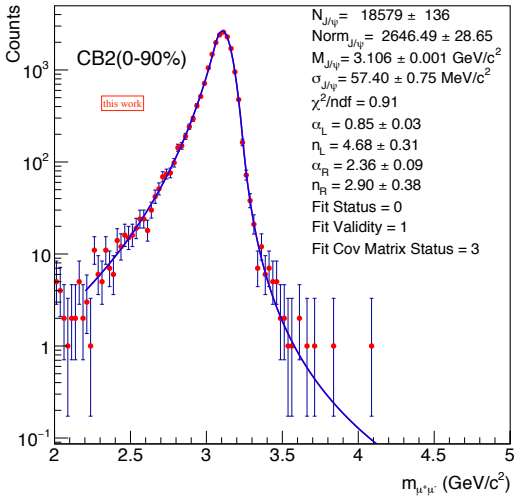

(e) $0.2 \leq p_T < 0.3$ *(GeV/c)*

Figure 6.14: *Pure J/ψ signal from embedding simulations fitted with CB2 function in different p_T ranges. Fit range:[2.2, 4.5].*

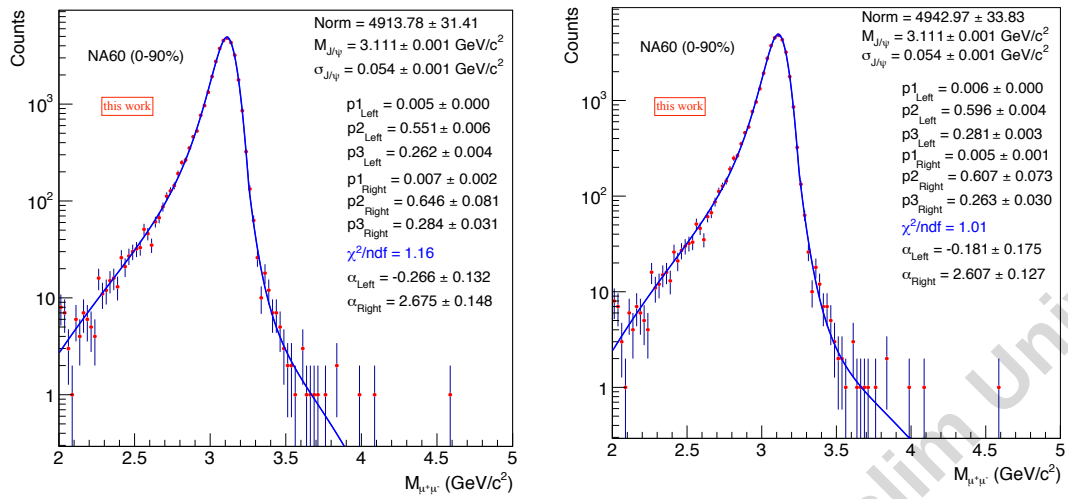

(a) $0 \leq p_T < 0.3$ *(GeV/c)* **(b)** $0 \leq p_T < 0.3$ *(GeV/c)*

Figure 6.15: *Pure J/ψ signal from embedding simulations fitted with NA60 function in* $0 \leq p_T < 0.3$ *GeV/c for two fit ranges: [2, 4.5] & [2, 4.8].*

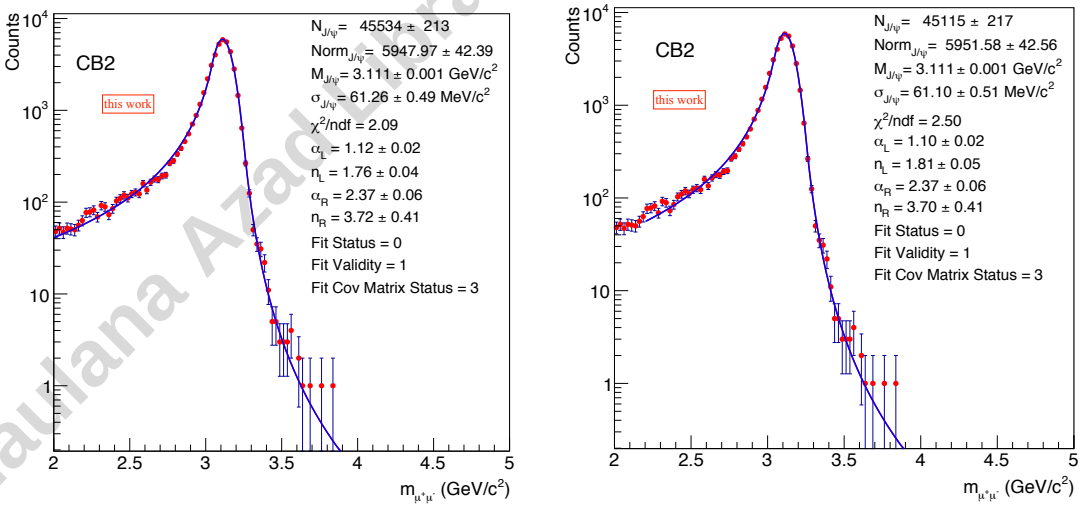

(a) $0 \leq p_T < 0.3$ *(GeV/c)* **(b)** $0 \leq p_T < 0.3$ *(GeV/c)*

Figure 6.16: *Pure J/ψ signal from the Geant4 simulations fitted with CB2 function in two fit ranges [2, 4.8] & [2.2, 4.5].*

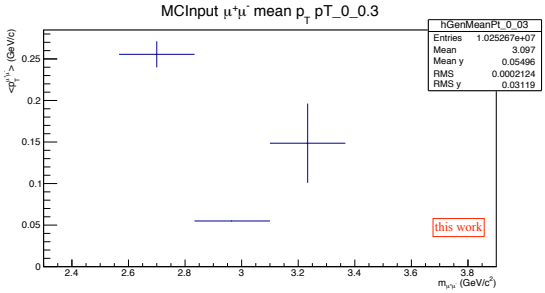

(a) *Generated $<p_T>$ versus mass.*

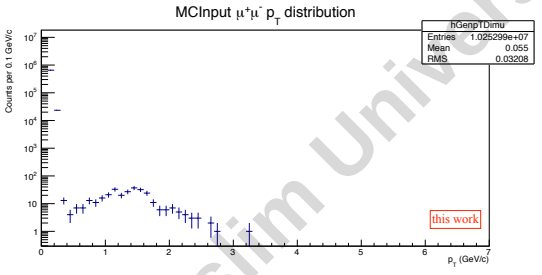

(b) *Generated p_T distribution.*

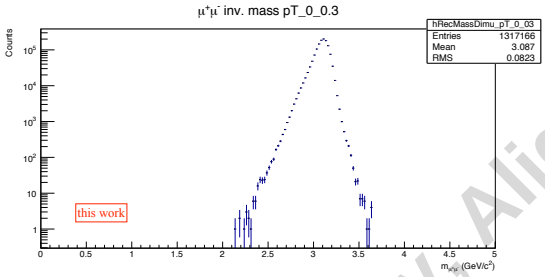

(c) *Reconstructed invariant mass distribution.*

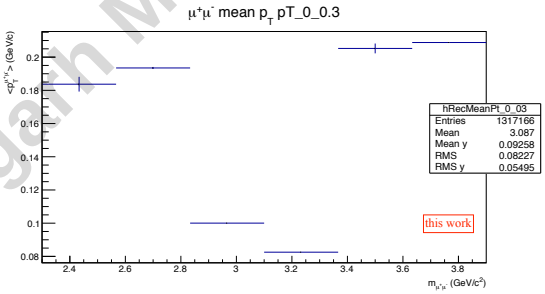

(d) *Reconstructed $<p_T>$ versus mass.*

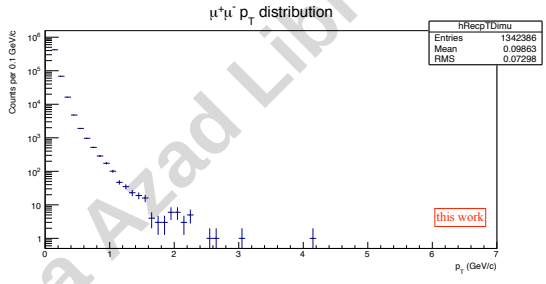

(e) *Reconstructed p_T distribution.*

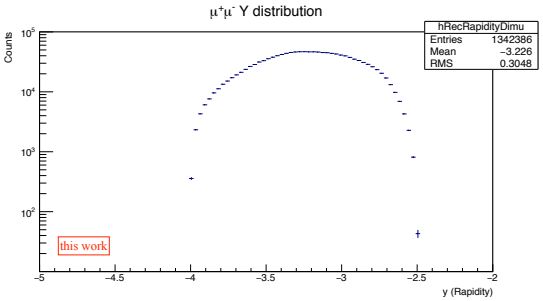

(f) *Generated rapidity distribution.*

Figure 6.17: *Some control plots from the starlight simulations.*

Part IV

Summary

7

Conclusions and outlook

This thesis presents a detailed study of unexpected chamber efficiency issues of the ALICE muon spectrometer and J/ψ production at very low transverse momentum ($p_T < 300 MeV/c$) in peripheral hadronic Pb-Pb collisions at $\sqrt{s_{NN}}$ = 5.02 TeV.

The unexpected chamber efficiency issues were identified by comparing "cluster maps" from the Monte Carlo (MC) simulation and the real data. The cluster maps studied correspond to pp data $\sqrt{s}$ = 13 TeV recorded during one year period time of the 2016. The study helped in improving the detector description in the simulations used to correct the real data taken by the ALICE muon spectrometer. The problematic regions of all the muon chambers, which could not be well reproduced in simulations through the status maps prepared by muonQA, were spotted by making detailed comparison of the cluster maps from the data and simulation. These regions are added in a "Reject list" and fresh simulations are performed using the updated information. This results in a more precise $A \times \epsilon$ correction which, in turn, reduce the associated tracking systematic uncertainties. These studies play an important role in all the quarkonium analyses in Pb-Pb collisions performed with the ALICE Muon Spectrometer.

The excess J/ψ production measurements are performed at p_T < 300 MeV/c in peripheral Pb-Pb collisions at $\sqrt{s_{NN}}$ = 5.02 TeV, with particular emphasis on signal extraction. The excess in J/ψ yield at p_T < 300 MeV/c is ascribed to coherent photoproduction of J/ψ and could not be explained with the existing theoretical models which are based on hadronic interactions only. The study of low-p_T J/ψ excess may be

used to constrain the various models based on suppression and regeneration mechanisms. Remarkable increase in J/ψ R_{AA} was found in $0 < p_T < 0.3$ GeV/c.

The number of J/ψs obtained from direct fit at $\sqrt{s_{NN}}$ = 2.76 TeV and $\sqrt{s_{NN}}$ = 5.02 TeV were compared in different p_T as well as centrality bins. In case of p_T bins comparison, 7-10 times increase, depending on the p_T bin, was found. However, remarkable difference was observed in comparing the centrality classes. It was found that moving from central to peripheral collisions the discrepancy widens with rapid pace, i.e. 9 times, 20 times and 66 times for 30%-50%, 50%-70% and 70%-90% respectively. The dependence of $A \times \epsilon$ on p_T and centrality classes at very low-p_T were also studied. It was observed that $A \times \epsilon$ increases from central to peripheral events. The effect of CINT7 trigger on real data systematically reduces $A \times \epsilon$. In addition, signal extraction was also performed for the pp collisions at $\sqrt{s}$ = 7 TeV in different centrality and rapidity bins.

The R_{AA} dependence on centrality is saturates above $N_{part} \sim 100$ at both the energies; i.e. $\sqrt{s_{NN}}$ = 2.76 TeV and $\sqrt{s_{NN}}$ = 5.02 TeV. It was also observed from the study of R_{AA} dependence on p_T that regeneration is dominates at low-p_T, whereas suppression is the dominant mechanism at high-p_T. The excess in the J/ψ yield at very low-p_T due to its coherent photoproduction is reflected in the significant enhancement of J/ψ R_{AA}. Comparing the ALICE results with the PHENIX it is clear that the regeneration, if any, at RHIC energies are insignificant.

The analysis of low-p_T excess J/ψ at $\sqrt{s_{NN}}$ = 5.02 TeV presented in this thesis may be complemented by the cross section and nuclear modification factor measurements in different centrality classes.

Part V

Appendices

A

List of run numbers used in this thesis

PbPb @ 5.02 TeV (LHC15o, 137 runs):

000246994 000246991 000246989 000246984 000246982 000246980 000246949
000246948 000246945 000246942 000246937 000246930 000246871 000246867
000246865 000246864 000246859 000246855 000246851 000246847 000246846
000246845 000246844 000246809 000246808 000246807 000246806 000246805
000246804 000246765 000246763 000246760 000246759 000246758 000246757
000246755 000246751 000246750 000246676 000246675 000246495 000246493
000246488 000246487 000246434 000246433 000246431 000246428 000246424
000246392 000246391 000246390 000246276 000246275 000246272 000246225
000246222 000246220 000246217 000246182 000246181 000246178 000246153
000246152 000246151 000246148 000246115 000246113 000246089 000246087
000246053 000246049 000246048 000246042 000246037 000246036 000246012
000246003 000246001 000245996 000245963 000245954 000245952 000245949
000245833 000245831 000245829 000245793 000245785 000245775 000245766
000245759 000245752 000245738 000245731 000245729 000245705 000245700
000245692 000245683 000245554 000245543 000245542 000245540 000245535
000245507 000245505 000245504 000245501 000245496 000245450 000245446
000245410 000245409 000245407 000245401 000245353 000245347 000245346
000245345 000245343 000245259 000245253 000245233 000245232 000245231
000245152 000245151 000245146 000245145 000245068 000245066 000245064
000244983 000244982 000244980 000244918

pp @ 7 TeV (LHC11c, 126 runs):

000155384 000155382 000155376 000155375 000155371 000155370 000155368
000155367 000155347 000155346 000155345 000155337 000155333 000155331
000155325 000155314 000155308 000155305 000155302 000155300 000155278
000155277 000155251 000155239 000155237 000155235 000155174 000155167
000155166 000155165 000155164 000155163 000155162 000155135 000154808
000154793 000154789 000154753 000154750 000154745 000154742 000154733
000154732 000154726 000154495 000154485 000154483 000154482 000154480
000154478 000154448 000154385 000154383 000154382 000154286 000154283
000154281 000154273 000154270 000154266 000154264 000154261 000154257
000154252 000154222 000154220 000154219 000154211 000154158 000154145
000154143 000154141 000154136 000154131 000154130 000154125 000154091
000154083 000154081 000154039 000153954 000153939 000153935 000153916
000153911 000153909 000153906 000153876 000153873 000153796 000153794
000153784 000153779 000153777 000153733 000153729 000153728 000153727
000153726 000153725 000153718 000153715 000153594 000153591 000153589
000153588 000153587 000153583 000153578 000153571 000153570 000153566
000153548 000153533 000153465 000153415 000153413 000153371 000153369
000153363 000153362 000153296 000153234 000153232 000153223 000153059

pp @ 7 TeV (LHC11d, 124 runs):

000159606 000159602 000159599 000159595 000159593 000159582 000159581
000159580 000159577 000159539 000159538 000159536 000159535 000159532
000159379 000159378 000159356 000159319 000159318 000159286 000159285
000159283 000159259 000159254 000159090 000158879 000158878 000158877
000158876 000158875 000158868 000158793 000158791 000158790 000158784
000158626 000158617 000158615 000158613 000158611 000158604 000158602
000158533 000158528 000158526 000158520 000158518 000158516 000158496
000158495 000158492 000158471 000158468 000158467 000158466 000158463
000158340 000158304 000158303 000158299 000158288 000158287 000158285
000158271 000158263 000158258 000158252 000158201 000158200 000158196
000158194 000158192 000158189 000158179 000158177 000158176 000158175
000158173 000158171 000158139 000158137 000158136 000158132 000158124
000158118 000158115 000158112 000158111 000158086 000158084 000157975
000157848 000157819 000157770 000157569 000157564 000157562 000157560
000157475 000157277 000157275 000157262 000157261 000157257 000157227
000157214 000157211 000157210 000157209 000157100 000157098 000157096
000157094 000157092 000157091 000157087 000157079 000157028 000157026
000157025 000156896 000156893 000156891 000156889

B
Fit functions

This appendix presents the description of the fitting functions used for extracting the signal of quarkonium resonances in general and in ALICE analyses in particular [91]. In this thesis, two functions, namely Extended Crystal Ball function (CB2) and NA60, are used for fitting the J/ψ signal as well as one function, namely Variable Width Gaussian (VWG) is used for the parametrization of background. The definition of the aforementioned functions, amongst others, are as follows:

B.1 Fitting functions used for J/ψ signal

B.1.1 Crystal Ball function

The Crystal Ball (CB) function is a probability distribution function, defined in equation B.1. It was introduced in [159]. The function consists of a Gaussian core portion, modeling the detector resolution, as well as a power-law "tail" on the left (low-mass) side defined by the parameters α and n for reproducing the non-Gaussian fluctuations accounting for energy loss processes.

$$f(x; N, \bar{x}, \sigma, \alpha, n) = N \cdot \begin{cases} exp\left(-\frac{(x-\bar{x})^2}{2\sigma^2}\right), & \text{if } \frac{x-\bar{x}}{\sigma} > -\alpha \\ A \cdot \left(B - \frac{x-\bar{x}}{\sigma}\right)^{-n}, & \text{if } \frac{x-\bar{x}}{\sigma} \leq -\alpha \end{cases} \tag{B.1}$$

where

$$A = \left(\frac{n}{|\alpha|}\right)^n \cdot exp\left(-\frac{|\alpha|^2}{2}\right)$$
$$B = \frac{n}{|\alpha|} - |\alpha|$$

B.1.2 Extended (or Double) Crystal Ball function

The extended Crystal Ball function (CB2) differs from Crystal Ball function in that it has power-law "tails" on both sides of the resonance peak. The right (high-mass) side tail not only incorporates the effects of multiple Coulomb scattering in the front absorber but also account for momentum resolution.

$$f(x; N, \bar{x}, \sigma, \alpha, n, \alpha', n') = N \cdot \begin{cases} exp\left(-\frac{(x-\bar{x})^2}{2\sigma^2}\right), & \text{if } \alpha' > \frac{x-\bar{x}}{\sigma} > -\alpha \\ A \cdot \left(B - \frac{x-\bar{x}}{\sigma}\right)^{-n}, & \text{if } \frac{x-\bar{x}}{\sigma} \leq -\alpha \\ C \cdot \left(D + \frac{x-\bar{x}}{\sigma}\right)^{-n'}, & \text{if } \frac{x-\bar{x}}{\sigma} \geq -\alpha' \end{cases} \tag{B.2}$$

where

$$A = \left(\frac{n}{|\alpha|}\right)^n \cdot exp\left(-\frac{|\alpha|^2}{2}\right)$$
$$B = \frac{n}{|\alpha|} - |\alpha|$$
$$C = \left(\frac{n'}{|\alpha'|}\right)^{n'} \cdot exp\left(-\frac{|\alpha'|^2}{2}\right)$$
$$D = \frac{n'}{|\alpha'|} - |\alpha'|$$

The x represents the dimuon invariant mass in both the CB and CB2 function. The parameters A, B, C and D are so defined that both the function as well as its first derivative are continuous.

B.1.3 NA60 function

The NA60 function was introduced by the NA60 Collaboration for the extraction of charmonium signal [193]. It is comprised of a normalization factor N, two Gaussian core parameters ($\bar{x}$ and σ) and eight tail parameters ($\alpha^L, p_1^L, p_2^L, p_3^L, \alpha^R, p_1^R, p_2^R$ and p_3^R). It is defined as

$$f(x; N, \bar{x}, \sigma, \alpha^L, p_1^L, p_2^L, p_3^L, \alpha^R, p_1^R, p_2^R, p_3^R) = N \cdot exp\left(-0.5\left(\frac{t}{t_0}\right)^2\right) \tag{B.3}$$

where

$$t = \frac{x - \bar{x}}{\sigma}$$

and

$$\begin{cases} t_0 = 1 + p_1^L(\alpha^L - t)^{\left(p_2^L - p_3^L\sqrt{(\alpha^L - t)}\right)}, & \text{if } t < \alpha^L \\ t_0 = 1, & \text{if } \alpha^L < t < \alpha^R \\ t_0 = 1 + p_1^R(t - \alpha^R)^{\left(p_2^R - p_3^R\sqrt{(t - \alpha^R)}\right)}, & \text{if } t > \alpha^R \end{cases}$$

B.2 Background fitting functions

B.2.1 Variable Width Gaussian (VWG)

The VWG function has a normalization factor N and three parameters $(\bar{x}, \alpha, \beta)$ and is defined as

$$f(x; N, \bar{x}, \alpha, \beta) = N \cdot exp\left(-\frac{(x - \bar{x})^2}{2\sigma_{VWG}^2}\right) \tag{B.4}$$

where

$$\sigma_{VWG} = \alpha + \beta\left(\frac{x - \bar{x}}{\bar{x}}\right)$$

B.2.2 Variable Width Gaussian (VWG2)

The VWG2 function differs from VWG in that it is a function of four parameters $(\bar{x}, \alpha, \beta, \gamma)$ instead of three and is defined as

$$f(x; N, \bar{x}, \alpha, \beta, \gamma) = N \cdot exp\left(-\frac{(x - \bar{x})^2}{2\sigma_{VWG}^2}\right) \tag{B.5}$$

where

$$\sigma_{VWG} = \alpha + \beta\left(\frac{x - \bar{x}}{\bar{x}}\right) + \gamma\left(\frac{x - \bar{x}}{\bar{x}}\right)^2$$

B.2.3 Polynomial2/Polynomial3 (pol2/pol3)

The function is defined in the following equation:

$$f(x) = N \cdot \left(\frac{Ax^2 + Bx + 1}{Cx^3 + Dx^2 + Ex + 1} \right) \tag{B.6}$$

C

Signal extraction in different p_T and y bins in pp collisions at $\sqrt{s}$ = 7 TeV

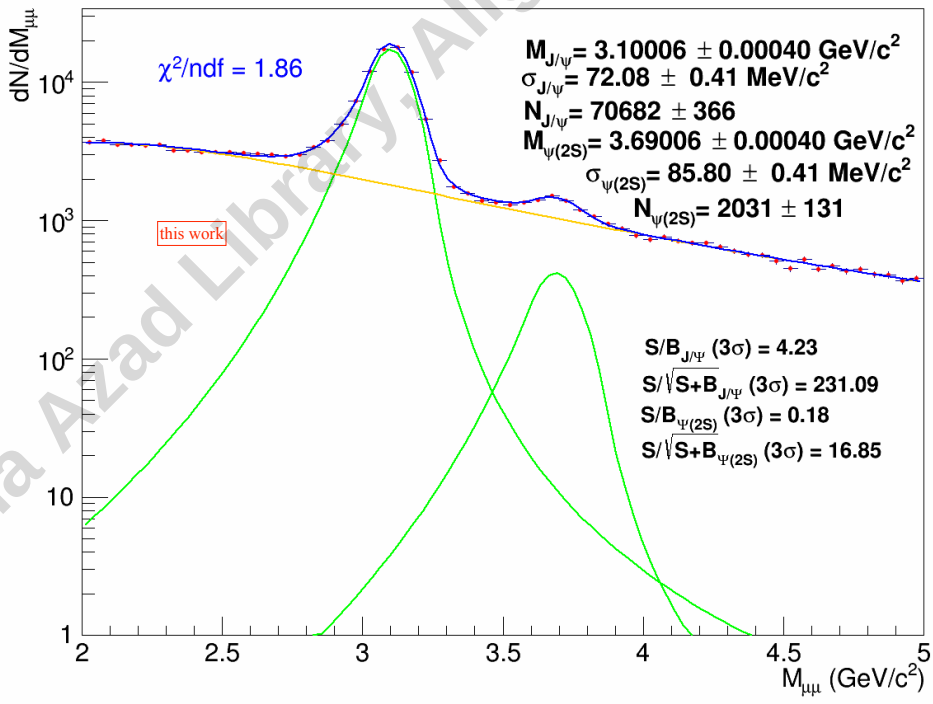

Figure C.1: *Integrated mass spectrum for* $0 < p_T < 20$ *(GeV/c). Extended Crystal Ball (CB2) and Variable Width Gaussian (VWG) functions are used for fitting the signal and background respectively. [LHC11c & LHC11d]*

C.1 Signal extraction in twelve p_T bins

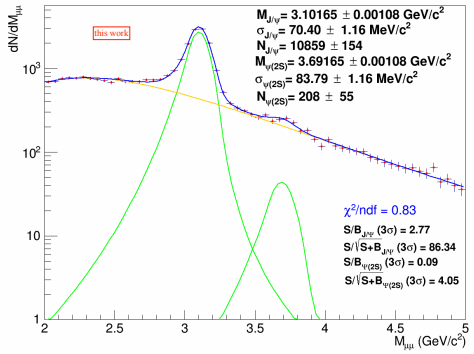

(a) $0 < p_T \leq 1$ *(GeV/c)*

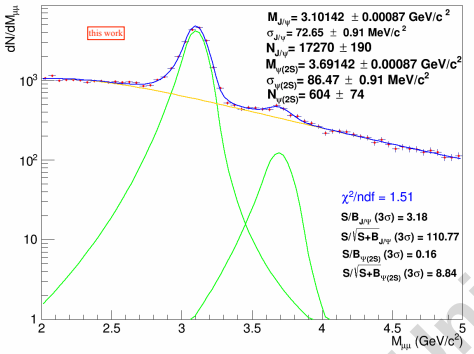

(b) $1 < p_T \leq 2$ *(GeV/c)*

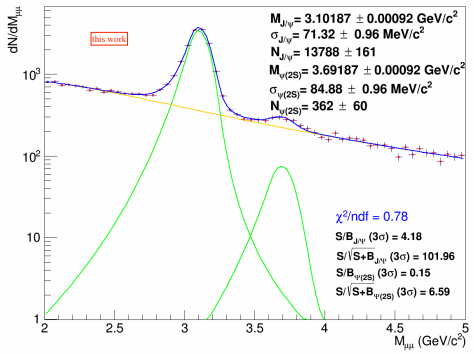

(c) $2 < p_T \leq 3$ *(GeV/c)*

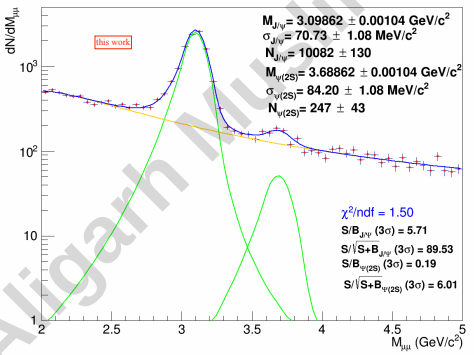

(d) $3 < p_T \leq 4$ *(GeV/c)*

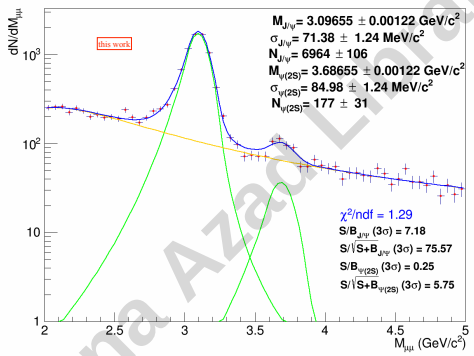

(e) $4 < p_T \leq 5$ *(GeV/c)*

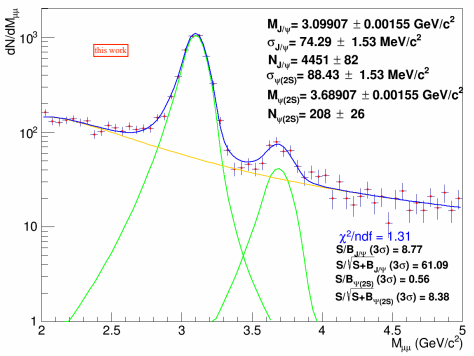

(f) $5 < p_T \leq 6$ *(GeV/c)*

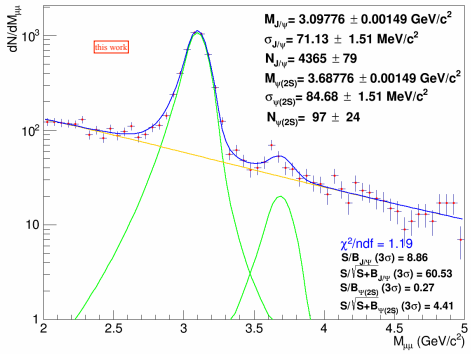

(g) $6 < p_T \leq 8$ *(GeV/c)*

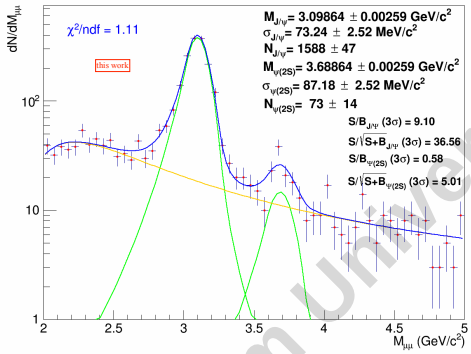

(h) $8 < p_T \leq 10$ *(GeV/c)*

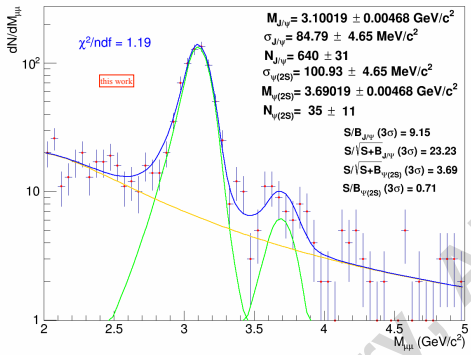

(i) $10 < p_T \leq 12$ *(GeV/c)*

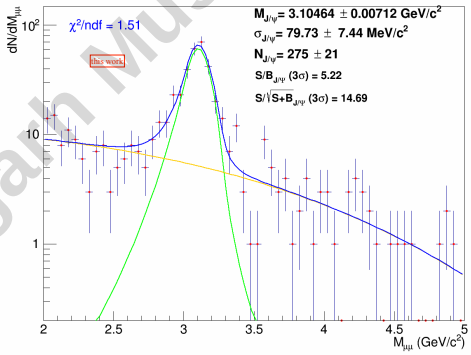

(j) $12 < p_T \leq 14$ *(GeV/c)*

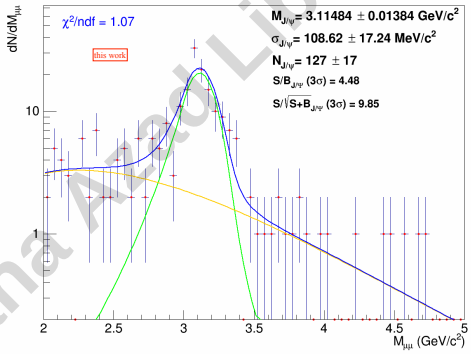

(k) $14 < p_T \leq 16$ *(GeV/c)*

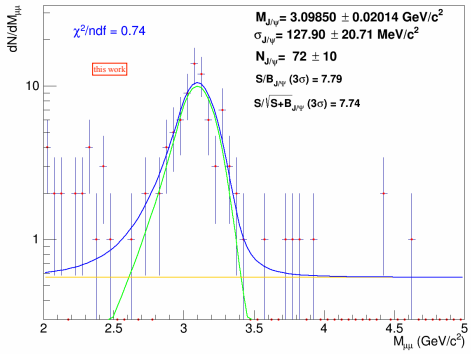

(l) $16 < p_T \leq 20$ *(GeV/c)*

Figure C.2: *Signal extraction in twelve p_T bins. CB2 function is used for fitting the J/ψ and $\psi(2S)$ signal, while VWG function is used for fitting the background. Above $p_T \geq 12$ (GeV/c) $\psi(2S)$ signal could not be extracted because of insignificant statistics.*

Bibliography

[1] D. Kharzeev [Proc. Quark Matter 97], *Theoretical interpretations of J/ψ suppression: A summary*, Nucl. Phys. A 638 (1998), no. 1, 279–290, https://doi.org/10.1016/S0375-9474(98)00366-2. (Cited on page 65.)

[2] J. P. Blaizot [Proc. Quark Matter 97], *QM '97 highlights-lepton-photon 2: The J/ψ puzzle*, Nucl. Phys. A 638 (1998), no. 1, 373–378, https://doi.org/10.1016/S0375-9474(98)00384-4. (Cited on page 65.)

[3] A. Andronic *et al.*, *Statistical hadronization of heavy flavor quarks in elementary collisions: Successes and failures*, Phys. Lett. B 678 (2009), no. Issue 4, 350–354, https://doi.org/10.1016/j.physletb.2009.06.051. (Cited on page 20.)

[4] A. Andronic *et al.*, *Thermal hadron production in relativistic nuclear collisions: The hadron mass spectrum, the horn, and the QCD phase transition*, Phys. Lett. B 673 (2009), no. Issue 2, 142–145, https://doi.org/10.1016/j.physletb.2009.02.014. (Cited on page 20.)

[5] A. Andronic *et al.*, *The statistical model in Pb–Pb collisions at the LHC*, Nucl. Phys. A 904-905 (2013), 535–538, https://doi.org/10.1016/j.nuclphysa.2013.02.070. (Cited on pages 28, 29, and 154.)

[6] A. Andronic *et al.*, *Heavy-flavour and quarkonium production in the LHC era: from proton–proton to heavy-ion collisions*, Eur. Phys. J C 76 (2016), no. 107, https://doi.org/10.1140/epjc/s10052-015-3819-5. (Cited on page 20.)

[7] A. Chodos, R. L. Jaffe, K. Johnson, C. B. Thorn, and V. F. Weisskopf, *New extended model of hadrons*, Phys. Rev. D 9 (1974), no. Issue 12, 3471, https://doi.org/10.1103/PhysRevD.9.3471. (Cited on page 13.)

[8] A. Cisek, W. Schöfer, and A. Szczurek, *Exclusive coherent production of heavy vector mesons in nucleus-nucleus collisions at energies available at the CERN Large Hadron Collider*, Phys. Rev. C 86 (2012), no. Issue 1, 014905, https://doi.org/10.1103/PhysRevC.86.014905. (Cited on page 30.)

[9] A. Fernández *et al.*, *Cosmic ray physics with the ALICE detectors*, Czech. J. Phys. 55 (2005), B801–B807. (Cited on page 57.)

[10] A. Ferrari *et al.*, *FLUKA: A multi-particle transport code (program version 2005)*, CERN Yellow Reports: Monographs, CERN (2005), http://cds.cern.ch/record/898301. (Cited on page 63.)

[11] A. K. Chaudhuri, *A short course on Relativistic Heavy Ion Collisions*, arXiv:1207.7028v1 (2012), https://arxiv.org/abs/1207.7028v1. (Cited on pages 5 and 159.)

[12] A. Shor and R. Longacre, *Effects of secondary interactions in proton-nucleus and nucleus-nucleus collisions using the HIJET event generator*, Phys. Lett. B 218 (1989), no. Issue 1, 100–104, https://doi.org/10.1016/0370-2693(89)90483-8. (Cited on page 92.)

[13] Adeola Adeluyi and C. A. Bertulani, *Constraining gluon shadowing using photoproduction in ultraperipheral pA and AA collisions*, Phys. Rev. C 85 (2012), no. Issue 4, 044904, https://doi.org/10.1103/PhysRevC.85.044904. (Cited on page 30.)

[14] ALICE Collaboration, *Technical proposal for A Large Ion Collider Experiment at the CERN LHC*, CERN-LHCC-95-71 (1995), http://cdsweb.cern.ch/record/293391. (Cited on pages 61 and 62.)

[15] ALICE Collaboration, *The forward muon spectrometer of ALICE : addendum to the technical proposal for a Large Ion Collider experiment at the CERN LHC*, CERN-LHCC-96-032 (1996), http://cdsweb.cern.ch/record/314011. (Cited on pages 61 and 65.)

[16] ALICE Collaboration, *The forward muon spectrometer of ALICE : addendum to the technical proposal for a Large Ion Collider experiment at the CERN LHC*, 1996, https://cds.cern.ch/record/314011. (Cited on pages 73, 74, and 156.)

[17] ALICE Collaboration, *ALICE high-momentum particle identification: Technical Design Report*, CERN-LHCC-98-019 (1998), http://cdsweb.cern.ch/record/381431. (Cited on page 54.)

[18] ALICE Collaboration, *ALICE: a transition radiation detector for electron identification within the ALICE central detector - an addendum to the Technical Proposal*, CERN-LHCC-99-013 (1999), http://cdsweb.cern.ch/record/401988. (Cited on page 61.)

[19] ALICE Collaboration, *ALICE dimuon forward spectrometer: Technical Design Report*, CERN-LHCC-99-022 (1999), http://cdsweb.cern.ch/record/401974. (Cited on pages 65, 75, 76, and 156.)

[20] ALICE Collaboration, *ALICE Inner Tracking System (ITS): Technical Design Report*, CERN-LHCC-99-012 (1999), http://edms.cern.ch/file/398932/1. (Cited on page 50.)

[21] ALICE Collaboration, *ALICE Photon Multiplicity Detector (PMD): Technical Design Report*, CERN-LHCC-99-032 (1999), http://cdsweb.cern.ch/record/451099. (Cited on page 58.)

[22] ALICE Collaboration, *ALICE Zero-Degree Calorimeter (ZDC): Technical Design Report*, CERN-LHCC-99-005 (1999), http://cdsweb.cern.ch/record/381433. (Cited on page 57.)

[23] ALICE Collaboration, *Technical design report of the photon spectrometer*, CERN-LHCC-99-004 (1999), http://cdsweb.cern.ch/record/381432. (Cited on page 56.)

[24] ALICE Collaboration, *ALICE dimuon forward spectrometer: addendum to the Technical Design Report*, CERN-LHCC-2000-046 (2000), http://cdsweb.cern.ch/record/494265. (Cited on page 65.)

[25] ALICE Collaboration, *ALICE Time-Of-Flight system (TOF): Technical Design Report*, CERN-LHCC-2000-012 (2000), http://cdsweb.cern.ch/record/430132. (Cited on page 53.)

[26] ALICE Collaboration, *ALICE Time Projection Chamber (TPC): Technical Design Report*, CERN-LHCC-2000-001 (2000), http://cdsweb.cern.ch/record/451098. (Cited on page 51.)

[27] ALICE Collaboration, *ALICE Transition Radiation Detector (TRD): Technical Design Report*, CERN-LHCC-2001-021 (2001), http://cdsweb.cern.ch/record/519145. (Cited on page 52.)

[28] ALICE Collaboration, *ALICE Time-Of Flight system (TOF): addendum to the technical design report*, CERN-LHCC-2002-016 (2002), http://cdsweb.cern.ch/record/545834. (Cited on page 53.)

[29] ALICE Collaboration, *ALICE Photon Multiplicity Detector (PMD): addendum to the technical design report*, CERN-LHCC-2003-038 (2003), http://cdsweb.cern.ch/record/642177. (Cited on page 58.)

[30] ALICE Collaboration, *ALICE trigger data-acquisition high-level trigger and control system: Technical Design Report*, CERN-LHCC-2003-062 (2003), http://cdsweb.cern.ch/record/684651. (Cited on page 60.)

[31] ALICE Collaboration, *ALICE trigger data-acquisition high-level trigger and control system: Technical Design Report*, CERN-LHCC-2003-062 (2003), http://cdsweb.cern.ch/record/684651. (Cited on page 61.)

[32] ALICE Collaboration, *ALICE forward detectors: FMD, TO and VO: Technical Design Report*, CERN-LHCC-2004-025 (2004), http://cdsweb.cern.ch/record/781854. (Cited on pages 59 and 60.)

[33] ALICE Collaboration, *ALICE electromagnetic calorimeter: addendum to the ALICE technical proposal*, CERN-LHCC-2006-014 (2006), http://cdsweb.cern.ch/record/932676. (Cited on pages 56 and 61.)

[34] ALICE Collaboration, *Centrality dependence of the charged-particle multiplicity density at midrapidity in Pb-Pb collisions at* $\sqrt{s_{NN}}$ = 5.02 *TeV*, ALICE Technical Report (2015), ALICE–PUBLIC–2015–008, https://cds.cern.ch/record/2118084. (Cited on page 92.)

[35] ALICE Collaboration, *Observation of a J/ψ yield excess at low* p_T *in Pb-Pb collisions at* $\sqrt{s_{NN}}$ = 2.76 *TeV*, ALICE Analysis Note (2017), no. ANA-315, https://alice-notes.web.cern.ch/node/315. (Cited on pages 101, 104, and 159.)

[36] ALICE Collaboration, *Centrality determination in heavy-ion collisions*, ALICE Public Note (2018), ALICE–PUBLIC–2014–XX, https://alice-notes.web.cern.ch/node/711. (Cited on pages 94 and 159.)

[37] ALICE website, https://aliceinfo.cern.ch/ArtSubmission/submitted. (Cited on page 48.)

[38] Andrew Purcell, *Go on a particle quest at the first CERN webfest*, (2012), no. BUL-NA-2012-269. 35/2012, 10, https://cds.cern.ch/record/1473657. (Cited on pages 4 and 153.)

[39] Giacomo Volpe [On behalf of ALICE Collaboration], *The High Momentum Particle IDentification (HMPID) detector PID performance and its contribution to the ALICE physics program*, Nucl. Instrum. Meth. A 876 (2017), 133–136, https://doi.org/10.1016/j.nima.2017.02.037. (Cited on pages 55 and 155.)

[40] Bernard R. Hicks, *Differential Production Cross-Section of Heavy-Flavor Electrons in $\sqrt{s}$ = 2.76 TeV pp collisions at the LHC with the ALICE detector*, Ph.D. thesis, Yale University, 2013, http://rhig.physics.yale.edu/Theses.html. (Cited on pages 14 and 153.)

[41] Boris Teyssier, *Light-neutral meson production in pp collisions at $\sqrt{s}$ = 13 TeV at forward rapidity in ALICE at the CERN LHC*, Ph.D. thesis, Université de Lyon, 2017, http://cds.cern.ch/record/2310922. (Cited on pages 62, 82, 155, and 156.)

[42] C. Lefevre, *LHC Guide*, (2017), no. CERN-Brochure-2017-002-Eng, https://cds.cern.ch/record/2255762. (Cited on page 40.)

[43] C. Loizides, J. Kamin, and D. d'Enterria, *Improved Monte Carlo Glauber predictions at present and future nuclear colliders*, Phys. Rev. C 97 (2018), no. Issue 5, 054910, https://doi.org/10.1103/PhysRevC.97.054910. (Cited on page 93.)

[44] C. R. Allton *et al.*, *Thermodynamics of two flavor QCD to sixth order in quark chemical potential*, Phys. Rev. D 71 (2005), no. Issue 5, 054508, https://doi.org/10.1103/PhysRevD.71.054508. (Cited on page 13.)

[45] C. Y. Wong, *Introduction to High-Energy Heavy-Ion Collisions*, 1st ed., World Scientific Publishing Co. Pte. Ltd., 1994. (Cited on page 49.)

[46] C. Y. Wong, *Lectures on the Near-Side Ridge, Landau Hydrodynamics, and Heavy Quarkonia in High Energy Heavy-Ion Collisions*, EPJ Web of Conferences 7 (2010), no. 01006, 50, https://doi.org/10.1051/epjconf/20100701006. (Cited on page 16.)

[47] CERN, *Latest update in the search for the Higgs boson*, (2012), https://indico.cern.ch/event/197461. (Cited on page 41.)

[48] CERN website, https://home.cern/about. (Cited on page 40.)

[49] Christof Gattringer and Christian B. Lang, *Quantum Chromodynamics on the Lattice*, 1st ed., Springer, 2010. (Cited on page 13.)

[50] Claudio GEUNA, *J/ψ production in proton-proton collisions at $\sqrt{s} = 2.76$ and 7 TeV in the ALICE Forward Muon Spectrometer at LHC*, Ph.D. thesis, Université Paris Sud, Paris, 2012, http://cds.cern.ch/record/1557080. (Cited on pages 72 and 156.)

[51] A. Adare *et al.* [PHENIX Collaboration], *Detailed measurement of the e^+e^- pair continuum in $p + p$ and Au + Au collisions at $\sqrt{s_{NN}} = 200$ GeV and implications for direct photon production*, Phys. Rev. C 81 (2010), no. Issue 3, 034911, https://doi.org/10.1103/PhysRevC.81.034911. (Cited on page 19.)

[52] A. Adare *et al.* [PHENIX Collaboration], *J/ψ suppression at forward rapidity in Au+Au collisions at $\sqrt{s_{NN}} = 200$ GeV*, Phys. Rev. C 84 (2011), no. Issue 5, 054912, https://doi.org/10.1103/PhysRevC.84.054912. (Cited on pages 33, 34, and 154.)

[53] A. Augusto Alves Jr *et al.* [LHCb Collaboration], *The LHCb Detector at the LHC*, JINST 3 (2008), no. S08005, http://dx.doi.org/10.1088/1748-0221/3/08/S08005. (Cited on page 44.)

[54] A. Bazavov *et al.* [HotQCD Collaboration], *Chiral and deconfinement aspects of the QCD transition*, Phys. Rev. D 85 (2012), no. Issue 5, 054503, https://doi.org/10.1103/PhysRevD.85.054503. (Cited on page 13.)

[55] A. Bazavov *et al.* [HotQCD Collaboration], *Equation of state in (2+1)-flavor QCD*, Phys. Rev. D 90 (2014), no. Issue 9, 094503, https://doi.org/10.1103/PhysRevD.90.094503. (Cited on page 13.)

[56] A. Fernández *et al.* [The ACORDE Collaboration], *ACORDE a cosmic ray detector for ALICE*, Nucl. Instrum. Meth. A 572 (2007), no. Issue 1, 102–103, https://doi.org/10.1016/j.nima.2006.10.336. (Cited on page 57.)

[57] A. N. Akindinov *et al.* [ALICE Collaboration], *Particle identification with the ALICE TOF detector at very high particle multiplicity*, Eur. Phys. J. C 32 (2004), no. 1, s165–s177, https://doi.org/10.1140/epjcd/s2003-01-0013-5. (Cited on page 54.)

[58] A. Rimai *et al.* [ALICE Collaboration], *Spatial Resolution Studies in Cathode Pad and in Cathode Strip Chambers*, ALICE Internal Note (1997), ALICE–INT–1997–23, https://edms.cern.ch/document/106754/1.0. (Cited on page 70.)

[59] A. Sansoni *et al.* [The CDF Collaboration], *Quarkonia production at CDF*, Nucl. Phys. A 610 (1996), 373–385, https://doi.org/10.1016/S0375-9474(96)00371-5. (Cited on page 66.)

[60] A. Zinchenko and G. Shabratova [ALICE Collaboration], *A new approach to cluster finding and hit reconstruction in cathode pad chambers and its development for the forward muon spectrometer of ALICE*, Nucl. Instrum. Methods A 502 (2003), no. Issues 2-3, 778–780, https://doi.org/10.1016/S0168-9002(03)00580-1. (Cited on page 71.)

[61] A. Zintchenko *et al.* [ALICE Collaboration], *A new approach to cluster finding and hit reconstruction in muon chambers of ALICE*, ALICE Internal Note (2003), ALICE–INT–2003–006, https://edms.cern.ch/document/373848/1. (Cited on page 70.)

[62] Alberica Toia & David Chinellato [ALICE Collaboration], *Centrality determination in Pb-Pb collisions at* $\sqrt{s_{NN}}$ *= 5.02 TeV*, ALICE Analysis Note (2017), ALICE–ANA–2015–2838, https://alice-notes.web.cern.ch/system/files/notes/analysis/453/2017-Sep-26-analysis_note-ALICE_analysis_note.pdf. (Cited on pages 92, 93, and 157.)

[63] ALICE TWiki webpage [ALICE Collaboration], *2015 J/ψ to mumu and Raa* , https://twiki.cern.ch/twiki/bin/viewauth/ALICE/JPsiPbPb2015Raa. (Cited on page 106.)

[64] ALICE TWiki webpage [ALICE Collaboration], *Dimuon Forward Spectrometer: Tracking chambers*, https://twiki.cern.ch/twiki/bin/view/ALICE/MuonTracking. (Cited on pages 67 and 156.)

[65] ALICE TWiki webpage [ALICE Collaboration], *Monitoring the data/MC agreement of tracking chamber status maps*, https://twiki.cern.ch/twiki/bin/viewauth/ALICE/MuonRejectList. (Cited on page 79.)

[66] ALICE TWiki webpage [ALICE Collaboration], *PbPb collisions – QA for 2015*, https://twiki.cern.ch/twiki/pub/ALICE/MuonPbPbQA2015. (Cited on page 97.)

[67] AliPhysics [ALICE Collaboration], *ALICE Software Reference Manual*, 2018, http://alidoc.cern.ch/AliPhysics. (Cited on page 62.)

[68] AliRoot [ALICE Collaboration], *ALICE Software Reference Manual*, 2018, http://alidoc.cern.ch/AliRoot. (Cited on page 62.)

[69] Ananya *et al.* [ALICE Collaboration], *O^2: A novel combined online and offline computing system for the ALICE Experiment after 2018*, J. Phys.: Conf. Series 513 (2014), no. 1, 012037, http://stacks.iop.org/1742-6596/513/i=1/a=012037. (Cited on page 63.)

[70] B. Abelev *et al.* [ALICE Collaboration], *Inclusive J/ψ production in pp collisions at* $\sqrt{s} = 2.76$ *TeV*, Phys. Lett. B 718 (2012), no. Issue 2, 295–306, https://doi.org/10.1016/j.physletb.2012.10.078. (Cited on page 96.)

[71] B. Abelev *et al.* [ALICE Collaboration], *J/ψ production as a function of charged particle multiplicity in pp collisions at* $\sqrt{s} = 7$ *TeV*, Phys. Lett. B 712 (2012), no. Issue 3, 165–175, https://doi.org/10.1016/j.physletb.2012.04.052. (Cited on page 96.)

[72] B. Abelev *et al.* [ALICE Collaboration], *Measurement of charm production at central rapidity in proton-proton collisions at* $\sqrt{s} = 2.76$ *TeV*, JHEP 07 (2012), 191, https://doi.org/10.1007/JHEP07(2012)191. (Cited on page 20.)

[73] B. Abelev *et al.* [ALICE Collaboration], *Centrality dependence of π, K, and p production in Pb-Pb collisions at* $\sqrt{s} = 2.76$ *TeV*, Phys. Rev. C 88 (2013), no. Issue 4, 044910, https://doi.org/10.1016/j.physletb.2009.02.014. (Cited on page 20.)

[74] B. Abelev *et al.* [ALICE Collaboration], *Centrality determination of Pb-Pb Collisions at* $\sqrt{s_{NN}} = 2.76$ *TeV with ALICE*, Phys. Rev. C 88 (2013), no. Issue 4, 044909, http://dx.doi.org/10.1103/PhysRevC.88.044909. (Cited on pages 18, 91, and 92.)

[75] B. Abelev *et al.* [ALICE Collaboration], *Coherent J/ψ photoproduction in ultra-peripheral Pb–Pb collisions at* $\sqrt{s_{NN}} = 2.76$ *TeV*, Phys. Lett. B 718 (2013), no. Issue 4-5, 1273–1283, https://doi.org/10.1016/j.physletb.2012.11.059. (Cited on pages 94, 96, 97, and 157.)

[76] B. Abelev *et al.* [ALICE Collaboration], *Pseudorapidity Density of Charged Particles in p-Pb Collisions at* $\sqrt{s_{NN}} = 5.02$ *TeV*, Phys. Rev. Lett. 110 (2013), no. Issue 3, 032301, https://doi.org/10.1103/PhysRevLett.110.032301. (Cited on page 93.)

[77] B. Abelev *et al.* [ALICE Collaboration], *Centrality, rapidity and transverse momentum dependence of J/ψ suppression in Pb–Pb collisions at* $\sqrt{s_{NN}} = 2.76$ *TeV*, Phys. Lett. B 734 (2014), 314–327, https://doi.org/10.1016/j.physletb.2014.05.064. (Cited on pages 20, 27, 28, 30, 33, 153, and 154.)

[78] B. Abelev *et al.* [ALICE Collaboration], *Measurement of quarkonium production at forward rapidity in pp collisions at* $\sqrt{s} = 7$ *TeV*, Eur. Phys. J. C 74 (2014), 2974, https://doi.org/10.1140/epjc/s10052-014-2974-4. (Cited on page 96.)

[79] B. Abelev *et al.* [ALICE Collaboration], *Performance of the ALICE experiment at the CERN LHC*, Int. J. Mod. Phys. A 29 (2014), no. 24, 1430044, http://dx.doi.org/10.1142/S0217751X14300440. (Cited on pages 45, 46, 48, 60, and 155.)

[80] B. Alessandro *et al.* [ALICE Collaboration], *ALICE: Physics Performance Report, Volume II*, J. Phys. G: Nucl. Part. Phys. 32 (2006), no. 10, 1295–2040, http://dx.doi.org/10.1088/0954-3899/32/10/001. (Cited on pages 45, 46, 48, 54, 56, 57, and 155.)

[81] D. Evans *et al.* [ALICE Collaboration], *ALICE Trigger System*, Proceedings of the 10th Workshop on Electronics for LHC and Future Experiments, Boston, USA (2004), no. CERN-2004-010, 277–280, http://cds.cern.ch/record/814257. (Cited on page 60.)

[82] D. Evans *et al.* [ALICE Collaboration], *The ALICE Central Trigger Processor*, Proceedings of the 11th Workshop on Electronics for LHC and Future Experiments, Heidelberg, Germany (2005), no. CERN-2005-011, 284–288, http://cds.cern.ch/record/921038. (Cited on page 60.)

[83] D. Swoboda [ALICE Collaboration], *ALICE Muon Arm Dipole Magnet: Conceptual Design Report*, ALICE Internal Note (1999), ALICE–INT–1999–06, http://cds.cern.ch/record/689306. (Cited on page 69.)

[84] E. Abbas *et al.* [ALICE Collaboration], *Charmonium and e^+e^- pair photoproduction at mid-rapidity in ultra-peripheral Pb–Pb collisions at $\sqrt{s_{NN}} = 2.76$ TeV*, Eur. Phys. J C 73 (2013), no. 2617, https://doi.org/10.1140/epjc/s10052-013-2617-1. (Cited on pages 30 and 94.)

[85] F. Carminati *et al.* [ALICE Collaboration], *ALICE: Physics Performance Report, Volume I*, J. Phys. G: Nucl. Part. Phys. 30 (2004), no. 11, 1517–1763, http://dx.doi.org/10.1088/0954-3899/30/11/001. (Cited on pages 45, 46, 48, 54, 55, 56, 57, and 155.)

[86] G. Aad *et al.* [ATLAS Collaboration], *The ATLAS Experiment at the CERN Large Hadron Collider*, JINST 3 (2008), no. S08003, http://dx.doi.org/10.1088/1748-0221/3/08/S08003. (Cited on page 43.)

[87] G. Aad *et al.* [ATLAS Collaboration], *Observation of a new particle in the search for the Standard Model Higgs boson with the ATLAS detector at the LHC*, Phys. Lett. B 716 (2012), no. Issue 1, 1–29, http://dx.doi.org/10.1016/j.physletb.2012.08.020. (Cited on page 41.)

[88] G. Aad *et al.* [ATLAS Collaboration], *Measurement of Z-boson production in Pb–Pb collisions at $\sqrt{s_{NN}} = 2.76$ TeV with the ATLAS Detector*, Phys. Rev. Lett. 110 (2013), 022301, https://doi.org/10.1103/PhysRevLett.110.022301. (Cited on page 23.)

[89] G. Anelli *et al.* [TOTEM Collaboration], *The TOTEM Experiment at the CERN Large Hadron Collider*, JINST 3 (2008), no. S08007, http://dx.doi.org/10.1088/1748-0221/3/08/S08007. (Cited on page 44.)

[90] G. Chabratova *et al.* [ALICE Collaboration], *Development of the Kalman filter for tracking in the forward muon spectrometer of ALICE*, ALICE Internal Note (2003), ALICE–INT–2003–002, https://edms.cern.ch/document/371480/1. (Cited on pages 70, 71, and 72.)

[91] Igor Lakomov [ALICE Collaboration], *Quarkonium signal extraction in ALICE*, ALICE-PUBLIC-2015-006 (2015), https://cds.cern.ch/record/2060096. (Cited on page 123.)

[92] J. Adam *et al.* [ALICE Collaboration], *Centrality dependence of particle production in p-Pb collisions at* $\sqrt{s_{NN}}$ = 5.02 *TeV*, Phys. Rev. C 91 (2015), no. Issue 6, 064905, https://doi.org/10.1103/PhysRevC.91.064905. (Cited on page 18.)

[93] J. Adam *et al.* [ALICE Collaboration], *Inclusive, prompt and non-prompt J/ψ production at mid-rapidity in Pb-Pb collisions at* $\sqrt{s}$ = *2.76 TeV*, JHEP 07 (2015), 051, https://doi.org/10.1007/JHEP07(2015)051. (Cited on pages 34 and 154.)

[94] J. Adam *et al.* [ALICE Collaboration], *Centrality Dependence of the Charged-Particle Multiplicity Density at Midrapidity in Pb-Pb Collisions at* $\sqrt{s_{NN}}$ = 5.02 *TeV*, Phys. Rev. Lett. 116 (2016), no. Issue 22, 222302, https://journals.aps.org/prl/pdf/10.1103/PhysRevLett.116.222302. (Cited on pages 48 and 91.)

[95] J. Adam *et al.* [ALICE Collaboration], *Measurement of an Excess in the Yield of* J/ψ *at Very Low* p_T *in Pb-Pb Collisions at* $\sqrt{s_{NN}}$ = *2.76 TeV*, Phys. Rev. Lett. 116 (2016), no. Issue 22, 222301, https://link.aps.org/doi/10.1103/PhysRevLett.116.222301. (Cited on pages 27, 91, 94, 95, and 157.)

[96] J. Adam *et al.* [ALICE Collaboration], *J/ψ suppression at forward rapidity in Pb-Pb collisions at* $\sqrt{s_{NN}}$ = *5.02 TeV*, Phys. Lett. B 766 (2017), 212–224, https://doi.org/10.1016/j.physletb.2016.12.064. (Cited on pages 27, 28, 29, 153, and 154.)

[97] J. Castillo [ALICE Collaboration], *Alignment of the ALICE MUON spectrometer*, 1st LHC Detector Alignment Workshop, CERN, Geneva, Switzerland, 4 - 6 Sep 2006 (2007), 127–138, http://cds.cern.ch/record/1047110. (Cited on page 72.)

[98] J. Peyré, B. Genolini and J. Pouthas [ALICE Collaboration], *A full-scale prototype for the tracking chambers of the ALICE muon spectrometer. Part I: mechanics, anode and cathode plane design, assembly and construction*, ALICE Internal Note (1998), ALICE–INT–1998–28, https://edms.cern.ch/document/106760/1.0. (Cited on page 71.)

[99] K. Aamodt *et al.* [ALICE Collaboration], *The ALICE experiment at the CERN LHC*, JINST 3 (2008), no. S08002, http://dx.doi.org/10.1088/1748-0221/3/08/S08002. (Cited on pages 43, 45, 46, 47, 48, 52, 54, 55, 57, 70, and 155.)

[100] K. Aamodt *et al.* [ALICE Collaboration], *Alignment of the ALICE Inner Tracking System with cosmic-ray tracks*, JINST 5 (2010), no. P03003, https://cds.cern.ch/record/1231809. (Cited on pages 50 and 155.)

[101] K. Aamodt *et al.* [ALICE Collaboration], *Centrality Dependence of the Charged-Particle Multiplicity Density at Midrapidity in Pb-Pb Collisions at* $\sqrt{s_{NN}} = 2.76$ *TeV*, Phys. Rev. Lett. 106 (2011), 032301, https://doi.org/10.1103/PhysRevLett.106.032301. (Cited on page 23.)

[102] K. Aamodt *et al.* [ALICE Collaboration], *Rapidity and transverse momentum dependence of inclusive J/ψ production in pp collisions at* $\sqrt{s} = 7$ *TeV*, Phys. Lett. B 704 (2011), no. Issue 5, 442–455, https://doi.org/10.1016/j.physletb.2011.09.054. (Cited on page 96.)

[103] L. Antoniazzi *et al.* [E705 Collaboration], *Measurement of J/ψ and ψ′ production in 300-GeV/c proton, antiproton, and* $\pi^{\pm}$ *interactions with nuclei*, Phys. Rev. D 46 (1992), no. 11, 4828, https://doi.org/10.1103/PhysRevD.46.4828. (Cited on page 26.)

[104] L. Antoniazzi *et al.* [E705 Collaboration], *Measurement of J/ψ via ψ′ and X decay in 300-GeV/c proton and* $\pi^{\pm}$ *interactions with nuclei*, Phys. Rev. Lett. 70 (1992), no. 4, 383, https://doi.org/10.1103/PhysRevLett.70.383. (Cited on page 26.)

[105] L. Aphecetche *et al.* [ALICE Collaboration], *Numerical Simulations and Offline Reconstruction of the Muon Spectrometer of ALICE*, ALICE Internal Note (2009), ALICE–INT–2009–044, https://edms.cern.ch/document/1054937/1. (Cited on page 71.)

[106] L. Aphecetche *et al.* [ALICE Collaboration], *Numerical Simulations and Offline Reconstruction of the Muon Spectrometer of ALICE*, ALICE Internal Note (2009), ALICE–INT–2009–044, https://edms.cern.ch/document/1054937/1. (Cited on page 72.)

[107] M. Arba *et al.* [ALICE Collaboration], *Assembly of a large slat chamber prototype for the ALICE Muon Spectrometer*, ALICE Internal Note (2002), ALICE–INT–2002–17, https://edms.cern.ch/document/347613/1. (Cited on page 71.)

[108] Mesut Arslandok [ALICE Collaboration], *ALICE Figure Repository*, https://aliceinfo.cern.ch/Figure/node/9219. (Cited on page 53.)

[109] Mohamad Tarhini [ALICE Collaboration], *ALICE Figure Repository*, https://aliceinfo.cern.ch/Figure/node/8886. (Cited on pages 100 and 157.)

[110] N. Bastid *et al.* [ALICE Collaboration], *Test Experiment for the Beam Shielding in ALICE*, ALICE Internal Note (1996), ALICE–INT–1996–14, https://edms.cern.ch/document/106926/1.0. (Cited on page 68.)

[111] Nicolo Jacazio [ALICE Collaboration], *ALICE Figure Repository*, https://aliceinfo.cern.ch/Figure/node/9150. (Cited on page 53.)

[112] O. Adriani *et al.* [LHCf Collaboration], *The LHCf detector at the CERN Large Hadron Collider*, JINST 3 (2008), no. S08006, http://dx.doi.org/10.1088/1748-0221/3/08/S08006. (Cited on page 44.)

[113] O. Baillie *et al.* [ALICE Collaboration], *Recent developments on the ALICE central Trigger processor*, Proceedings of the 12th Workshop on Electronics for LHC and Future Experiments, Valencia, Spain (2007), no. CERN-2007-001, 341–345, http://cds.cern.ch/record/1027489. (Cited on page 60.)

[114] R. Aaij *et al.* [LHCb Collaboration], *Measurement of J/ψ production in pp collisions at* $\sqrt{s} = 7$ *TeV*, Eur. Phys. J. C 71 (2011), 1645, https://doi.org/10.1140/epjc/s10052-011-1645-y. (Cited on page 96.)

[115] R. Aaij *et al.* [LHCb Collaboration], *Measurement of J/ψ production in pp collisions at* $\sqrt{s} = 2.76$ *TeV*, JHEP 41 (2013), 2013, https://doi.org/10.1007/JHEP02(2013)041. (Cited on page 96.)

[116] R. Wurzinger, Y. Le Bornec and N. Willis [ALICE Collaboration], *MonteCarlo Studies on Cathode Strip/Pad Chambers for the ALICE Di-Muon Arm*, ALICE Internal Note (1997), ALICE–INT–1997–10, https://edms.cern.ch/document/106932/1.0. (Cited on page 70.)

[117] S. Acharya *et al.* [ALICE Collaboration], *Sequential regeneration of charmonia in heavy-ion collisions*, Nuclear Phys. A 943 (2015), 147–158, https://doi.org/10.1016/j.nuclphysa.2015.09.006. (Cited on pages 29, 31, and 154.)

[118] S. Acharya *et al.* [ALICE Collaboration], *J/ψ elliptic flow in Pb-Pb collisions at* $\sqrt{s_{NN}} = 5.02$ *TeV*, Phys. Rev. Lett. 119 (2017), no. Issue 24, 242301, https://doi.org/10.1103/PhysRevLett.119.242301. (Cited on pages 31 and 154.)

[119] S. Acharya *et al.* [ALICE Collaboration], *D-Meson Azimuthal Anisotropy in Midcentral Pb-Pb Collisions at* $\sqrt{s_{NN}} = 5.02$ *TeV*, Phys. Rev. Lett. 120 (2018), no. Issue 10, 102301, https://doi.org/10.1103/PhysRevLett.120.102301. (Cited on pages 31 and 154.)

[120] S. Acharya *et al.* [ALICE Collaboration], *Measurement of* Z^0*-boson production at large rapidities in Pb–Pb collisions at* $\sqrt{s_{NN}} = 5.02$ *TeV*, Phys. Lett. B 780 (2018), 372–383, https://doi.org/10.1016/j.physletb.2018.03.010. (Cited on pages 20 and 23.)

[121] S. Afanasiev *et al.* [PHENIX Collaboration], *Photoproduction of J/ψ and of high mass* e^+e^- *in ultraperipheral Au + Au collisions at* $\sqrt{s_{NN}} = 200$ *GeV*, Phys. Lett. B 679 (2009), no. Issue 4, 321–329, https://doi.org/10.1016/j.physletb.2009.07.061. (Cited on page 94.)

[122] S. Afanasiev *et al.* [PHENIX Collaboration], *Measurement of Direct Photons in Au + Au Collisions at* $\sqrt{s_{NN}} = 200$ *GeV*, Phys. Rev. Lett. 109 (2012), no. Issue 15, 152302, https://doi.org/10.1103/PhysRevLett.109.152302. (Cited on page 23.)

[123] S. Chatrchyan *et al.* [CMS Collaboration], *The CMS Experiment at the CERN LHC*, JINST 3 (2008), no. S08004, http://dx.doi.org/10.1088/1748-0221/3/08/S08004. (Cited on page 43.)

[124] S. Chatrchyan *et al.* [CMS Collaboration], *Jet momentum dependence of jet quenching in PbPb collisions at* $\sqrt{s_{NN}} = 2.76$ *TeV*, Phys. Lett. B 712 (2012), no. Issue 3, 176–197, https://doi.org/10.1016/j.physletb.2012.04.058. (Cited on page 20.)

[125] S. Chatrchyan *et al.* [CMS Collaboration], *Observation of a new boson at a mass of 125 GeV with the CMS experiment at the LHC*, Phys. Lett. B 716 (2012), no. Issue 1, 30–61, http://dx.doi.org/10.1016/j.physletb.2012.08.021. (Cited on page 41.)

[126] S. Chatrchyan *et al.* [CMS Collaboration], *Study of W boson production in PbPb and pp collisions at* $\sqrt{s_{NN}} = 2.76$ *TeV*, Phys. Lett. B 715 (2012), 66–87, https://doi.org/10.1016/j.physletb.2012.07.025. (Cited on page 23.)

[127] S. Chatrchyan *et al.* [CMS Collaboration], *Study of Z production in PbPb and pp collisions at* $\sqrt{s_{NN}} = 2.76$ *TeV in the dimuon and dielectron decay channels*, JHEP 03 (2015), 022, https://doi.org/10.1007/JHEP03(2015)022. (Cited on pages 20 and 23.)

[128] S. Grigoryan [ALICE Collaboration], *Contribution of Secondary π/K Mesons, produced in the Absorber, into the Dimuon Background in Pb-Pb Collisions*, ALICE Internal Note (2002), ALICE–INT–2002–06, https://edms.cern.ch/document/338221/2. (Cited on page 67.)

[129] V. Khachatryan *et al.* [CMS Collaboration], *Study of W boson production in pPb collisions at* $\sqrt{s_{NN}} = 5.02$ *TeV*, Phys. Lett. B 750 (2015), 565–586, https://doi.org/10.1016/j.physletb.2015.09.057. (Cited on page 20.)

[130] Vasiliki, A Mitsou [For MoEDAL Collaboration], *The MoEDAL experiment at the LHC: status and results*, Journal of Physics: Conference Series 873 (2017), no. 1, 012010, http://dx.doi.org/10.1088/1742-6596/873/1/012010. (Cited on page 44.)

[131] Y. Fukuda *et al.* [Super-Kamiokande Collaboration], *Evidence for Oscillation of Atmospheric Neutrinos*, Phys. Rev. Lett. 81 (1998), no. Issue 8, 1562, https://doi.org/10.1103/PhysRevLett.81.1562. (Cited on page 6.)

[132] Yasser Corrales Morales [ALICE Collaboration], *ALICE Figure Repository*, https://aliceinfo.cern.ch/Figure/node/9866. (Cited on pages 51 and 155.)

[133] D. H. Perkins, *Introduction to High Energy Physics*, 4th ed., Cambridge University Press, 2000. (Cited on pages 5, 43, and 159.)

[134] D. J. Griffiths, *Introduction to Elementary Particles*, 2nd, revised ed., WILEY-VCH Verlag GmbH & Co. KGaA, 2008. (Cited on page 10.)

[135] D. J. Gross and F. Wilczek, *Asymptotically Free Gauge Theories. I*, Phys. Rev. D 8 (1973), no. 10, 3633, https://doi.org/10.1103/PhysRevD.8.3633. (Cited on page 10.)

[136] D. J. Gross and F. Wilczek, *Ultraviolet Behavior of Non-Abelian Gauge Theories*, Phys. Rev. Lett. 30 (1973), no. 26, 1343, https://doi.org/10.1103/PhysRevLett.30.1343. (Not cited.)

[137] D. J. Gross and F. Wilczek, *Asymptotically Free Gauge Theories. II*, Phys. Rev. D 9 (1974), no. 4, 980, https://doi.org/10.1103/PhysRevD.9.980. (Cited on page 10.)

[138] D. Kharzeev, E. Levin, and M. Nardi, *Color glass condensate at the LHC: Hadron multiplicities in pp, pA and AA collisions*, Nucl. Phys. A 747 (2005), no. Issue 2-4, 609–629, https://doi.org/10.1016/j.nuclphysa.2004.10.018. (Cited on page 92.)

[139] E. G. Ferreiro, *Charmonium dissociation and recombination at LHC: Revisiting comovers*, Phys. Lett. B 731 (2014), 57–63, https://doi.org/10.1016/j.physletb.2014.02.011. (Cited on pages 28, 29, and 154.)

[140] E. G. Ferreiro, *Excited charmonium suppression in proton–nucleus collisions as a consequence of comovers*, Phys. Lett. B 749 (2015), 98–103, https://doi.org/10.1016/j.physletb.2015.07.066. (Cited on pages 28, 29, and 154.)

[141] E. Mathieson, *Cathode charge distributions in multiwire chambers: 4. Empirical formula for small anode-cathode separation*, Nucl. Instrum. Methods A 270 (1988), no. Issues 2-3, 602–603, https://doi.org/10.1016/0168-9002(88)90736-X. (Cited on pages 71 and 80.)

[142] E. V. Shuryak, *Quark-gluon plasma and hadronic production of leptons, photons and psions*, Phys. Lett. B 78 (1978), no. Issue 1, 150–153, https://doi.org/10.1016/0370-2693(78)90370-2. (Cited on page 13.)

[143] F. Halzen and A. D. Martin, *QUARKS AND LEPTONS: An Introductory Course in Modern Particles Physics*, 1st ed., JOHN WILEY & SONS, 1984. (Cited on page 10.)

[144] F. Karsch, *Lattice QCD at High Temperature and Density*, arXiv:hep-lat/0106019v2 (2001), https://arxiv.org/abs/hep-lat/0106019v2. (Cited on pages 14 and 15.)

[145] F. Karsch, *Lattice results on QCD thermodynamics*, Nuclear Physics A 698 (2002), no. Issues 1-4, 199–208, https://doi.org/10.1016/S0375-9474(01)01365-3. (Cited on page 15.)

[146] F. Karsch *et al.*, *Sequential charmonium dissociation*, Phys. Lett. B 637 (2006), no. Issues 1-2, 75–80, https://doi.org/10.1016/j.physletb.2006.03.078. (Cited on page 26.)

[147] Federico Ronchetti, *ALICE: from LS1 to readiness for Run2*, ALICE MATTERS (2015), http://alicematters.web.cern.ch/?q=ALICE_LS1_readiness. (Cited on page 52.)

[148] Florent Staley and Ermanno Vercellin, *ALICE gets ready to pinpoint muon pairs*, CERN Courier (2007), http://cerncourier.com/cws/article/cern/31866. (Cited on pages 66 and 155.)

[149] G. Blanchard, P. Crochet and P. Dupieux, *The local trigger electronics of the ALICE dimuon trigger*, ALICE Internal Note (2003), no. ALICE-EN-2003-010, https://cds.cern.ch/record/1066018. (Cited on page 74.)

[150] Ginéz Martínez García, *Advances in Quark Gluon Plasma*, arXiv:1304.1452 (2013), https://arxiv.org/abs/1304.1452. (Cited on pages 12, 15, 17, and 153.)

[151] M. Tanabashi *et al.* [Particle Data Group], *Review of Particle Physics*, Phys. Rev. D 98 (2018), no. 3, 030001, https://doi.org/10.1103/PhysRevD.98.030001. (Cited on pages 11, 12, 23, 102, and 153.)

[152] H. D. Politzer, *Reliable Perturbative Results for Strong Interactions?*, Phys. Rev. Lett. 30 (1973), no. 26, 1346, https://doi.org/10.1103/PhysRevLett.30.1346. (Cited on page 10.)

[153] H. De Vries, C. W. De Jager, and C. De Vries, *Nuclear charge-density-distribution parameters from elastic electron scattering*, Atomic Data and Nuclear Data Tables 36 (1987), no. Issues 3, 495–536, https://doi.org/10.1016/0092-640X(87)90013-1. (Cited on page 92.)

[154] H R Schmidt and J Schukraft, *The physics of ultra-relativistic heavy-ion collisions*, J. Phys. G: Nucl. Part. Phys. 19 (1993), no. 11, 1705–1795, https://doi.org/10.1088/0954-3899/19/11/006. (Cited on page 17.)

[155] H. Satz, *Colour deconfinement and quarkonium binding*, J. Phys. G: Nucl. and Particle Phys. 32 (2006), no. 3, https://doi.org/10.1088/0954-3899/32/3/R01. (Cited on pages 24 and 159.)

[156] J. C. Collins and M. J. Perry, *Superdense Matter: Neutrons or Asymptotically Free Quarks?*, Phys. Rev. Lett. 34 (1975), no. Issue 21, 1353, https://doi.org/10.1103/PhysRevLett.34.1353. (Cited on pages 7 and 13.)

[157] J. Cleymans, R. V. Gavai and E. Suhonen, *Quarks and gluons at high temperatures and densities*, Physics Reports 130 (1986), no. 4, 217–292, https://doi.org/10.1016/0370-1573(86)90169-9. (Cited on page 7.)

[158] J. D. Bjorken, *Highly relativistic nucleus-nucleus collisions: The central rapidity region*, Phys. Rev. D 27 (1983), no. Issue 1, 140, https://doi.org/10.1103/PhysRevD.27.140. (Cited on pages 16 and 18.)

[159] J. Gaiser, *Charmonium Spectroscopy From Radiative Decays of the J/ψ and ψ(2S)*, Ph.D. thesis, SLAC, 1982, http://www.slac.stanford.edu/cgi-wrap/getdoc/slac-r-255.pdf. (Cited on page 123.)

[160] J. P. Blaizot *et al.*, *Self-consistent hard-thermal-loop thermodynamics for the quark-gluon plasma*, Physics Lett. B 470 (1999), no. Issues 1-4, 181–188, https://doi.org/10.1016/S0370-2693(99)01306-4. (Cited on page 14.)

[161] J. Stachel *et al.*, *Confronting LHC data with the statistical hadronization model*, J. Phys.: Conf. Ser. 509 (2014), 012019, https://10.1088/1742-6596/509/1/012019. (Cited on page 22.)

[162] Jeff Greensite, *An Introduction to the Confinement Problem*, 1st ed., Springer, 2011. (Cited on pages 9 and 153.)

[163] Kai Zhou, Nu Xu, Zhe Xu, and Pengfei Zhuang, *Medium effects on charmonium production at ultrarelativistic energies available at the CERN Large Hadron Collider*, Phys. Rev. C 89 (2014), no. Issue 5, 054911, https://doi.org/10.1103/PhysRevC.89.054911. (Cited on pages 28, 29, 31, and 154.)

[164] L. Betev et. al., *Definition of the alice coordinate system and basic rules for sub-detector components numbering*, ALICE-INT-2003-038 (2003), http://edms.cern.ch/file/406391/1. (Cited on pages 48, 49, and 155.)

[165] Lizardo Valencia Palomo, *Inclusive J/ψ production measurement in Pb-Pb collisions at $\sqrt{s_{NN}} = 2.76$ TeV with the ALICE Muon Spectrometer*, Ph.D. thesis, Université Paris Sud, Paris, 2013, https://tel.archives-ouvertes.fr/tel-01139756. (Cited on pages 68, 72, and 156.)

[166] Lyndon Evans and Philip Bryant, *LHC Machine*, JINST 3 (2008), no. S08001, http://dx.doi.org/10.1088/1748-0221/3/08/S08001. (Cited on page 39.)

[167] M. Bondila *et al.*, *ALICE T0 detector*, IEEE Trans. Nucl. Sci. 52 (2005), no. Issue 5, 1705–1711, https://doi.org/10.1109/TNS.2005.856900. (Cited on page 60.)

[168] M. L. Miller *et al.*, *Glauber Modeling in High-Energy Nuclear Collisions*, Annu. Rev. Nucl. Part. Sci. 57 (2007), 205, https://doi.org/10.1146/annurev.nucl.57.090506.123020. (Cited on pages 91, 92, and 93.)

[169] Maire, Antonin, *QCD potential between 2 coloured objects as a function of their mutual distance, in nuclear matter and in QGP medium*, (2011), no. ALICE-PHO-SKE-2011-002, https://cds.cern.ch/record/2025217. (Cited on pages 8 and 153.)

[170] Maire, Antonin, *Two views on the Bjorken scenario for ultra-relativistic heavy-ion collisions*, (2011), no. ALICE-PHO-SKE-2011-005, https://cds.cern.ch/record/2030270. (Cited on pages 19 and 153.)

[171] Mark G. Alford *et al.*, *Color superconductivity in dense quark matter*, Rev. Mod. Phys. 80 (2008), no. Issue 4, 1455, https://doi.org/10.1103/RevModPhys.80.1455. (Cited on page 13.)

[172] Maximilien Brice, *The ALICE muon spectrometer dipole magnet*, 2005, https://cds.cern.ch/record/865277. (Cited on pages 69 and 156.)

[173] CERN [Media and Press Relations], *CERN releases analysis of the LHC incident*, http://press.cern/press-releases/2008/10/cern-releases-analysis-lhc-incident. (Cited on page 44.)

[174] CERN [Media and Press Relations], *Facts & figures*, https://press.cern/backgrounders/facts-figures. (Cited on page 45.)

[175] Mobs, Esma, *The CERN accelerator complex*, (2016), no. OPEN-PHO-ACCEL-2016-009, https://cds.cern.ch/record/2197559. (Cited on pages 40 and 154.)

[176] N. Brambilla *et al.*, *Heavy quarkonium in a weakly-coupled quark-gluon plasma below the melting temperature*, JHEP 09 (2010), no. 038, https://doi.org/10.1007/JHEP09(2010)038. (Cited on page 25.)

[177] N. Brambilla *et al.*, *Heavy quarkonium: progress, puzzles, and opportunities*, Eur. Phys. J. C 71 (2011), 1534, https://doi.org/10.1140/epjc/s10052-010-1534-9. (Cited on page 25.)

[178] N. Cabibbo and G. Parisi, *Exponential hadronic spectrum and quark liberation*, Phys. Lett. B 59 (1975), no. Issue 1, 67–69, https://doi.org/10.1016/0370-2693(75)90158-6. (Cited on page 13.)

[179] O. Adriani *et al.*, *The L3 + C detector, a unique tool-set to study cosmic rays*, Nucl. Instrum. Meth. A 488 (2002), no. Issues 1-2, 209–225, https://doi.org/10.1016/S0168-9002(02)00479-5. (Cited on page 57.)

[180] P. Braun-Munzinger and J. Stachel, *(Non)thermal aspects of charmonium production and a new look at J/ψ suppression*, Phys. Lett. B 490 (2000), no. Issues 3-4, 196–202, https://doi.org/10.1016/S0370-2693(00)00991-6. (Cited on page 22.)

[181] P. Braun-Munzinger, K. Redlich, and J. Stachel, *Particle Production in Heavy Ion Collisions*, arXiv:nucl-th/0304013v1 (2003), https://arxiv.org/abs/nucl-th/0304013v1. (Cited on page 19.)

[182] P. Petreczky, *Lattice QCD at non-zero temperature*, J. Phys. G: Nuclear and Particle Physics 39 (2012), no. 9, 093002, https://doi.org/10.1088/0954-3899/39/9/093002. (Cited on pages 14, 15, and 16.)

[183] Philippe Pillot, *Private communication*. (Cited on page 85.)

[184] R. Arnaldi *et al.*, *Study of the resistive plate chambers for the ALICE Dimuon Arm*, Nucl. Instrum. Method A 456 (2000), no. Issues 1-2, 73–76, https://doi.org/10.1016/S0168-9002(00)00965-7. (Cited on page 75.)

[185] R. Arnaldi *et al.*, *The ALICE dimuon trigger: overview and electronics prototypes*, Nucl. Instrum. Method A 456 (2000), no. Issues 1-2, 126–131, https://doi.org/10.1016/S0168-9002(00)00977-3. (Cited on page 76.)

[186] R. Arnaldi *et al.*, *A dual threshold technique to improve the time resolution of resistive plate chambers in streamer mode*, Nucl. Instrum. Method A 457 (2001), no. Issues 1-2, 117–125, https://doi.org/10.1016/S0168-9002(00)00760-9. (Cited on page 76.)

[187] R. Arnaldi *et al.*, *Spatial resolution of RPC in streamer mode*, Nucl. Instrum. Method A 490 (2002), no. Issues 1-2, 51–57, https://doi.org/10.1016/S0168-9002(02)00917-8. (Cited on page 75.)

[188] R. Brun and F. Rademakers, *ROOT: An object oriented data analysis framework*, Nucl. Instrum. Meth. A 389 (1997), 81–86, http://root.cern.ch. (Cited on page 62.)

[189] R. Brun *et al.*, *GEANT: Detector Description and Simulation Tool*, CERN, Geneva (1993), http://cds.cern.ch/record/1082634. (Cited on page 63.)

[190] R. Glauber, *Cross sections in deuterium at high energies*, Phys. Rev. 100 (1955), 242, https://doi.org/10.1103/PhysRev.100.242. (Cited on page 91.)

[191] R. Glauber, *Lectures in theoretical physics Vol. 1*, Eds. W. E. Brittin and L. G. Dunham, Interscience (1959), 315, https://archive.org/details/in.ernet.dli.2015.177153. (Not cited.)

[192] R. Glauber, *Quantum optics and heavy ion physics*, Nucl. Phys. A 774 (2006), 3, https://doi.org/10.1016/j.nuclphysa.2006.06.009. (Cited on page 91.)

[193] R. Shahoyan, *J/ψ and ψ(2S) production in 450 GeV pA interactions and its dependence on the rapidity and xF*, Ph.D. thesis, Lisbon, IST, 2001, http://cds.cern.ch/record/915077. (Cited on page 124.)

[194] R. Snellings, *Collective expansion at the LHC: selected ALICE anisotropic flow measurements*, J. Phys. G 41 (2014), no. 12, 124007, https://doi.org/10.1088/0954-3899/41/12/124007. (Cited on page 19.)

[195] R. V. Gavai and Sourendu Gupta, *QCD at finite chemical potential with six time slices*, Phys. Rev. D 78 (2008), no. Issue 11, 114503, https://doi.org/10.1103/PhysRevD.78.114503. (Cited on page 13.)

[196] Robert L. Thews, Martin Schroedter, and Johann Rafelski, *Enhanced J/ψ production in deconfined quark matter*, Phys. Rev. C 63 (2001), no. Issue 5, 054905, https://doi.org/10.1103/PhysRevC.63.054905. (Cited on page 22.)

[197] S. Agostinelli *et al.*, *GEANT4 - a simulation toolkit*, Nucl. Instrum. Meth. A 506 (2003), no. Issue 3, 250–303, https://doi.org/10.1016/S0168-9002(03)01368-8. (Cited on page 63.)

[198] S. Digal, P. Petreczky, and H. Satz, *Quarkonium feed-down and sequential suppression*, Phys. Rev. D 64 (2001), no. Issue 9, 094015, https://doi.org/10.1103/PhysRevD.64.094015. (Cited on page 22.)

[199] Serge Dailler, *LHC Dipole.*, (1998), no. LHC-PHO-1998-299, https://cds.cern.ch/record/842253. (Cited on pages 41 and 154.)

[200] Serge Dailler, *Cross section of LHC dipole.*, (1999), no. LHC-PHO-1999-172, https://cds.cern.ch/record/842530. (Cited on pages 41 and 154.)

[201] Simon Hands, *The phase diagram of QCD*, Contemporary Physics 42 (2001), no. Issue 4, 209–225, https://doi.org/10.1080/00107510110063843. (Cited on page 13.)

[202] Spencer R. Klein and Joakim Nystrand, *Exclusive vector meson production in relativistic heavy ion collisions*, Phys. Rev. C 60 (1999), no. Issue 1, 014903, https://doi.org/10.1103/PhysRevC.60.014903. (Cited on pages 30 and 31.)

[203] STARLIGHT website (2018), http://starlight.hepforge.org/. (Cited on pages 95 and 157.)

[204] Steven Weinberg, *Conceptual foundations of the unified theory of weak and electromagnetic interactions*, Rev. Mod. Phys. 52 (1980), no. 3, 515, https://doi.org/10.1103/RevModPhys.52.515. (Cited on page 6.)

[205] Suire, Christophe, *Installation of station 1 of the tracking chambers of the ALICE Muon Spectrometer*, 2007, https://cds.cern.ch/record/1046255. (Cited on page 70.)

[206] R. Arnaldi *et al.* [Proc. Suppl.], *Design and Performance of the ALICE Muon Trigger System*, Nucl. Phys. B 158 (2006), 21–24, https://doi.org/10.1016/j.nuclphysbps.2006.07.012. (Cited on page 74.)

[207] R. Arnaldi *et al.* [Proc. Suppl.], *Overview on production and first results of the tests on the RPCs for the ALICE dimuon trigger*, Nucl. Phys. B 158 (2006), 83–86, https://doi.org/10.1016/j.nuclphysbps.2006.07.003. (Cited on page 76.)

[208] T. Lappi and H. Mäntysaari, *J/ψ production in ultraperipheral Pb + Pb and p + Pb collisions at energies available at the CERN Large Hadron Collider*, Phys. Rev. C 87 (2013), no. Issue 3, 032201, https://doi.org/10.1103/PhysRevC.87.032201. (Cited on pages 30 and 31.)

[209] T. Ludlam *et al.*, *HIJET: A Monte Carlo Event Generator for p-Nucleus and Nucleus-Nucleus Collisions*, BNL 37196 (1985), 373–381, https://inis.iaea.org/search/search.aspx?orig_q=RN:17030604. (Cited on page 92.)

[210] T. Matsui and H. Satz, *J/ψ suppression by quark-gluon plasma formation*, Phys. Lett. B 178 (1986), no. 4, 416–422, http://dx.doi.org/10.1016/0370-2693(86)91404-8. (Cited on pages 20 and 22.)

[211] B. Espagnon [For the ALICE Collaboration], *The ALICE muon spectrometer and related physics*, J. Phys. G: Nucl. Part. Phys. 35 (2008), no. 10, 104145(4pp), http://dx.doi.org/10.1088/0954-3899/35/10/104145. (Cited on page 65.)

[212] M. Wilde [For the ALICE Collaboration], *Measurement of Direct Photons in pp and Pb–Pb Collisions with ALICE*, Nuclear Physics A 904-905 (2013), 573–576, https://doi.org/10.1016/j.nuclphysa.2013.02.079. (Cited on page 19.)

[213] V. Chambert *et al.* [For the ALICE Collaboration], *The electronics of ALICE Dimuon tracking chambers*, Topical Workshop on Electronics for Particle Physics, Naxos, Greece, 15 - 19 Sep 2008 (2008), 242–246, https://cds.cern.ch/record/1158633. (Cited on page 73.)

[214] Christian Finck [For the ALICE Muon Spectrometer collaboration], *The ALICE muon spectrometer and related physics*, J. Phys.: Conf. Series 50 (2006), no. 1, 397–401, https://doi.org/10.1088/1742-6596/50/1/056. (Cited on pages 67 and 70.)

[215] The HL-LHC project, https://hilumilhcds.web.cern.ch/about/hl-lhc-project. (Cited on pages 45 and 155.)

[216] Torbjörn Sjöstrand *et al.*, *PYTHIA 6.4 physics and manual*, Journal of High Energy Physics 05 (2006), no. 026, https://doi.org/10.1088/1126-6708/2006/05/026. (Cited on page 63.)

[217] TU WIEN website, https://ati.tuwien.ac.at. (Cited on pages 9 and 153.)

[218] U. Heinz, *The Little Bang: searching for quark–gluon matter in relativistic heavy-ion collisions*, Nuclear Physics A 685 (2001), no. Issues 1-4, 414–431, https://doi.org/10.1016/S0375-9474(01)00558-9. (Cited on page 18.)

[219] U. Heinz, *The quark-gluon plasma at RHIC*, Nuclear Physics A 721 (2003), 30–39, https://doi.org/10.1016/S0375-9474(03)01014-5. (Cited on page 19.)

[220] V. Grigoriev *et al.*, *A Start Trigger Detector for the ALICE Spectrometer*, Instrum. Exp. Tech. 43 (2000), no. Issue 6, 750–755, https://doi.org/10.1023/A:1026607631385. (Cited on page 60.)

[221] V. P. Goncalves and M. V. T. Machado, *Vector meson production in coherent hadronic interactions: Update on predictions for energies available at the BNL Relativistic Heavy Ion Collider and the CERN Large Hadron Collider*, Phys. Rev. C 84 (2011), no. Issue 1, 011902, https://doi.org/10.1103/PhysRevC.84.011902. (Cited on page 30.)

[222] V. Rebyakova, M. Strikman, and M. Zhalov, *Coherent ρ and J/ψ photoproduction in ultraperipheral processes with electromagnetic dissociation of heavy ions at RHIC and LHC*, Phys. Lett. B 710 (2012), no. Issue 4-5, 647–653, https://doi.org/10.1016/j.physletb.2012.03.041. (Cited on pages 30 and 31.)

[223] Weber, Steffen Georg and Andronic, Anton, *ALICE event display of a Pb-Pb collision at $\sqrt{s_{NN}}$ = 5.02 TeV*, (2016), no. ALICE-PHO-GEN-2016-001, https://cds.cern.ch/record/2202730. (Cited on pages 52 and 155.)

[224] Wei-Tian Deng, Xin-Nian Wang, and Rong Xu, *Hadron production in p+p, p+Pb, and Pb+Pb collisions with the HIJING 2.0 model at energies available at the CERN Large Hadron Collider*, Phys. Rev. C 83 (2011), no. Issue 1, 014915, https://link.aps.org/doi/10.1103/PhysRevC.83.014915. (Cited on pages 63 and 92.)

[225] X. Du and R. Rapp, *Sequential regeneration of charmonia in heavy-ion collisions*, Nucl. Phys. A 943 (2015), 147–158, https://doi.org/10.1016/j.nuclphysa.2015.09.006. (Cited on pages 27, 28, 29, 30, and 154.)

[226] X. Zhao and R. Rapp, *Transverse momentum spectra of J/ψ in heavy-ion collisions*, Phys. Lett. B 664 (2008), no. Issues 4-5, 253–257, https://doi.org/10.1016/j.physletb.2008.03.068. (Cited on page 24.)

[227] X. Zhao and R. Rapp, *Forward and midrapidity charmonium production at RHIC*, Eur. Phys. J C 62 (2009), no. Issue 1, 109–117, https://doi.org/10.1140/epjc/s10052-009-0905-6. (Cited on page 24.)

[228] X. Zhao and R. Rapp, *Medium modifications and production of charmonia at LHC*, Nucl. Phys. A 859 (2011), no. Issue 1, 114–125, https://doi.org/10.1016/j.nuclphysa.2011.05.001. (Cited on pages 27, 28, 29, 30, and 154.)

[229] Y. Aoki *et al.*, *The QCD transition temperature: results with physical masses in the continuum limit II*, JHEP 06 (2009), 088, https://doi.org/10.1088/1126-6708/2009/06/088. (Cited on page 13.)

[230] Y. Nambu and G. Jona-Lasinio, *Dynamical Model of Elementary Particles Based on an Analogy with Superconductivity. I*, Phys. Rev. 122 (1961), no. Issue 1, 345, https://doi.org/10.1103/PhysRev.122.345. (Cited on page 13.)

[231] Y. Nambu and G. Jona-Lasinio, *Dynamical Model of Elementary Particles Based on an Analogy with Superconductivity. II*, Phys. Rev. 124 (1961), no. Issue 1, 246, https://doi.org/10.1103/PhysRev.124.246. (Cited on page 13.)

[232] Z. Fodor, *Lattice QCD results at finite temperature and density*, Nuclear Physics A 715 (2003), 319–328, https://doi.org/10.1016/S0375-9474(02)01442-2. (Cited on page 16.)

[233] Z. Fodor and S. Katz, *Critical point of QCD at finite T and μ, lattice results for physical quark masses*, JHEP 04 (2004), https://doi.org/10.1088/1126-6708/2004/04/050. (Cited on page 13.)

[234] Zaida Conesa del Valle, *Vector bosons in heavy-ion collisions at the LHC*, Eur. Phys. J C 61 (2009), no. Issue 4, 729–733, https://doi.org/10.1140/epjc/s10052-009-0980-8. (Cited on page 20.)